

ISSN 2732-0189 (Online)
ISSN 1586-2070 (Print)

JOURNAL OF COMPUTATIONAL AND APPLIED MECHANICS

An Open Access International Journal

Published by the University of Miskolc

VOLUME 19, NUMBER 1 (2024)



MISKOLC UNIVERSITY PRESS

ISSN 2732-0189 (Online)
ISSN 1586-2070 (Print)

JOURNAL OF COMPUTATIONAL AND APPLIED MECHANICS

An Open Access International Journal

Published by the University of Miskolc

VOLUME 19 NUMBER 1 (2024)



MISKOLC UNIVERSITY PRESS

EDITOR-IN-CHIEF

Balázs TÓTH, University of Miskolc, Hungary, balazs.toth@uni-miskolc.hu

EDITORS

Tamás FÜLÖP, Budapest University of Technology and Economics, Hungary, fulop.tamas@gpk.bme.hu

Róbert KOVÁCS, Budapest University of Technology and Economics, Hungary, kovacs.robert@wigner.mta.hu

EDITORIAL ADVISORY BOARD

Holm ALTENBACH, Otto-von-Guericke Universität
Magdeburg, Germany,
holm.altenbach@ovgu.de

Edgár BERTÓTI, University of Miskolc, Hungary,
edgar.bertoti@uni-miskolc.hu

Attila BAKSA, University of Miskolc, Hungary,
attila.baksa@uni-miskolc.hu

Leszek Felix DEMKOWICZ, The University of Texas
at Austin, USA,
leszek@oden.utexas.edu

Amit Kumar DHIMAN, Indian Institute of
Technology, Roorkee, India,
dhimuamit@rediffmail.com

Alexander DÜSTER, Hamburg University of
Technology, Germany,
alexander.duester@tuhh.de

István ECSEDI, University of Miskolc, Hungary,
mechecs@uni-miskolc.hu

Gusztáv FEKETE, Széchenyi István
University, Győr, Hungary,
fekete.gusztav@sze.hu

Ulrich GABBERT, Otto-von-Guericke-Universität
Magdeburg, Germany,
ulrich.gabbert@mb.uni-magdeburg.de

Robert HABER, University of Illinois
at Urbana-Champaign, USA,
rbh3@illinois.edu

Csaba HÓS, Budapest University of Technology and
Economics, Hungary,
hoscscaba@vizgep.bme.hu

Gábor JANIGA, Otto-von-Guericke-Universität
Magdeburg, Germany,
janiga@ovgu.de

Károly JÁRMAI, University of Miskolc, Hungary,
altjar@uni-miskolc.hu

Daniel JUHRE, Otto-von-Guericke Universität
Magdeburg, Germany,
daniel.juhre@ovgu.de

László KOLLÁR, Budapest University of Technology
and Economics, Hungary,
lkollar@eik.bme.hu

Efstathios KONSTANTINIDIS, University of
Western Macedonia, Greece,
ekonstantinidis@uowm.gr

József KÖVECSES, McGill University, Canada,
jozsef.kovecses@mcgill.ca

László KÖNÖZSY, Cranfield University, UK
laszlo.konozsy@cranfield.ac.uk

Márta KURUTZ, Budapest University of Technology
and Economics, Hungary,
kurutzm@eik.bme.hu

Lin LU, Dalian University of Technology, China,
lulin@dlut.edu.cn

Herbert MANG, Vienna University of Technology,
Austria,
Herbert.Mang@tuwien.ac.at

Sanjay MITTAL, Indian Institute of Technology,
Kanpur, India,
smittal@iitk.ac.in

Zenon MRÓZ, Polish Academy of Sciences,
zmroz@ippt.gov.pl

Sukumar PATI, National Institute of Technology
Silchar, India, sukumarpati@gmail.com

Gyula PATKÓ, University of Miskolc, Hungary,
patko@uni-miskolc.hu

István PÁCZELT, University of Miskolc, Hungary,
istvan.paczelt@uni-miskolc.hu

Srboljub SIMIĆ, University of Novi Sad, Serbia,
ssimic@uns.ac.rs

Jan SLADEK, Slovak Academy of Sciences, Slovakia,
usarslad@sayba.sk

Gábor STÉPÁN, Budapest University of Technology
and Economics, Hungary,
stepan@mm.bme.hu

Barna SZABÓ, Washington University, USA,
szabo@wustl.edu

Péter VÁN, Wigner Research Centre for Physics,
Budapest, Hungary
van.peter@wigner.mta.hu

Meizi WANG, The Hong Polytechnic University,
Hong Kong, China
meiziwang@polyu.edu.hk

Krzysztof WISNIEWSKI, Polish Academy of
Sciences, Poland
kwisn@ippt.pan.pl

Song YANG, The Hong Polytechnic University, Hong
Kong, China
yangsong@polyu.edu.hk

SECRETARY GENERAL

Ákos LENGYEL, University of Miskolc, Hungary, akos.lengyel@uni-miskolc.hu

COPY EDITOR

Robin Lee NAGANO, Institute of Modern Philology, University of Miskolc, Hungary,

HONORARY EDITORIAL ADVISORY BOARD MEMBERS

László BARANYI, University of Miskolc, Hungary,

Gábor HALÁSZ, Budapest University of Technology and Economics, Hungary

György SZEIDL, University of Miskolc, Hungary

INVESTIGATION OF THE STRESS STATE IN A THIN ELASTIC DISC

ISTVÁN ECSEDI

Institute of Applied Mechanics, University of Miskolc
Miskolc-Egyetemváros, H-3515 Miskolc, Hungary

mechecs@uni-miskolc.hu

ÁKOS JÓZSEF LENGYEL

Institute of Applied Mechanics, University of Miskolc
Miskolc-Egyetemváros, H-3515 Miskolc, Hungary

akos.lengyel@uni-miskolc.hu

[Received: July 6, 2023; Accepted: March 25, 2024]

Abstract. This paper deals with the stress state in a thin elastic disc which is loaded by a uniform radial load on its outer curved boundary surface. Two solutions are presented. The first is an elastic solution based on the governing equation of the plane stress state. The second is a strength of material solution. The results obtained from the plane stress model are compared to those obtained from the strength of material solution.

Mathematical Subject Classification: 74A10, 74B05, 74G10, 74K20

Keywords: Thin elastic disc, plane stress, strength of materials

1. FORMULATION OF THE BOUNDARY VALUE PROBLEM

Figure 1 shows the thin elastic disc which is loaded by uniform radial load on its outer curved boundary part. The plane domain of the middle section of the elastic disc is denoted by A and the boundary curve of A is $\partial A = \partial A_1 \cup \partial A_2 \cup \partial A_3 \cup \partial A_4$. The formulation of the boundary value problem is presented in the $Or\varphi$ cylindrical coordinate system. It is evident that

$$A = \{(r, \varphi) \mid a \leq r \leq b, 0 \leq \varphi \leq \pi\}, \quad (1.1)$$

$$\partial A_1 = \{(r, \varphi) \mid a \leq r \leq b, \varphi = 0\}, \quad (1.2)$$

$$\partial A_2 = \{(r, \varphi) \mid r = b, 0 \leq \varphi \leq \pi\}. \quad (1.3)$$

$$\partial A_3 = \{(r, \varphi) \mid a \leq r \leq b, \varphi = \pi\}, \quad (1.4)$$

$$\partial A_4 = \{(r, \varphi) \mid r = a, 0 \leq \varphi \leq \pi\}. \quad (1.5)$$

The displacement vector $\mathbf{t} = \mathbf{t}(r, \varphi)$ can be represented as

$$\mathbf{t}(r, \varphi) = u(r, \varphi) \mathbf{e}_r + v(r, \varphi) \mathbf{e}_\varphi, \quad (1.6)$$

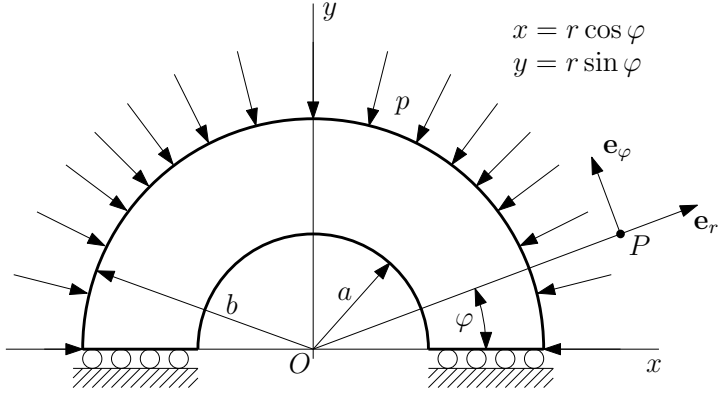


Figure 1. Thin elastic disc with uniform radial load

where \mathbf{e}_r and \mathbf{e}_φ are the unit vectors of the cylindrical coordinate system $Or\varphi$ (see Figure 1). The expressions of the strains are as follows [1–5]

$$\varepsilon_r = \frac{\partial u}{\partial r}, \quad \varepsilon_\varphi = \frac{u}{r} + \frac{1}{r} \frac{\partial v}{\partial \varphi}, \quad (1.7)$$

$$\gamma_{r\varphi} = \frac{1}{r} \frac{\partial u}{\partial \varphi} + \frac{\partial v}{\partial r} - \frac{v}{r}. \quad (1.8)$$

Based on the strain-displacement relationships [1–5] the following equations are valid

$$\varepsilon_r = \frac{\sigma_r}{E} - \nu \frac{\sigma_\varphi}{E}, \quad \varepsilon_\varphi = -\nu \frac{\sigma_r}{E} + \frac{\sigma_\varphi}{E}, \quad (1.9)$$

$$\gamma_{r\varphi} = \frac{2(1+\nu)}{E} \tau_{r\varphi}. \quad (1.10)$$

In equations (1.9) and (1.10) σ_r and σ_φ are the normal stresses, $\tau_{r\varphi}$ denotes the shearing stress, E represents the modulus of elasticity and ν means the Poisson number. For this problem the equations of mechanical equilibrium are

$$\frac{\partial \sigma_r}{\partial r} + \frac{1}{r} \frac{\partial \tau_{r\varphi}}{\partial \varphi} + \frac{\sigma_r - \sigma_\varphi}{r} = 0, \quad (r, \varphi) \in A, \quad (1.11)$$

$$\frac{\partial \tau_{r\varphi}}{\partial r} + \frac{1}{r} \frac{\partial \sigma_\varphi}{\partial \varphi} + \frac{2}{r} \tau_{r\varphi} = 0, \quad (r, \varphi) \in A. \quad (1.12)$$

The following boundary conditions are prescribed in this problem:

$$\tau_{r\varphi} = 0, \quad v = 0 \text{ on } \partial A_1, \quad (1.13)$$

$$\sigma_r = -p = \text{constant}, \quad \tau_{r\varphi} = 0 \text{ on } \partial A_2, \quad (1.14)$$

$$\tau_{r\varphi} = 0, \quad v = 0 \text{ on } \partial A_3, \quad (1.15)$$

$$\tau_{r\varphi} = 0, \quad \sigma_r = 0 \text{ on } \partial A_4. \quad (1.16)$$

The solution to the boundary value problem formulated by equations (1.7–1.14) will be solved under the conditions

$$u = u(r), \quad v(r, \varphi) = 0, \quad (r, \varphi) \in A \cup \partial A. \quad (1.17)$$

2. PLANE STRESS SOLUTION

From equation (1.17) it follows that the equations of mechanical equilibrium are reduced to one equation, which is

$$\frac{d}{dr}(r\sigma_r) - \sigma_\varphi = 0, \quad (r, \varphi) \in A. \quad (2.1)$$

The general solution of stress equilibrium equation (2.1) in terms of stress function $F = F(r)$ can be represented for a thin elastic disc as

$$\sigma_r(r) = \frac{1}{t} \frac{F(r)}{r}, \quad \sigma_\varphi(r) = \frac{1}{t} \frac{dF(r)}{dr}, \quad (r, \varphi) \in A \cup \partial A, \quad (2.2)$$

where t is the thickness of the elastic disc. From equations (1.7) and (1.9) it follows that

$$Et \frac{du}{dr} = \frac{F}{r} - \nu \frac{dF}{dr}, \quad (2.3)$$

$$Et \frac{u}{r} = -\nu \frac{F}{r} + \frac{dF}{dr}. \quad (2.4)$$

The combination of equation (2.3) with (2.4) gives an ordinary second order differential equation for $F = F(r)$

$$\frac{d^2F}{dr^2} + \frac{1}{r} \frac{dF}{dr} - \frac{F}{r^2} = 0, \quad a < r < b. \quad (2.5)$$

According to the traction boundary conditions (1.14), (1.16) $F = F(r)$ satisfies the following boundary conditions

$$F(a) = 0, \quad F(b) = -pbt. \quad (2.6)$$

The solution to the boundary value problem formulated by equations (2.5), (2.6) is

$$F(r) = \frac{b^2tp}{b^2 - a^2} \left(-r + \frac{a^2}{r} \right), \quad a \leq r \leq b. \quad (2.7)$$

The expressions of normal stresses σ_r and σ_φ can be represented as

$$\sigma_r(r) = \frac{b^2p}{b^2 - a^2} \left(-1 + \frac{a^2}{r^2} \right), \quad a \leq r \leq b, \quad (2.8)$$

$$\sigma_\varphi(r) = -\frac{b^2p}{b^2 - a^2} \left(1 + \frac{a^2}{r^2} \right), \quad a \leq r \leq b. \quad (2.9)$$

Based on equations (1.7), (1.9)₁ and (1.17) it is evident that

$$u(r) = \frac{r}{E} (\sigma_\varphi - \nu\sigma_r) \quad (2.10)$$

from which the following formula can be obtained for the radial displacement

$$u(r) = \frac{b^2p}{E(b^2 - a^2)} \left[(\nu - 1)r - (1 + \nu) \frac{a^2}{r} \right], \quad 0 \leq r \leq b. \quad (2.11)$$

3. STRENGTH OF MATERIAL SOLUTION

The formulation of the strength of material solution is based on the paper [5], which uses the displacement field

$$\mathbf{u}(r, \varphi) = U(\varphi)\mathbf{e}_r + \left(r\phi(\varphi) + \frac{dU}{d\varphi} \right) \mathbf{e}_\varphi. \quad (3.1)$$

The corresponding strain field as a function of the displacement field given by equation (3.1) is

$$\varepsilon_\varphi = \frac{W(\varphi)}{r} + \frac{d\phi}{d\varphi}, \quad W(\varphi) = \frac{d^2U}{d\varphi^2} + U(\varphi). \quad (3.2)$$

Figure 2 shows the strength of material model according to paper [5]. The resultants of the tractions acting on the boundary surface segments ∂A_1 and ∂A_3 are F_1 and F_3 . The moments of traction acting on the boundary surface segments ∂A_1 and ∂A_3 are M_1 and M_3 and we have $M_1 = M_3 = M_0$. The value of M_0 is obtained from the condition

$$\phi(\varphi) = 0, \quad 0 \leq \varphi \leq \pi \quad (3.3)$$

according to the results presented in Section 2 of this paper. Application of the Hooke law gives

$$\sigma_\varphi(r, \varphi) = E \left(\frac{W(\varphi)}{r} + \frac{d\phi}{d\varphi} \right). \quad (3.4)$$

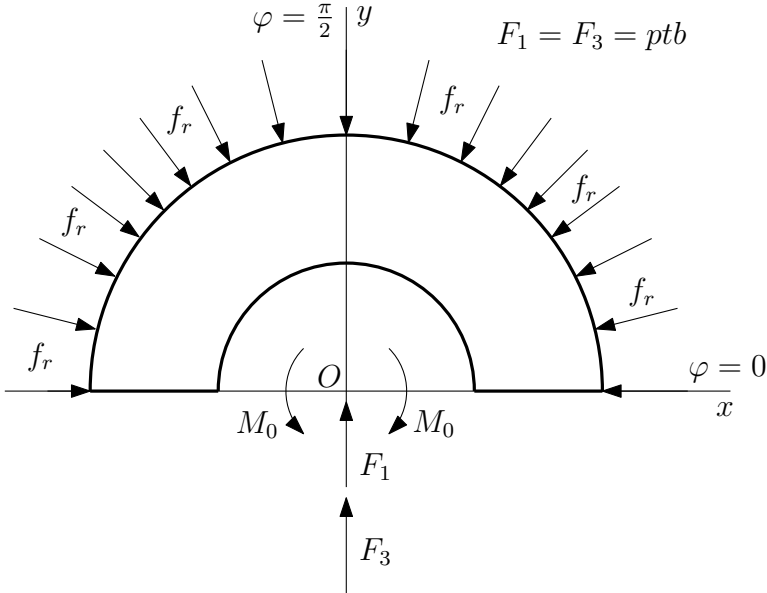


Figure 2. Strength of material model.

The normal force and bending moment on an arbitrary cross section can be calculated as

$$N = \int_A \sigma_\varphi dA, \quad M = \int_A r \sigma_\varphi dA. \quad (3.5)$$

Detailed forms of expressions of $N = N(\varphi)$ and $M(\varphi)$ are as follows:

$$N(\varphi) = Et \left[W(\varphi) \ln \frac{b}{a} + (b-a) \frac{d\phi}{d\varphi} \right], \quad (3.6)$$

$$M(\varphi) = Et \left[W(\varphi)(b-a) + c(b-a) \frac{d\phi}{d\varphi} \right], \quad (3.7)$$

where

$$c = 0.5(a+b). \quad (3.8)$$

In the present problem the solution of equilibrium equation [5]

$$\frac{d^2 N}{d\varphi^2} + N - f_r = 0 \quad (3.9)$$

is

$$f_r = -btp = \text{constant}, \quad 0 \leq \varphi \leq \pi. \quad (3.10)$$

The shear force $S = S(\varphi)$ vanishes since

$$S(\varphi) = -\frac{dN}{d\varphi} = 0, \quad (3.11)$$

and from the moment equilibrium equation it follows that

$$M(\varphi) = M = \text{constant}, \quad 0 \leq \varphi \leq \pi. \quad (3.12)$$

If $\phi = 0$ ($0 \leq \varphi \leq \pi$) then

$$M = -t \frac{(b-a)b}{\ln \frac{b}{a}} p, \quad (3.13)$$

$$W = \frac{d^2 U}{d\varphi^2} + U = -\frac{bp}{E \ln \frac{b}{a}}. \quad (3.14)$$

Substitution of equation (3.14) into equation (3.4) gives

$$\sigma_\varphi(r) = -\frac{b}{r \ln \frac{b}{a}} p, \quad a \leq r \leq b. \quad (3.15)$$

From the stress equilibrium equation

$$\frac{d}{dr} (r\sigma_r) = \sigma_\varphi \quad (3.16)$$

it follows that

$$r\sigma_r(r) - a\sigma_r(a) = -\frac{bp}{\ln \frac{b}{a}} \ln \frac{r}{a}, \quad a \leq r \leq b, \quad (3.17)$$

that is

$$\sigma_r(r) = -\frac{bp}{r} \frac{\ln \frac{r}{a}}{\ln \frac{b}{a}}, \quad a \leq r \leq b. \quad (3.18)$$

Thus, the normal stress σ_r given by equation (3.18) satisfies the stress boundary conditions

$$\sigma_r(a) = 0, \quad \sigma_r(b) = -p. \quad (3.19)$$

Integration of equation (3.14) provides the radial displacement

$$U(\varphi) = -\frac{bp}{E \ln \frac{b}{a}} + \alpha \cos \varphi + \beta \sin \varphi, \quad (3.20)$$

where α and β are the constants of integration and

$$V(\varphi) = \frac{dU}{d\varphi} = -\alpha \sin \varphi + \beta \cos \varphi. \quad (3.21)$$

By means of the boundary conditions

$$V(0) = V(\pi) = 0, \quad V\left(\frac{\pi}{2}\right) = 0 \quad (3.22)$$

it is easy to prove that

$$\alpha = \beta = 0, \quad (3.23)$$

so the radial displacement has the form

$$U(\varphi) = -\frac{bp}{E \ln \frac{b}{a}} = \text{constant}, \quad 0 \leq \varphi \leq 2\pi. \quad (3.24)$$

4. DETERMINATION OF VON MISES STRESS

In the present problem the equivalent Von Mises stress is obtained from the formula

$$\sigma(r) = \sqrt{\sigma_r^2(r) + \sigma_\varphi^2(r) - \sigma_r(r)\sigma_\varphi(r)}, \quad (4.1)$$

which yields the following result for the plane stress model

$$\sigma_1(r) = \frac{b^2 p}{(b^2 - a^2) r^2} \sqrt{r^4 + 3a^4} \quad (4.2)$$

and for the strength of material model

$$\sigma_2(r) = \frac{bp}{r \ln \frac{b}{a}} \sqrt{1 - \ln \frac{r}{a} + \left(\ln \frac{r}{a}\right)^2}. \quad (4.3)$$

5. COMPARISON OF THE SOLUTIONS

In the following, the effect of the geometric parameters on the stresses is examined. First of all the radial normal stresses are considered. The radial normal stress is obtained from plane stress solution σ_r^{ps} [see equation (2.8)] and it can be reformulated in the following manner:

$$\sigma_r^{\text{ps}} = \frac{pb^2}{b^2 - a^2} \left(-1 + \frac{a^2}{r^2}\right) = p \frac{1}{1 - \left(\frac{a}{b}\right)^2} \left[-1 + \left(\frac{a}{r}\right)^2\right]. \quad (5.1)$$

Similarly, the radial normal stress derived from the strength of material solution σ_r^{sm} [see equation (3.18)] can be written in the form

$$\sigma_r^{\text{sm}} = -\frac{bp \ln \frac{r}{a}}{r \ln \frac{b}{a}} = -p \frac{b}{a} \frac{\ln \frac{r}{a}}{r \ln \frac{b}{a}}. \quad (5.2)$$

New variables are introduced:

$$\lambda = \frac{a}{r}, \quad \psi = \frac{a}{b}. \quad (5.3)$$

Since $a \leq r \leq b$ it is easy to prove that

$$0 < \psi < 1, \quad \psi \leq \lambda \leq 1. \quad (5.4)$$

Substitution of equations (5.3) into equations (5.1) and (5.2) yields

$$\sigma_r^{\text{ps}} = p \frac{1}{1 - \psi^2} [-1 + \lambda^2], \quad (5.5)$$

$$\sigma_r^{\text{sm}} = -p \frac{\lambda \ln \frac{1}{\lambda}}{\psi \ln \frac{1}{\psi}}. \quad (5.6)$$

Let $\Delta_r = \Delta_r(\lambda, \psi)$ denote the dimensionless difference of the radial normal stresses

$$\Delta_r(\lambda, \psi) = \frac{\sigma_r^{\text{ps}} - \sigma_r^{\text{sm}}}{p} = \frac{1}{1 - \psi^2} [-1 + \lambda^2] + \frac{\lambda \ln \frac{1}{\lambda}}{\psi \ln \frac{1}{\psi}}. \quad (5.7)$$

Figure 3 illustrates the dimensionless difference function $\Delta_r(\lambda, \psi)$.

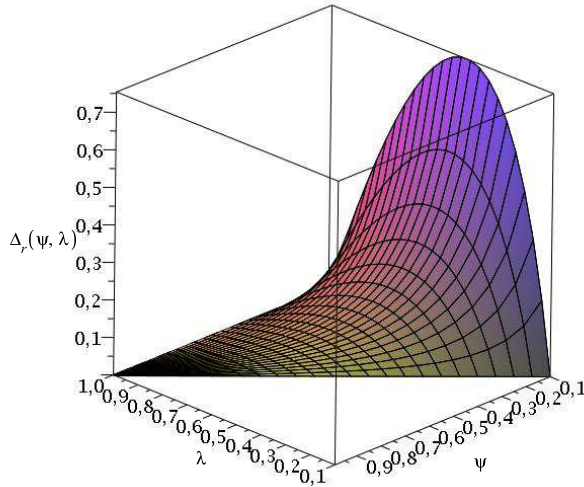


Figure 3. The dimensionless difference function $\Delta_r = \Delta_r(\lambda, \psi)$

The tangential normal stresses can be modified similarly. In the case of the plane stress solution, according to equation (2.8) one can write

$$\sigma_{\varphi}^{\text{ps}} = -\frac{b^2 p}{b^2 - a^2} \left(1 + \frac{a^2}{r^2}\right) = -p \frac{1}{1 - \left(\frac{a}{b}\right)^2} \left[1 + \left(\frac{a}{r}\right)^2\right]. \quad (5.8)$$

The modified form of the tangential normal stress in connection with the strength of material solution from equation (3.15) is as follows

$$\sigma_{\varphi}^{\text{sm}} = -\frac{b}{r \ln \frac{b}{a}} p = -p \frac{b}{a} \frac{1}{r \ln \frac{b}{a}}. \quad (5.9)$$

Substitution of equations (5.3) into equations (5.8) and (5.9) provides

$$\sigma_{\varphi}^{\text{ps}} = -p \frac{1}{1 - \psi^2} (1 + \lambda^2), \quad (5.10)$$

$$\sigma_{\varphi}^{\text{sm}} = -p \frac{\lambda}{\psi} \frac{1}{\ln \frac{1}{\psi}}. \quad (5.11)$$

Another dimensionless difference function denoted by $\Delta_{\varphi} = \Delta_{\varphi}(\lambda, \psi)$ can be established according to tangential normal stresses (5.10) and (5.11)

$$\Delta_{\varphi}(\lambda, \psi) = \frac{\sigma_{\varphi}^{\text{ps}} - \sigma_{\varphi}^{\text{sm}}}{p} = -\frac{1}{1 - \psi^2} (1 + \lambda^2) + \frac{\lambda}{\psi} \frac{1}{\ln \frac{1}{\psi}}. \quad (5.12)$$

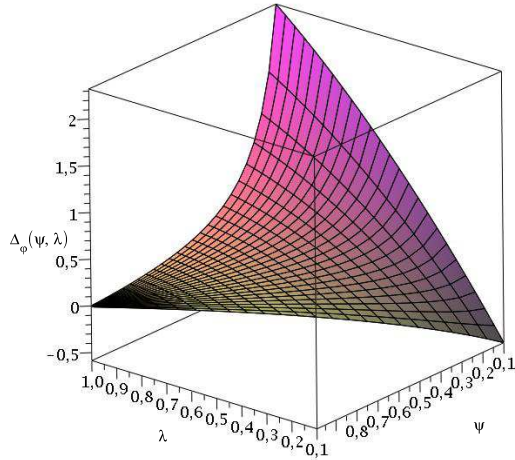


Figure 4. The dimensionless difference function $\Delta_{\varphi} = \Delta_{\varphi}(\lambda, \psi)$

Figure 4 shows the $\Delta_{\varphi} = \Delta_{\varphi}(\lambda, \psi)$ function. Figures 3 and 4 represent that the differences between the two solutions converge to zero when $\lambda, \psi \rightarrow 1$, which means that the outer radius b of the disc converges to the inner radius a (Figure 1). In that

case the problem actually becomes a curved beam problem and then the two solutions are in good congruence. If $\psi \rightarrow 0$, namely the parameter b is significantly higher than a (so the disc is wide), then the difference between the two solutions increases.

6. NUMERICAL EXAMPLES

6.1. Narrow disk. The following data are used in the first numerical example: $a = 0.1$ m, $b = 0.2$ m, $E = 2 \times 10^{11}$ Pa, $\nu = 0.3$, $p = 25 \times 10^6$. According to the parameters $\psi = a/b = 0.5$ in this case. Investigating Figures 3 and 4, the example is close to a beam problem as the dimensionless difference functions (5.7) and (5.12) provide relatively low discrepancy between the two solutions. A plane stress FEM analysis has been also made to check and compare the results. In Figures 5 and 6 the plots of σ_r and σ_φ are shown as functions of r . The graphs of Von Mises stresses as a function of r are presented in Figure 7. Figure 8 represents the radial displacement functions as a function of r . The values of the radial displacement for $r = a$, $r = b$, $r = 0.5(a + b)$ are listed below

$$u(a) = -0.000033334 \text{ m}, \quad u(b) = -0.0000341666 \text{ m},$$

$$u\left(\frac{a+b}{2}\right) = -0.0000319444 \text{ m}, \quad U = -0.000036067 \text{ m}.$$

It can be clearly seen that the plane stress solution and the FEM solution (plane stress model too) produce practically the same results for all the stress and displacement functions. In this case the strength of material solution does not differ significantly from the plane stress results, either.

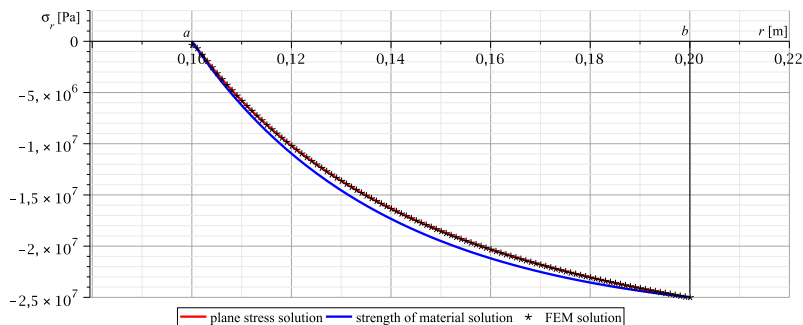


Figure 5. The plots of the radial normal stress functions $\sigma_r(r)$ (narrow disk)

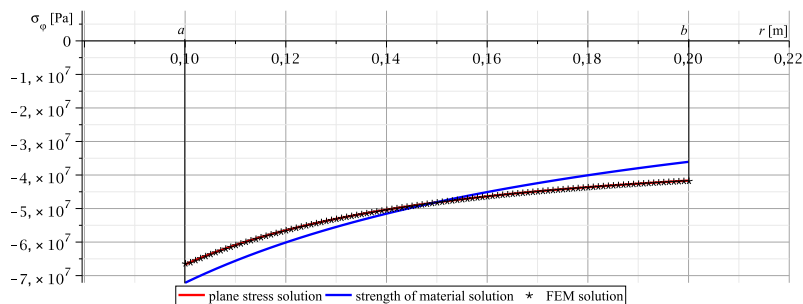


Figure 6. The plots of the tangential normal stress functions $\sigma_\varphi(r)$ (narrow disk)

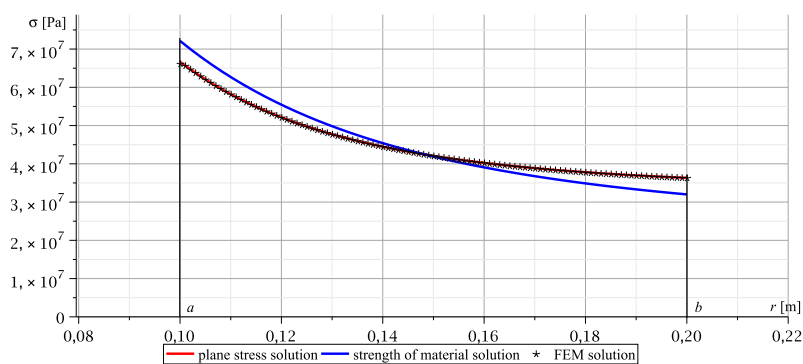


Figure 7. The plots of the Von Mises stress functions $\sigma(r)$ (narrow disk)

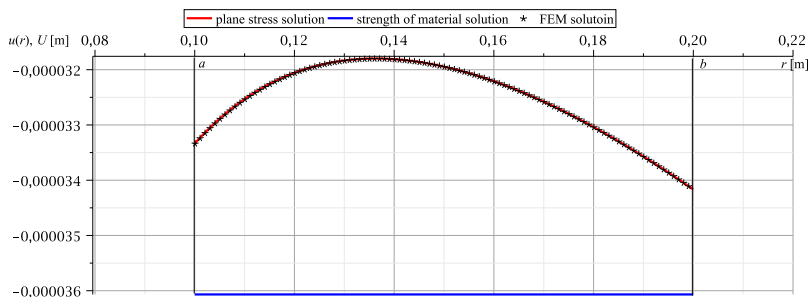


Figure 8. The plots of the radial displacement functions $u(r)$, U (narrow disk)

6.2. Wide disk. In this example a wide disk is analysed. The data are the same as in Example 6.1 with one exception. The outer radius of the disk $b = 1$ m. The ratio of the geometrical parameters $a/b = \psi = 0.1$, which means a much higher difference between the two analytical solutions according to dimensionless difference functions (5.7) and (5.12) (see Figures 3 and 4). A plane stress FEM analysis was carried out for this wide disk, as well. In Figure 9 the radial stress functions are shown as a function of r . The tangential stress functions as a function of r can be seen in Figure 10. Figure 11 represents the Von Mises stress functions in terms of r . The displacement functions in terms of r are also given in Figure 12. The values of the radial displacement for $r = a$, $r = b$, $r = 0.5(a + b)$ are listed below:

$$u(a) = -0.000025253 \text{ m}, \quad u(b) = -0.000090025 \text{ m},$$

$$u\left(\frac{a+b}{2}\right) = -0.000051596 \text{ m}, \quad U = -0.000054287 \text{ m}.$$

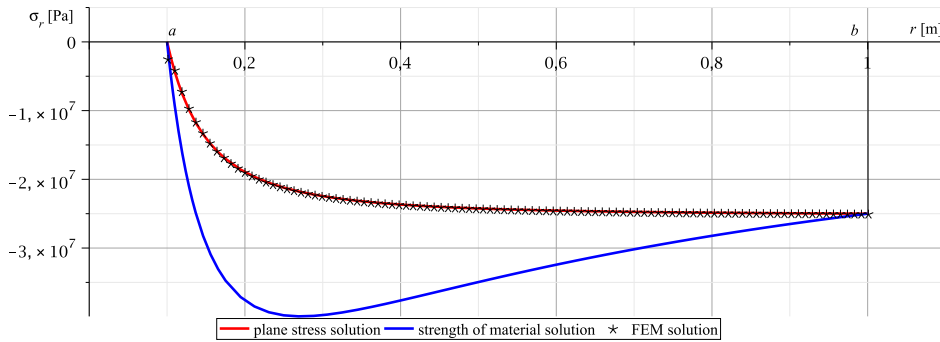


Figure 9. The plots of the radial normal stress functions $\sigma_r(r)$ (wide disk)

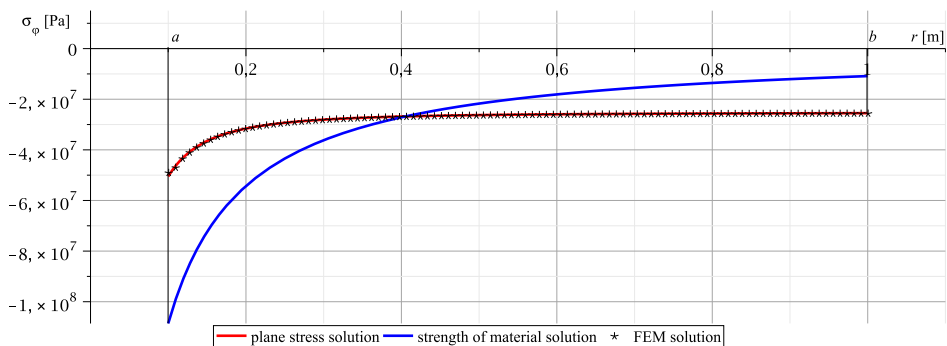


Figure 10. The plots of the tangential normal stress functions $\sigma_\varphi(r)$ (wide disk)

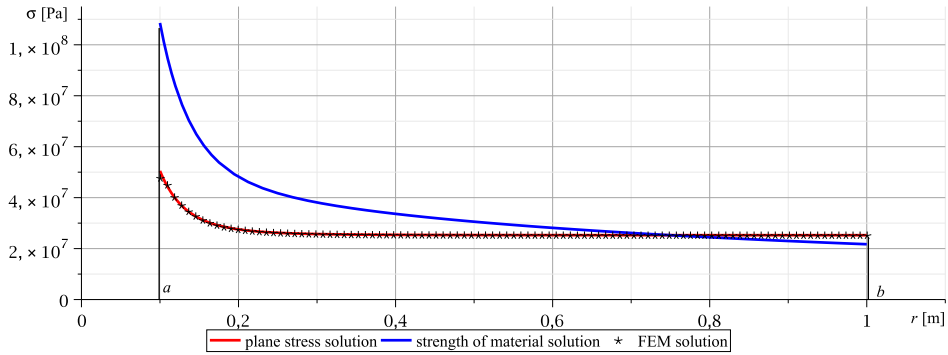


Figure 11. The plots of the Von Mises stress functions $\sigma(r)$ (wide disk)

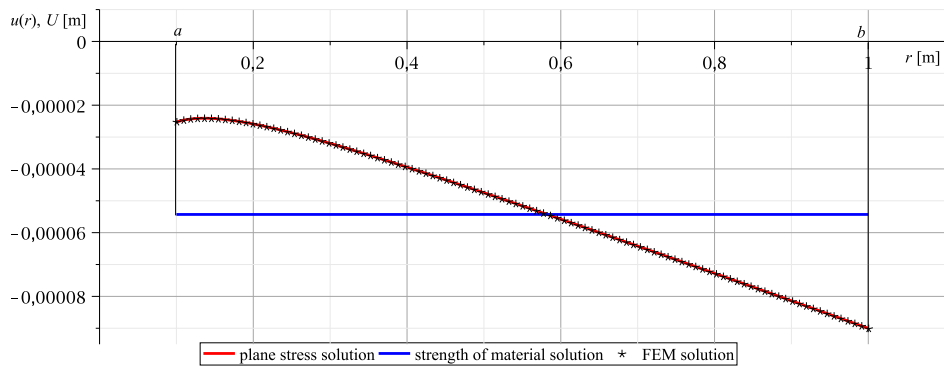


Figure 12. The plots of the radial displacement functions $u(r)$, U (wide disk)

It can be concluded that the plane stress solution and the FEM solution (plane stress model too) yield the same results for all of the stress and displacement functions as in the previous example 6.1. In this case the strength of material solution significantly differs from the plane stress results, as was expected.

7. CONCLUSIONS

The investigation of the state of stresses of a thin elastic disc is presented by applying two different mechanical models. The first model uses the governing equation of the plane stress deformation. The second model is a strength of material model. The results derived from the two models are in good agreement when the thin disk problem converges to a curved beam problem according to the geometrical parameters. When the disk becomes wider the results of the models diverge. Numerical examples illustrate the application of the derived formulae.

The results of the calculations illustrate that the radial and tangential normal stresses calculated with the two different models differ slightly when the thin disk can be considered as a curved beam according to the geometrical parameters. The same remark applies to radial displacements. The examples also represent the divergence of the stresses and the displacements derived from the two models in the case of a wide disk. The examples were also investigated with FEM analysis to check the results of the two models. The plane stress FEM analysis yields practically the same results as the analytical plane stress model in all examples investigated.

REFERENCES

1. SOKOLNIKOFF, I. S. *Mathematical Theory of Elasticity*. McGraw-Hill, New York, 1956.
2. TIMOSHENKO, S. and GOODIER, J. N. *Theory of Elasticity*. McGraw-Hill, New York, 1970.
3. SOUTHWELL, R. V. *An Introduction to the Theory of Elasticity*. Oxford University Press, Oxford, 1936.
4. LOVE, A. E. H. *A Treatise on Mathematical Theory of Elasticity*. University Press, Cambridge, 1952.
5. ECSEDI, I. and DLUHI, K. "A linear model for the static and dynamic analysis of non-homogeneous curved beams." *Applied Mathematical Modelling*, **29**(12), (2005), pp. 1211–1231. DOI: 10.1016/j.apm.2005.03.006.

NUMERICAL STUDY OF ICE ACCRETION ON BLADE SURFACE WITH VARYING CLOUD CHARACTERISTICS

IBRAHIM KIPNGENO ROTICH
Doctoral School of Environmental Sciences
Eötvös Loránd University, Budapest
ibrahimrkip@gmail.com

LÁSZLÓ E. KOLLÁR
Savaria Institute of Technology
Eötvös Loránd University, Budapest
kl@inf.elte.hu

[Received: January 28, 2024; Accepted: April 15, 2024]

Abstract. Wind turbines experience the threat of ice accretion under extreme weather conditions. A numerical modeling approach was applied using FENSAP ICE to simulate turbine blade icing and to determine the aerodynamic performance degradation due to ice accretion. Particular attention is paid to the combined effects of the cloud characteristics, i.e. median volume diameter (MVD), liquid water content (LWC) and ambient air temperature, in a relatively wide range that covers in-cloud icing and precipitation icing as well. Depending on these parameters, aerodynamic performance degradation may not occur proportionally with the increase in ice mass, which is discussed in detail. The accuracy of the numerical model is based on the number of shots, which is also studied. A single-shot approach means simulation of the icing event in a single step on the bare surface occurring over a period, whereas multi-shot involves multiple icing simulations, redefining the surface and applying mesh displacement after each shot. Such simulation considers that each additional layer of ice accretes on different iced surfaces. Numerical validation showed that a five-shot approach provided a close estimation of experimental results and was assessed sufficient for the study considering computational time and accuracy. The mass of ice accretion augments increases when LWC increases from 0.1 g/m^3 to 1 g/m^3 , and when MVD increases from $20 \mu\text{m}$ to $100 \mu\text{m}$, which results in the decrease of the lift-to-drag ratio (CL/CD) after a long enough accretion time. Higher ice mass leads to aerodynamic performance degradation; however, a slight increase in the ratio CL/CD may be observed after short accretion time for up to 20 minutes.

Keywords: Aerodynamic performance, ice accretion, liquid water content (LWC), median volume diameter (MVD), wind turbine

1. INTRODUCTION

Wind power is becoming a prevalent global source of electricity to reduce climate change effects [1–3]. However, wind energy penetration is affected by atmospheric conditions, location, and polar vortex [4]. The polar vortex expands during winters, sending colder air from the Arctic to mid-latitudes that can cause winter storms in areas that are not typically associated with cold. The cold spells associated with icing

conditions cause ice accumulation on wind turbine blades, reducing power production [5, 6]. The regions with high wind energy potential mainly lie in the cold climatic regions due to higher air densities that can increase power by about 10% [7, 8]. The icing regions pose a great danger to wind power production and energy transmission due to ice accumulation and ice load, which may lead to a shutdown or stall of wind turbines, affecting the grid stability [9]. The frequency of icing in a region greatly influences power production due to stall standby on turbines during icing days. Botta [10] presented a case of Acqua Spruzza Italy receiving 12 to 36 icing days per year. Maissan [11] studied the icing days of the Whitehorse region in Canada, with 33 to 50 icing days annually resulting in 20% estimated energy production loss. Dierer et al. [12] studied the icing frequency in the winter of 2009/2010 on an E-82 Enercon turbine in the Jura region of Switzerland, with results showing 11.5 and 41.5 days/year of meteorological icing and instrumental icing, respectively. The analyzed power reduction from the region with and without heating instruments on the blade showed a 3.5% and 10% annual power reduction, respectively. The impact of icing on wind energy involves wind power penalties because of structural vibrations of the overloaded component, which results in fatigue of wind turbine components, rotational imbalance, and an increase in drag force due to the formation of a new shape affecting the airflow [13, 14]. Paper [15] studied numerically the performance losses on an Aelos 30kW airfoil due to an icing event and obtained a result of 24% power loss from the 2D flow analysis; hence there is a need to study the power reduction due to icing.

Atmospheric icing conditions are responsible for ice accretion, which is characterized by physical and atmospheric parameters such as blade design (airfoil shape), temperature, air density, liquid water content (LWC), relative humidity, and median volume diameter (MVD) of droplets in the natural cloud that the wind turbine is exposed to [16–21]. The blade design is determined by size, rotational speed, impact angle on the root to tip of the airfoil, the droplet impingement area, and the angle of attack. Virk et al. [22] showed that blade size and the shape of the airfoil profile exposed to ice accretion influenced power loss due to aerodynamic performance degradation. Reid et al. [23] performed a study on the rotation of wind turbines under icing conditions, finding aerodynamic performance degradation leading to a 60% power reduction.

Icing conditions depend on the physical and atmospheric conditions, which are classified as in-cloud icing and precipitation icing. In-cloud icing is formed when the supercooled droplets collide with an object (e.g. a wind turbine blade), which changes the thermodynamic conditions, causing freezing. In-cloud icing results in rime ice or glaze ice, depending on the ambient parameters, principally the temperature, MVD, and LWC. Glaze ice is formed during wet ice growth associated with droplet diameter up to $500\ \mu\text{m}$ and high LWC, whereas rime ice is formed with temperatures below $-6\ \text{C}^\circ$, small MVD up to about 10, and lower LWC in the range of $0.1\ \text{g}/\text{m}^3$ [17, 22]. Paper [23] carried out a study on the performance degradation of a wind turbine using FENSAP-ICE with LWC of $0.5\ \text{g}/\text{m}^3$, MVD between $20 - 30\ \mu\text{m}$, temperature of $-3\ \text{C}^\circ$ and $-15\ \text{C}^\circ$ and accretion time between 10-60 minutes. They observed how

icing was influenced by atmospheric conditions and showed the relationship between the LWC, MVD, and temperature that results in similar icing conditions. The LWC decreases with increase in temperature in some scenarios [24].

Despite the challenges associated with the impact of icing on power production and targeting the increasing use of renewable energy, it is crucial to evaluate wind turbine performance under extreme weather conditions to obtain useful data to improve wind turbine performance in icing regions. Data collection on wind turbine icing is challenging due to unpredictable factors such as number of icing days, uncontrolled changes in atmospheric conditions, and inaccurate images captured by cameras [25]. The icing scenarios are studied by numerical tests applying computational fluid dynamics (CFD) and by laboratory tests in icing wind tunnels to predict ice formation under controlled conditions [26].

This study applies a numerical approach to model icing on a wind turbine blade section using ANSYS FENSAP ICE 2021/R2. The software applies a single-shot or multi-shot approach, the latter one providing more accurate but more costly computation. Raj et al. [27] studied the impact of number of shots for single shot, 4 shots and 8 shots and concluded that using multi-shots was more effective compared to a single shot. However, they did not focus on determining the minimum number of shots that can be used with minimal impact on the accuracy of aerodynamic performance. Wang et al. [28] carried out a numerical study on a NACA 0012 airfoil with shots between a single shot to 5 shots under varying icing conditions, but mostly focused on the impact of ice shapes.

In the present study, the ice accretion is simulated, and the optimum number of shots in the numerical model is determined, which provides acceptable accuracy and helps reduce computational time. The ice mass and the corresponding aerodynamic performance are evaluated under a wide enough range of cloud characteristics that covers substantially different icing conditions. The study will reveal how the aerodynamic performance considered by the lift-to-drag ratio changes with accretion time. The results provide beneficial information for researchers in the wind industry and contribute to more efficient energy production under extreme weather conditions.

2. NUMERICAL MODEL

2.1. Geometry and computational domain. The study employed a C-shaped computational domain around a NACA4412 airfoil. This shape was considered due to its moderate thickness, which can be used in several applications including aviation and wind turbines and thus providing versatility for numerical simulations under different conditions. The NACA 4412 airfoil with a 1 m chord length was defined and extruded 1 m in spanwise direction since FENSAP-ICE works with a 3D geometry, but the unsteady flow was simulated in the plane determined by the airfoil section. A fine 2D grid was created with 98,573 elements, a minimum orthogonal quality, and a maximum skew of 0.85 and 0.194 respectively. Triangular meshing in the domain was used in the study with a higher resolution near the blade surface for better accuracy, characterized by 1.05% growth of cells outwards, with dense elements and nodes occurring close to the wall. To accurately capture the flow phenomenon, the wall/airfoil

was divided into small domains (1000 units) all around and the inflation mesh of 27 layers was introduced with first layer thickness derived in ANSYS FENSAP-ICE (2017):

$$y^+ = \frac{yu_\tau}{\nu} = \frac{y}{\delta}, \quad (1)$$

where y is the distance from the wall to a point of interest, δ is the molecular viscous length scale, ν is the kinematic viscosity, and u_τ is the friction velocity.

The no-slip condition was achieved through the distance separation displayed on the number of layers and the boundary layer characteristic on the transition and separation which guided in the laminar-turbulent transition. The first layer thickness calculated was 1.46 m with a growth rate of 1.08% outwards to fully capture the complex ice shape and mass from the flow distribution over the surface and last inflation layer had a thickness of 1.9406×10^{-5} m. The number of layers was within the range specified in a study done by Piperas [29] (i.e. < 100 layers) for reducing the computational cost, especially in complex simulations, while maintaining the mesh quality.

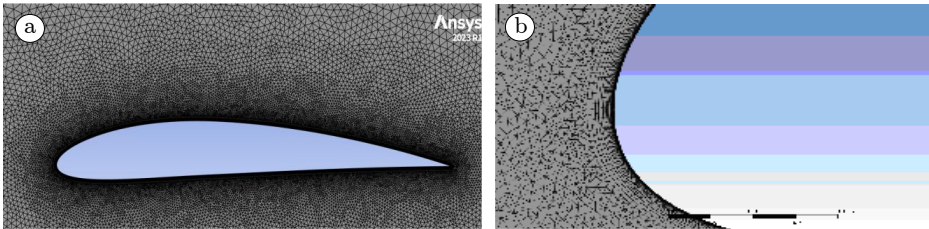


Figure 1. Mesh around the blade: (a) Fine, unstructured mesh (triangular mesh); (b) meshed domain near the leading edge

2.2. Boundary and flow conditions. The boundary conditions play an important role in the accuracy and reliability of the simulation by describing the inlet, outlet, wall, and symmetry conditions. The boundary conditions used in the study employed the Dirichlet and Neumann conditions in specifying the value of the solution and the derivative of the solution, respectively. The inlet condition is specified as the velocity with 20 m/s used in the study, the outlet condition specifies the pressure or the backflow condition in the outlet, and the gage pressure was set to 0 Pa. The ambient temperature in the freestream was defined as $-5\text{ }^\circ\text{C}$, $-10\text{ }^\circ\text{C}$ and $-20\text{ }^\circ\text{C}$. The airfoil in the study was set to be an obstacle with wall temperature initialized by isothermal conditions at $+0.1\text{ }^\circ\text{C}$ higher than freestream ambient temperature, while the symmetry conditions are used to describe the boundaries within which the flow occurs. These boundary conditions are indicated in Figure 2. Based on studies done by Abdalkarem et al. [30] and Manni et al. [31], it was found that utilizing the

computational domain having a distance of 10 to 15 times chord length downstream was ideal for the study. The distance upstream from the leading edge was set at 5-chord lengths, while downstream from the trailing edge to the end of domain at 10-chord lengths.

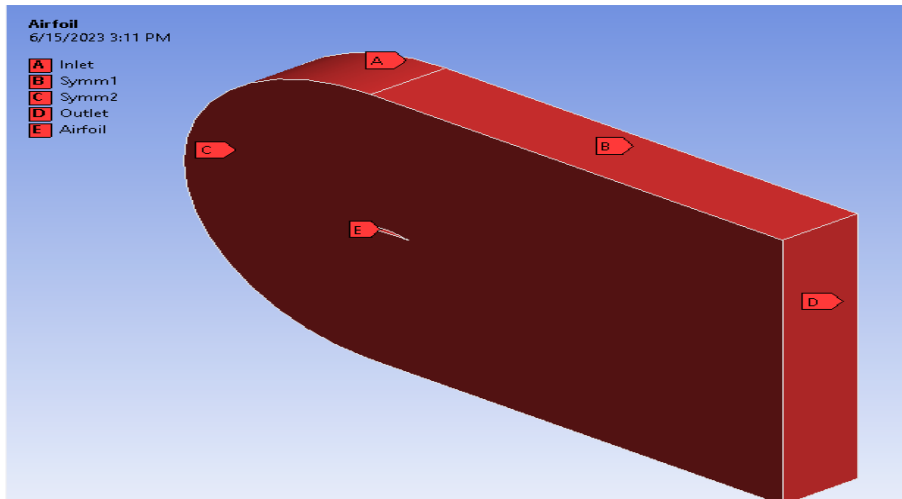


Figure 2. C-shaped computational domain

2.3. Icing model. Icing is a complex phenomenon involving phase change and thermodynamic and fluid dynamic processes when the supercooled droplets hit the surface and accrete. The rate of icing is calculated using FENSAP-ICE, as summarized in the following steps. First, the flow around the airfoil is determined by the flow solver (FENSAP), then the motion of droplets is simulated by the droplet's solver (DROP3D), and finally icing is modeled by the ice accretion and water runback module (ICE3D).

The cloud that leads to ice accretion is modeled by multiphase flow over the airfoil surface governed by Reynolds-Averaged Navier-Stokes (RANS) equations coupled with Lagrangian particle tracking. The continuity equation ensures that the mass of the fluid is conserved within the simulation domain, while the momentum equation describes the conservation of momentum within the fluid. The k -turbulence model was used in the present study, which derived the dynamic eddy viscosity and the bulk fluid viscosity over the fluid flow. This model was developed by Menter to blend the robust and accurate nature of $k \cdots \omega$ model in near-wall region varying with models, i.e., $k \cdots \varepsilon$ and $k \cdots \omega$ [32, 33]. The blending function on the $k \cdots \omega$ SST model is used for smooth transition between the models based on the distance from the wall. The $k \cdots \varepsilon$ is suitable for capturing turbulent regions in far distances, while $k \cdots \omega$ is activated near the wall where boundary layer turbulence is significant, and is thus able to resolve flow dynamics.

Water droplet trajectories near the surface are modeled by the droplet equation, which describes the motion of individual droplets in a fluid based on the assumptions

that droplets do not collide, coalesce, or splash until they reach the surface. Numerically, the ice accretion involves a multiphase-flow approach involving the tracking of trajectories of supercooled water droplets, which determines the collection efficiency on the surface, followed by the heat transfer governing the air-liquid-solid phase change and ice accretion on the airfoil. The ice characteristics based on the physical and atmospheric conditions determines the type of ice as described in Ibrahim et al. [17] and Rotich & Kollár [19]. Factors which mainly affect the accretion process include the atmospheric conditions (microphysics) described by the ambient temperature T_a , liquid water content (LWC), and median volume diameter (MVD), whereas physical components include airfoil configuration (angle of attack).

The thermodynamics of the ice accretion process as described in Makkonen et al. [34] determine the accretion efficiency that affects the rate of icing. Icing over the surface was numerically simulated after defining the atmospheric conditions influencing the aerodynamic performance and ice shapes. The controlled conditions set were air temperature (-5 , -10 , and -20 -20°C), LWC (0.1 g/m^3 , 0.5 g/m^3 , and 1 g/m^3), MVD (20 , 40 , 60 , 80 and $100\text{ }\mu\text{m}$) at 0° angle of attack and accretion time of 3 hours. The numerical parameter, the number of shots in the simulation of the icing, was varied from a single shot to multi-shot including 3-5-8 shots, which has an impact on the ice shape and mass and the aerodynamic performance degradation. A single-shot simulation involves constant one-interval ice accretion over a given time, while a multi-shot approach is divided into shorter-interval icing solutions obtained after dividing the total icing time by the number of shots (3600 , 2160 and 1350 seconds for 3, 5 and 8 shots, respectively, in this study). Grid on the airfoil surface is defined in the first shot, and then it is displaced in each shot according to the iced airfoil profile, with more shots causing formation of a more complex shape. Atmospheric conditions are set in each shot, then the droplet impingement is simulated on the iced surface, further ice accretion is predicted, and the aerodynamic performance of the iced blade is determined.

3. RESULTS AND DISCUSSION

The airfoil section studied was NACA4412. The FENSAP solver computed flow field solutions, while the droplet trajectories were calculated in DROP3D after setting up the conditions determined by the MVD, LWC, and droplet size distribution (Langmuir D) of the cloud. Icing prediction was based on numerical calculations in the ICE3D. The numerical model will be validated first in this section, followed by analyzing the impact of number of shots on icing and on aerodynamic performance. Finally, the effects of MVD, LWC, and air temperature will be discussed.

3.1. Validation of the numerical model. The grid independence study was carried out to determine the number of divisions and elements in the mesh generated. The classification of the refinement was done based on the number of divisions in the domain.

According to a study conducted by Roache [35], the accuracy of numerical solutions may be assessed using the discretization method. The estimation on the accuracy

Table 1. Grid refinement ratio obtained depending on the number of elements

Divisions	35	100	400	800	1200	1500	2000
Elements	84525	87845	181215	354330	497515	651970	900990
Refinement ratio		1.039278	2.062895	1.955302	1.404101	1.310453	1.38195

of solution was based on calculating the grid refinement ratios. According to Roache, using Richardson extrapolation theory (Celik et al. [36]) a refinement ratio greater than 1.3 was ideal for numerical studies. In the present scenario, medium/coarse was not found to be ideal since the refinement ratio was 1.039; however, it increased to 2.063 for fine/medium, which was found to be excellent.

The lift-to-drag ratio is plotted as a function of the number of elements in Figure 3 to show that the aerodynamic performance is not affected by further increasing the number of divisions above the chosen value.

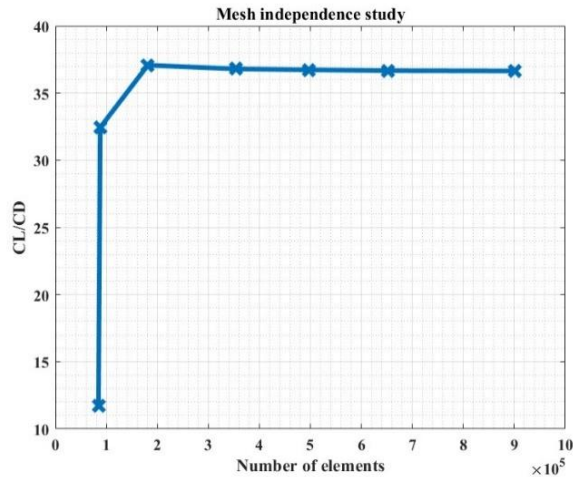


Figure 3. Results of grid independence study regarding lift-to-drag ratio

The numerical model was validated by an experimental study carried out in a low-speed wind tunnel by Sundaresan et al. [37] using the NACA0012 airfoil. The conditions used in the experimental study were wind speed of 77 m/s, MVD of $20 \mu\text{m}$, LWC of 0.5 g/m^3 and 16.9 minutes accretion time for an airfoil with 0.533 m chord length, which was duplicated and numerically simulated on FENSAP-ICE software. In the numerical study, single shot and 3-5-8 shot simulations were applied. Figure 4 shows that similar ice shapes were obtained after the 5-shot and 8-shot simulations. The single-shot and 3-shot simulations slightly underestimate the amount of ice on the upper half of the profile, and they predict the maximum ice thickness at a lower position. However, the simulations with five and eight shots

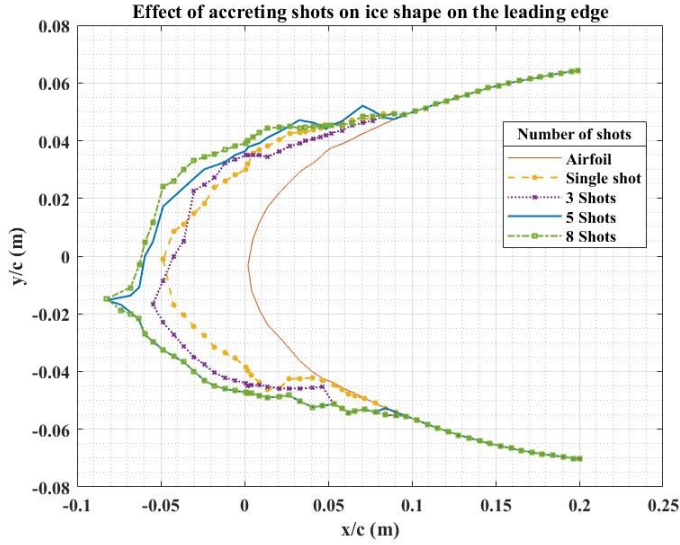


Figure 4. Comparison of ice accretions on NACA 4412 profile obtained numerically for single-shot and multi-shot simulations

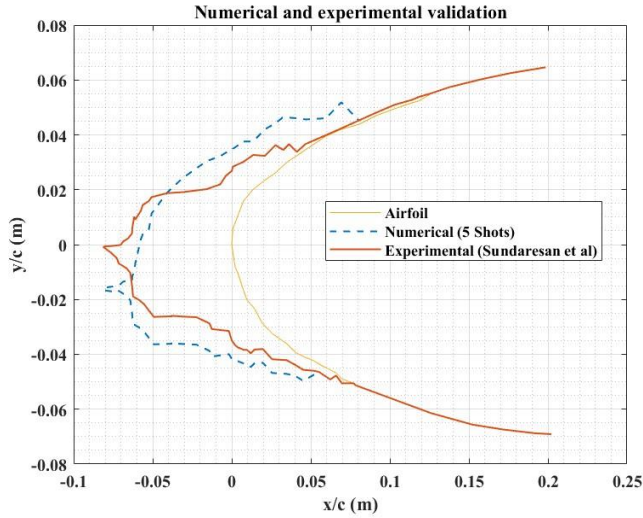


Figure 5. Comparison of numerical results (5 shots) obtained by FENSAP-ICE 2021 R2 with experimental data from low-speed subsonic wind tunnel facility (Sundaresan et al. [37]) from airfoil generated by Jacobs et al. [38].

provide a nearly similar shape of ice formed on the leading edge to that obtained experimentally, as can be compared in Figure 5.

3.2. Impact of number of shots on the accuracy of model prediction. The atmospheric and physical conditions listed in Section 2.2 were assumed in the numerical study and were introduced in FENSAP-ICE. The assumptions made in the study were that droplets were spherical and no coalescence, splashing/bouncing, or fragmentation or disruption occurred in the simulation of a three-hour ice accretion event. In the following, the changes in the ice mass and in the lift-to-drag ratio when increasing the number of shots are compared.

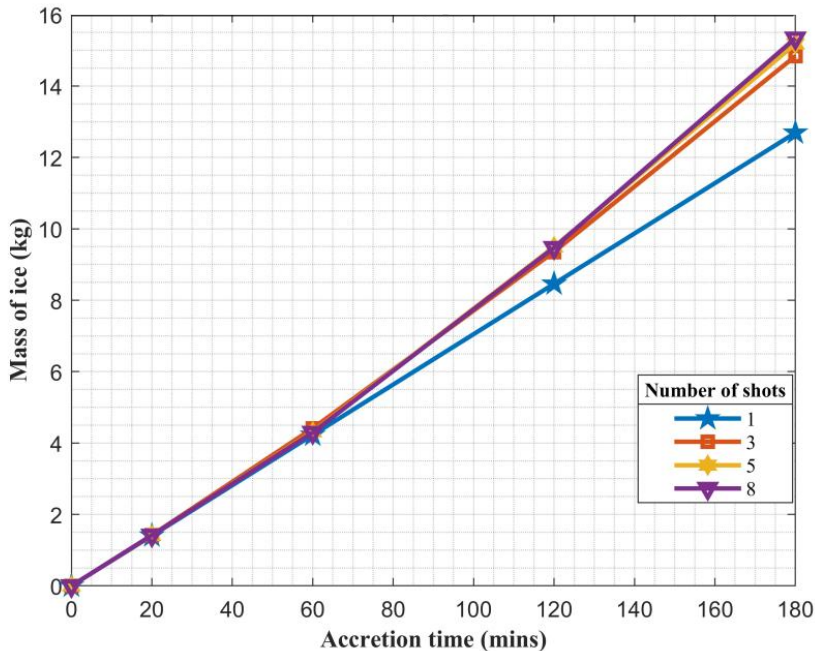


Figure 6. Effect of number of shots on the mass of ice for different accretion times (mins), for LWC 1 g/m^3 , MVD $100 \mu\text{m}$ and air temperature -10°C

According to Figure 5, the ice mass did not vary significantly with the number of shots, except between the single-shot and multi-shot simulations after long accretion time. The differences after 180 imin accretion time for an MVD of $100 \mu\text{m}$ were 14.88% between 1 and 3 shots, 2.24% between 3 and 5 shots, and 1.04% between 5 and 8 shots. The ice accretion depended on the number of shots and affected the flow over the surface, forming a more streamlined shape on the leading edge for the single shot. The mass of ice increases with the number of shots, and once the prediction of ice shape becomes accurate enough, the ice mass does not change considerably with the number of shots. The aerodynamic performance degradation

may be evaluated by the reduction in the lift-to-drag ratio CL/CD . Figure 7 reveals how this parameter varied with the number of shots for different values of LWC. The variation in the lift-to-drag ratio with the number of shots is below 5% for the smallest LWC, as seen for 0.1 g/m^3 . However, it is 20-50% for higher LWC when increasing the number of shots up to 5, and then further increasing the number of shots from 5 to 8, the change reduces to around or below 5%.

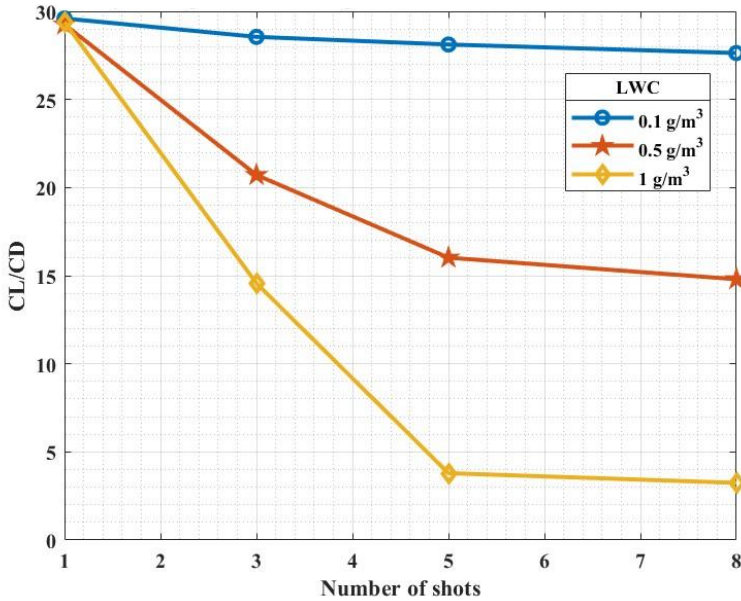


Figure 7. Effect of the number of shots on aerodynamic performance for MVD $60 \mu\text{m}$, accretion time 180 minuts, air temperature -10°C , and for different values of LWC g/m^3

The lift-to-drag ratio reduces significantly when the number of shots increases up to five. However, no significant difference can be observed between the lift-to-drag ratios obtained with the five- and the eight-shot simulations. Consequently, increasing the number of shots above five does not lead to further considerable change in ice shape or in aerodynamic performance degradation. Furthermore, a high number of shots leads to numerical instability, as was observed in some simulations that were run with 20 shots [39]. Therefore, this study employs five shots in the following in order not to overly increase the computation time and to avoid numerical problems.

3.3. Effects of MVD and LWC. The icing rate and mass of ice accreting on the airfoil depend on atmospheric conditions described by parameters such as LWC and MVD. When LWC and MVD are small, fewer droplets freeze, causing a slower accretion process on the surface, whereas large-diameter droplets collide more efficiently, and then they freeze, leading to an increase in ice mass. The inertial forces have little

effect on small droplets that follow the streamlines, while greater droplets have higher inertia, causing increasing collision efficiency and impingement of a higher number of droplets. The collision efficiency is influenced by the droplet diameter, and the accretion efficiency depends on the availability of water on the surface that creates the nucleation sites for ice growth.

The ice mass was found to increase approximately linearly with the LWC, MVD, and accretion time (see Figure 8). These observations correspond to those reported in the studies by Hakimian et al. [40], Molkoselka et al. [41], and Tsao & Anderson, [42].

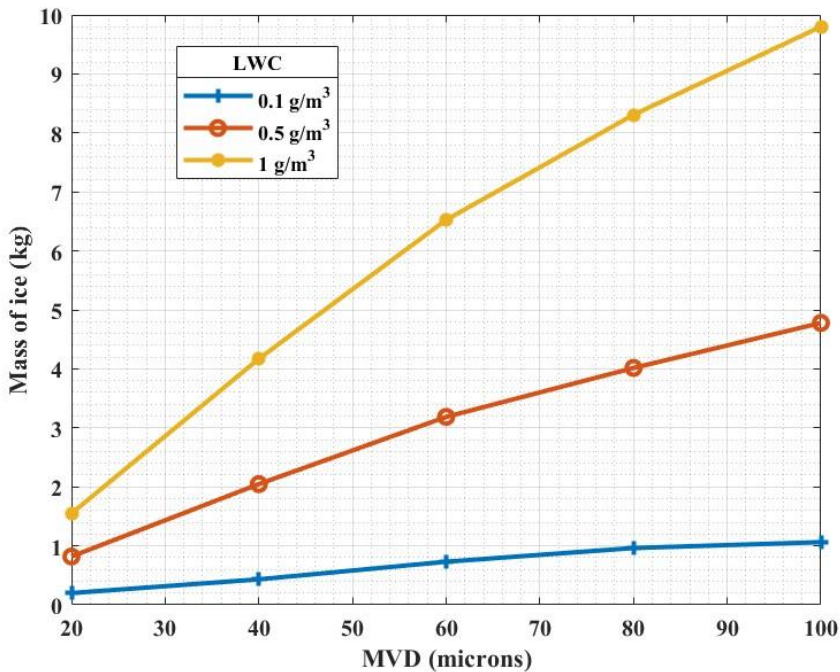


Figure 8. Effect of the number of shots on aerodynamic performance for MVD $60 \mu\text{m}$, accretion time 180 minutes, air temperature -10°C , and for different values of LWC g/m^3

Figure 8 represents how the accreted ice mass is affected by MVD and LWC. As MVD and LWC increase, the collection efficiency on the airfoil surface increases leading to more ice accreting on the leading edge. The horn formation that can be seen in Figure 9 is substantially influenced by the droplet diameter. The ice accreted on the surface for lower MVD causes little or no noticeable flow separation compared to the ice accretion obtained for higher MVD, which forms a complex shape creating recirculation flow. The iced airfoil shape alters the flow over the surface, increasing the drag and resulting in a separation region further along the upper profile behind the leading edge.

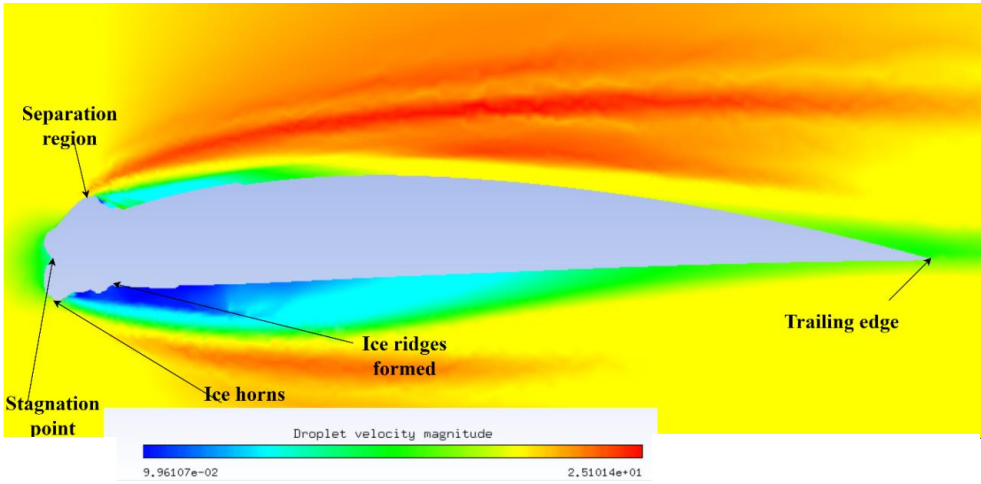


Figure 9. Flow distribution disturbance caused by ridges of ice accretion, for LWC 0.5 g/m^3 , MVD $100 \mu\text{m}$, air temperature -20°C , accretion time 180 minutes

Ice accretion causes aerodynamic degradation, since the lift decreases and the drag increases. However, an unexpected tendency was observed after a short accretion time. A small amount of ice on the blade may even slightly increase the lift-to-drag ratio, which is followed by a steep decrease after further ice accretion due to shift of the stagnation point (Rotich & Kollár [19]) and the flow separation described in the previous paragraph. These tendencies can be observed in Figure 10, where

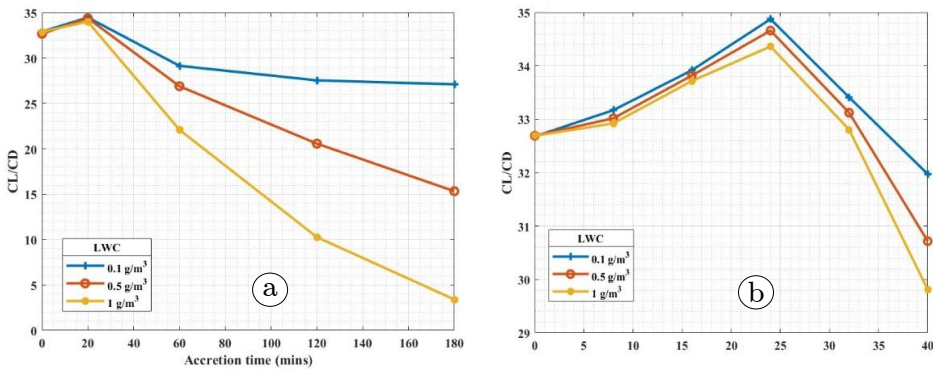


Figure 10. Variation of lift-to-drag ratio with accretion time (mins) for different values of LWC, at MVD $60 \mu\text{m}$ and air temperature -10°C : (a) accretion time is 180 min; (b) short accretion times up to 40 minutes

results of simulations with smaller time intervals are shown in Figure 10(b). The aerodynamic degradation in 180-minute accretion time is greatly affected by the LWC. The reduction in the lift-to-drag ratio is less than 20% for the smallest LWC, while it drops to about one tenth for the highest LWC. The ice type on the surface is mainly determined by the LWC and MVD. Rime ice is formed when droplets are small and LWC is low, whereas higher LWC and MVD increase the chance of forming glaze ice due to the higher water content available on the surface, leading to incomplete freezing. The ice shape is also greatly affected by MVD and LWC. Bigger droplets result in greater collision efficiency, leading to increased ice accretion with the appearance of horns and less streamlined airfoils (Virk et al. [43]). An increase in LWC results in a higher amount of liquid water on the surface, which influences the type of accreting ice and worsens the aerodynamic characteristics.

3.4. Effects of air temperature. The atmospheric temperature influences the rate of icing and the type of ice on the airfoil surface. At higher temperatures, the heat transfer is not enough to freeze all droplets upon impact, causing some runback water on the airfoil surface leading to glaze ice. At lower temperatures, the supercooled water droplets freeze immediately upon impact, causing rime ice. The effect of temperature on ice shape and aerodynamic performance was studied on -5°C , -10°C , and -20°C (Figure 11). In FENSAP-ICE, the icing solver considers the heat balance

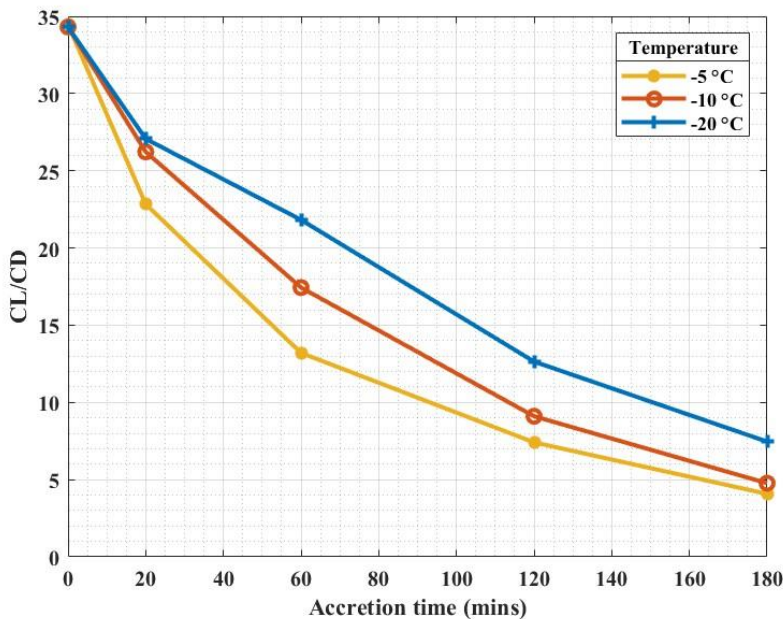


Figure 11. Effect of air temperature on lift-to-drag ratio for MVD $80\ \mu\text{m}$ and for LWC $1\ \text{g}/\text{m}^3$

between the liquid water and the accreted surface. Figure 11 shows how the lift-to-drag ratio reduces with accretion time for different values of air temperature. Since the LWC is high (i.e. 1 g/m^3), the lift-to-drag ratio decreases considerably with accretion time, but this decreasing tendency is faster at higher temperatures. Contrary to the results presented in Figure 9, the increasing tendency of the lift-to-drag ratio after the first 20 min accretion time cannot be observed in Figure 11. This may be explained by the higher MVD and high LWC. The ice in this case change the shape of the profile so that aerodynamic performance degradation occurs after even a few minutes of accretion.

The air temperature affects the ice formation and the water film on the surface (Orchard et al. [44]); thus, different shapes are formed at the leading edge for different air temperatures. At lower temperatures, the shape of the ice is more streamlined, while at higher temperatures, the ice has a 'horny' shape, as can be observed in Figure 12, and such changes in the shape influence the flow, and thus the aerodynamic performance.

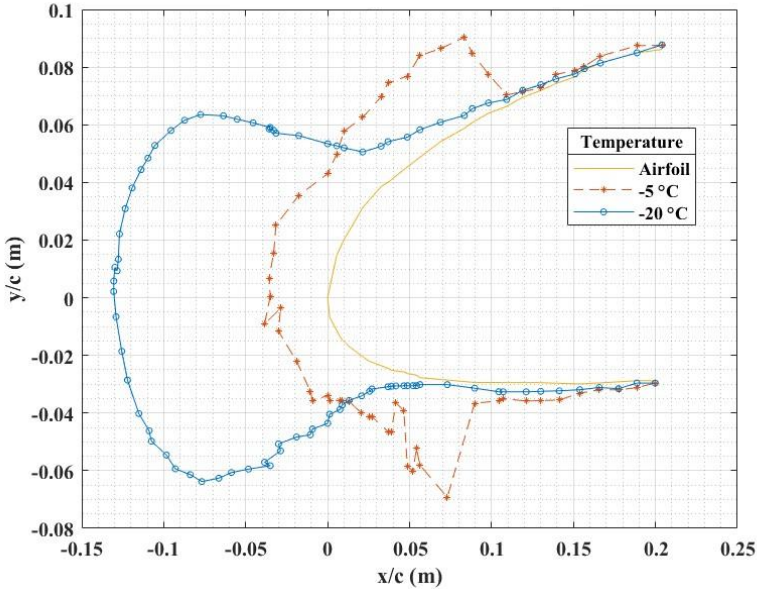


Figure 12. Effect of temperature on ice shape for MVD $80 \mu\text{m}$, LWC 1 g/m^3 , at 180 minutes for -5°C and -20°C

4. CONCLUSIONS

Ice accretion on the NACA4412 airfoil and the resulting aerodynamic performance degradation were modeled numerically. The optimum number of shots in the numerical simulation was determined and the effects of physical parameters describing

the ambient conditions and the characteristics of the cloud were studied, including MVD, LWC, air temperature, and accretion time. The numerical approach was validated with experimental results, and the 5-shot and 8-shot approaches provided close prediction of ice shape and lift-to-drag ratio contrary to the single-shot and 3-shot simulations. The single-shot approach was found to be inaccurate for estimating ice mass after a long accretion time.

- i The lift-to-drag ratio changed considerably when the number of shots increased up to 5; however, further increasing it to 8 resulted in a change of 5% or less. Consequently, the 5-shot approach was chosen for further simulations.
- ii The MVD was varied from 20 mm to 100 mm, at 10 μm intervals, whereas the LWC was changed from 0.1 g/m^3 to 1 g/m^3 . Simulation results showed that ice mass increased with both parameters. Aerodynamic performance degradation was concluded to be more significant for higher values of MVD and LWC.
- iii An interesting property was also observed depending on the ambient parameters. The lift-to-drag ratio that was used to describe aerodynamic performance slightly increased after a short period of ice accretion (i.e., up to 20-25 minutes), and dropped only after further ice accretion. Thus, a small amount of ice may not cause aerodynamic performance degradation at smaller values of MVD and LWC.
- iv The air temperature influences ice formation, since horny shapes develop for higher temperature, i.e., when the temperature is closer to the freezing point. Consequently, the lift-to-drag ratio reduces to lower values for higher air temperatures.

Further research will include experimental study of the effects of the ambient parameters on ice accretion in an icing wind tunnel and the consideration of these results in the design of blade shapes. Such observations would contribute to extending the operation of wind turbines under icing conditions.

Acknowledgement. Project no. TKP2021-NVA-29 has been implemented with support provided by the Ministry of Culture and Innovation of Hungary from the National Research, Development, and Innovation Fund, financed under the TKP2021-NVA funding scheme.

REFERENCES

1. JUNG, C. and SCHINDLER, D. "Development of onshore wind turbine fleet counteracts climate change-induced reduction in global capacity factor." *Nature Energy*, **7**, (2022), 608–619. DOI: 10.1038/s41560-022-01056-z.
2. ROTICH, I. K. and MUSYIMI, P. K. "Wind power density characterization in arid and semi-arid Taita-Taveta and Garissa counties of Kenya." *Cleaner Engineering and Technology*, (2023), p. 100704. DOI: 10.1016/j.clet.2023.100704.
3. SUMAN, A. "Role of renewable energy technologies in climate change adaptation and mitigation: A brief review from Nepal." *Renewable and Sustainable Energy Reviews*, **151**, (2021), p. 111524. DOI: 10.1016/j.rser.2021.111524.

4. SALAM, A., ALSABAGH, Y., XU, Y., VIRK, M. S., SUMAN, A. and BAD-RAN, O. “Atmospheric ice loading and its impact on natural frequencies of wind turbines. Wind Engineering.” *Wind Engineering*, **39**(1), (2015), 83–96. DOI: 10.2307/90006861.
5. ZHANG, J., YUE, P., ZHANG, Q. and WANG, Z. “Impact of tropospheric polar vortex on winter cold extremes over Northeast China.” *Atmospheric Research*, **294**, (2023), p. 106942. DOI: 10.1016/j.atmosres.2023.106942.
6. CHUANG, Z., YI, H., CHANG, X., LIU, H., ZHANG, H. and XIA, L. “Comprehensive analysis of the impact of the icing of Wind turbine blades on power loss in cold regions.” *Journal of Marine Science and Engineering*, **11**(6), (2023), p. 1125. DOI: 10.3390/jmse11061125.
7. FORTIN, G., PERRON, J. and ILINCA, A. *Behaviour and modeling of cup anemometers under icing conditions*. IWAIS XI. URL: <https://www.researchgate.net/publication/259758149>.
8. FU, P. and FARZANEH, M. “A CFD approach for modeling the rime-ice accretion process on a horizontal-axis wind turbine.” *Journal of Wind Engineering and Industrial Aerodynamics*, **98**(4-5), (2010), 181–188. DOI: 10.1016/j.jweia.2009.10.014.
9. GAO, L. and HONG, J. “Wind turbine performance in natural icing environments: A field characterization.” *Cold Regions Science and Technology*, **181**, (2011), p. 103193. DOI: j.coldregions.2020.103193.
10. BOTTA, G., CAVALIERE, M. and HOLTINEN, H. *Ice accretion at Acqua Spruzza and its effects on wind turbine operation and loss of energy production*. BOREAS IV. URL: <https://www.researchgate.net/publication/265244514>.
11. MAISSAN, J. F. “Wind power development in sub-arctic conditions with severe rime icing.” *Circumpolar Climate Change Summit and Exposition*, (2011), 174–183. URL: <https://thenorthernreview.ca/index.php/nr/article/view/233/226>.
12. DIERER, S., OECHSLIN, R. and CATTIN, R. “Wind turbines in icing conditions: performance and prediction.” *Advances in Science and Research*, **6**(1), (2011), 245–250. DOI: 10.5194/asr-6-245-2011.
13. KOLLAR, L. E. and MISHRA, R. “Inverse design of wind turbine blade sections for operation under icing conditions.” *Energy Conversion and Management*, **180**, (2019), 844–858. DOI: 10.1016/j.enconman.2018.11.015.
14. MANATBAYEV, R., BAIZHUMA, Z., BOLEGENOVA, S. and GEORGIEV, A. “Numerical simulations on static vertical axis wind turbine blade icing.” *Renewable Energy*, **170**, (2021), 997–1007. DOI: 10.1016/j.renene.2021.02.023.
15. YIRTICI, O., TUNCER, I. H. and OZGEN, S. “Ice accretion prediction on wind turbines and consequent power losses.” *Journal of Physics: Conference Series*, **753**, (2016). DOI: 10.1088/1742-6596/753/2/022022.
16. DHYANI, A., CHOI, W., GOLOVIN, K. and TUTEJA, A. “Surface design strategies for mitigating ice and snow accretion.” *Matter*, **5**(5), (2021), 1423–1454. DOI: 10.1016/j.matt.2022.04.012.
17. IBRAHIM, G. M., POPE, K. and MUZYCHKA, Y. S. “Effects of blade design on ice accretion for horizontal axis wind turbines.” *Journal of Wind Engineering*

- and Industrial Aerodynamics*, **173**, (2018), 39–52. DOI: 10.1016/j.jweia.2017.11.024.
18. KRAJ, A. G. and BIBEAU, E. L. “Phases of icing on wind turbine blades characterized by ice accumulation.” *Renewable Energy*, **35**(5), (2010), 966–972. DOI: 10.1016/j.renene.2009.09.013.
 19. ROTICH, I. and KOLLÁR, L. E. “Numerical simulation of the performance of an asymmetrical airfoil under extreme weather conditions.” *Mérnöki És Informatikai Megoldások*, **3**(2), (2022), 19–29. DOI: 10.37775/EIS.2022.2.2.
 20. STRAUSS, L., SERAFIN, S. and DORNINGER, M. “Probability forecasts of ice accretion on wind turbines derived from multiphysics and neighbourhood ensembles.” *Quarterly Journal of the Royal Meteorological Society*, **148**(746), (2022), 2446–2467. DOI: 10.1002/qj.4311.
 21. SWENSON, L., GAO, L., HONG, J. and SHEN, L. “An efficacious model for predicting icing-induced energy loss for wind turbines.” *Applied Energy*, **305**, (2022), p. 117809. DOI: 10.1016/j.apenergy.2021.117809.
 22. VIRK, M., HOMOLA, M. and NICKLASSON, P. “Atmospheric icing on large wind turbine blades.” *International Journal of Energy and Environment*, **3**(2), (2012), pp. 1–8.
 23. REID, T., BARUZZI, G., OZCER, I., SWITCHENKO, D. and HABASHI, W. *FENSAP-ICE simulation of icing on wind turbine blades, Part 1: performance degradation*. 51st AIAA Aerospace Sciences Meeting Including the New Horizons Forum and Aerospace Exposition, Jan. 7. DOI: 10.2514/6.2013-750.
 24. LIU, Y., ZHANG, K., TIAN, W. and HU, H. “An experimental investigation on the dynamic ice accretion and unsteady heat transfer over an airfoil surface with embedded initial ice roughness.” *International Journal of Heat and Mass Transfer*, **146**, (2020), p. 118900. DOI: 10.1016/j.ijheatmasstransfer.2019.118900.
 25. HAN, Y., PALACIOS, J. and SCHMITZ, S. “Scaled ice accretion experiments on a rotating wind turbine blade.” *Journal of Wind Engineering and Industrial Aerodynamics*, **109**, (2012), 55–67. DOI: 10.1016/j.jweia.2012.06.001.
 26. HOMOLA, M. C., VIRK, M. S., WALLENUS, T., NICKLASSON, P. J. and SUNDSBØ, P. A. “Effect of atmospheric temperature and droplet size variation on ice accretion of wind turbine blades.” *Journal of Wind Engineering and Industrial Aerodynamics*, **98**(12), (2010), 724–729. DOI: 10.1016/j.jweia.2010.06.007.
 27. RAJ, L., YEE, K. and MYONG, R. S. “Sensitivity of ice accretion and aerodynamic performance degradation to critical physical and modeling parameters affecting airfoil icing.” *Aerospace Science and Technology*, **98**, (2020), p. 105659. DOI: 10.1016/j.ast.2019.105659.
 28. WANG, Q., YI, X., LIU, Y., REN, J., LI, W., WANG, Q. and LAI, Q. “Simulation and analysis of wind turbine ice accretion under yaw condition via an improved multi-shot icing computational model.” *Renewable Energy*, **162**, (2020), 1854–1873. DOI: 10.1016/j.renene.2020.09.107.

29. PIPERAS, A. T. “Investigation of boundary layer suction on a wind turbine airfoil using CFD (MSc thesis).” PhD thesis. Technical University of Denmark, 2010.
30. ABDALKAREM, A. A. M., ABDULLAH, A. F., SOPIAN, K., HAW, L. C., MUZAMMIL, W. K. and WONG, K. H. “The effect of trailing-edge wedge-tails on the aerodynamic characteristics of wind turbine airfoil.” *IOP Conference Series: Materials Science and Engineering*, **1278**(1), (2023), p. 012011. DOI: 10.1088/1757-899X/1278/1/012011.
31. MANNI, L., NISHINO, T. and DELAFIN, P. L. “Numerical study of airfoil stall cells using a very wide computational domain.” *Computers & Fluids*, **140**, (2016), pp. 260–269. DOI: 10.1016/j.compfluid.2016.09.023.
32. MARTINI, F., IBRAHIM, H., CONTRERAS MONTOYA, L. T., RIZK, P. and ILINCA, A. “Turbulence modeling of iced wind turbine airfoils.” *Energies*, **15**(22), (2016), p. 8325. DOI: 10.3390/en15228325.
33. MENTER, F. *Zonal two equation $k-\omega$ turbulence models for aerodynamic flows*. 23rd Fluid Dynamics, Plasmadynamics, and Lasers Conference, July 6. DOI: 10.2514/6.1993-2906.
34. MAKKONEN, L., LAAKSO, T., MARJANIEMI, M. and ILINCA, A. “Modelling and prevention of ice accretion on wind turbines.” *Wind Engineering*, **25**(1), (2001), pp. 3–21. DOI: 10.1260/0309524011495791.
35. ROACHE, P. J. “Perspective: A method for uniform reporting of grid refinement studies.” *Journal of Fluids Engineering*, **116**(3), (1994), pp. 405–413. DOI: 10.1115/1.2910291.
36. CELIK ISMAIL B., GHIA URMILA, ROACHE PATRICK J., FREITAS CHRISTOPHER J., COLEMAN HUGH and PETER E. RAAD. “Procedure for estimation and reporting of uncertainty due to discretization in CFD applications.” *Journal of Fluids Engineering*, **130**(7), (2008), p. 078001. DOI: 10.1115/1.2960953.
37. SUNDARESAN, A., ARUNVINTHAN, S., PASHA, A. A. and PILLAI, S. N. “Effect of ice accretion on the aerodynamic characteristics of wind turbine blades.” *Wind and Structures, An International Journal*, **32**(8), (2021), 205–217. DOI: 10.12989/was.2021.32.3.205.
38. JACOBS, E. N., WARD, K. E. and PINKERTON, R. M. *The characteristics of 78 related airfoil sections from tests in the variable-density wind tunnel*. in NASA. 1935.
39. ROTICH, I. and KOLLÁR, L. “Numerical simulation of the performance of an asymmetrical airfoil under extreme weather conditions.” *Mérnöki és Informatikai Megoldások*, **3**(2), (2013), pp. 19–29. DOI: 10.37775/EIS.2022.2.2.
40. HAKIMIAN, A., NAZIFI, S. and GHASEMI, H. *Ice Adhesion: Mechanism, Measurement and Mitigation*. Ed. by K. L. Mittal and C. H. Choi. Wiley, 2020. Chap. Physics of Ice Nucleation and Growth on a Surface, 87–110. DOI: 10.1002/9781119640523.ch3.
41. MOLKOSELKA, E., KAIKKONEN, V. and MAKYNEN, A. *Instrument and method for measuring ice accretion in mixed-phase cloud conditions*. IEEE International Instrumentation and Measurement Technology Conference (I2MTC). 1-5., 2020. URL: 10.1109/I2MTC43012.2020.9129604.

-
42. TSAO, J. C. and ANDERSON, D. N. *Additional study of water droplet median volume diameter (MVD) effects on ice shapes*. NASA, 2005. URL: <http://www.sti.nasa.gov>.
 43. VIRK, M. S., HOMOLA, M. C. and NICKLASSON, P. J. “Effect of rime ice accretion on aerodynamic characteristics of wind turbine blade profiles.” *Wind Engineering*, **34**(2), (2010), 207–218. DOI: 10.1260/0309-524X.34.2.207.
 44. ORCHARD, D. M., CLARK, C. and CHEVRETTE, G. “Measurement of liquid water content for supercooled large drop conditions in the NRC’s altitude icing wind tunnel.” *The Japan Society for Aeronautical and Space Sciences* **54**(6), (2013), 175–186. DOI: 10.4271/2019-01-2007.

ANALYSIS OF OVERCORING IN SITU STRESS MEASUREMENT METHODS USING FINITE ELEMENT SIMULATIONS

DÁVID BORZA

Department of Energy Engineering, Faculty of Mechanical Engineering,
Budapest University of Technology and Economics
Műgyetem rkp. 3, 1111 Budapest, Hungary
borza.david@edu.bme.hu

DONÁT M. TAKÁCS

Department of Energy Engineering, Faculty of Mechanical Engineering,
Budapest University of Technology and Economics
Műgyetem rkp. 3, 1111 Budapest, Hungary
Montavid Thermodynamic Research Group
c/o ETTE, Lovas út 18., Budapest, 1012, Hungary
takacs@energia.bme.hu

[Received: March 20, 2024; Accepted: August 6, 2024]

Abstract. Two commonly used overcoring measurement methods for estimating the in situ stress state in rocks – the In Situ Stress Testing (IST) gauge and the Hollow Inclusion (HI) cell – are compared based on finite element models. The models simulate idealized measurement circumstances in homogeneous, isotropic and linearly elastic rocks during overcoring, and are used to evaluate the maximum accuracy achievable using the two methods. We show that while both methods are capable of accurately estimating the in situ stress state, their accuracy depends significantly on the placement of the instruments within the pilot hole. Recommendations regarding optimal instrument placement are given for both methods by considering stress disturbances created by the bore- and pilot holes.

1. INTRODUCTION

Estimation of the undisturbed underground or in situ stress state is essential to underground operations, such as mining, tunnelling and other geotechnical engineering projects. Since the in situ stress state is influenced by factors such as depth, tectonic forces, topography, constitutive behaviour of the rock, and the local geological history, among others [1], measurements are necessary to estimate the state of stress underground.

There are several techniques to determine the in situ stress state [2–4]. Hydraulic methods, such as hydraulic fracturing and the flat jack method, are based on pressure measurements. Their advantage is that these methods do not require knowledge of the material properties of the rock. On the other hand, they do not provide enough information to accurately estimate the entire three-dimensional in situ stress state, which can be necessary in certain cases. Methods based on displacement or strain

measurements, such as overcoring, enable more accurate estimations. As the in situ stress state is derived from displacement or strain values, the constitutive behavior of the rock must be known. Typically, the rock is assumed to be linearly elastic. It is worth noting that there are methods that take the time dependence of the material behaviour into consideration, e.g., the Anelastic Strain Recovery (ASR) method [5, 6]. However, here, we work with the assumption of linear elasticity, as the unloading rate is assumed to be sufficiently low.

In the present paper we investigate two specific overcoring methods: the In situ Stress Testing (IST) method developed by Sibra, and the Hollow Inclusion (HI) cell developed by the Commonwealth Scientific and Industrial Research Organisation (CSIRO). Both methods use several assumptions in order to make calculations feasible, and best practice recommendations are given in order to confirm that the measurement circumstances conform to these assumptions and consequently the measurement results are accurate to some extent. Our goal is to independently verify such assumptions and recommendations and potentially improve them in order to ensure accurate measurement results.

The outline of the paper is as follows. First, we give an overview of overcoring methods in Section 2. This is followed by the exposition of the theory behind the IST and CSIRO HI measurement methods in Section 3, which is crucial for understanding the assumptions made during the evaluation of such measurements as well as for clearly showing the limitations of these methods. In Section 4, we construct a series of finite element models for the quasi-static simulation of a case study in the overcoring measurement process for the IST and CSIRO HI methods. We evaluate the results of these case studies regarding the theoretically achievable maximum accuracy of the estimated in situ stress state. Finally, in Section 5, we compare and contrast the two measurement techniques and give recommendations regarding the placement of the specific overcoring measurement instruments inside the pilot hole.

2. A CONCISE OVERVIEW OF OVERCORING METHODS

One of the most common in situ stress measurement techniques in the mining industry is overcoring, which has been used since the 1960s [4]. The in situ stress state can be estimated based on the deformations and strains measured while the core is relieved. Naturally, the constitutive equations are necessary for the calculation of the stress state, therefore the material properties of the rock have to be measured. This is usually performed after the overcoring measurement itself, in a laboratory setting.

An overcoring measurement consists of three main steps, which are shown in Figure 1.

- *Step 1*: Drilling to the depth of the in situ stress state measurement itself. This main hole is usually called the borehole.
- *Step 2*: From the bottom of the borehole, a smaller diameter hole, the *pilot hole*, is drilled. An instrument, or gauge, is mounted in the pilot hole, which measures the deformations and strains of the pilot hole. (The specifics of this instrument depend on the measurement method used.)

- *Step 3:* A concentric hole is drilled around the instrument in the pilot hole, i.e. it is cored over. The outer diameter of this hole is identical or similar to the borehole diameter, and the inner diameter is larger than the pilot hole diameter. During this step, the remaining rock core is largely relieved from the in situ stress state, while the instrument installed in the pilot hole measures and records the deformations or strains throughout the process.

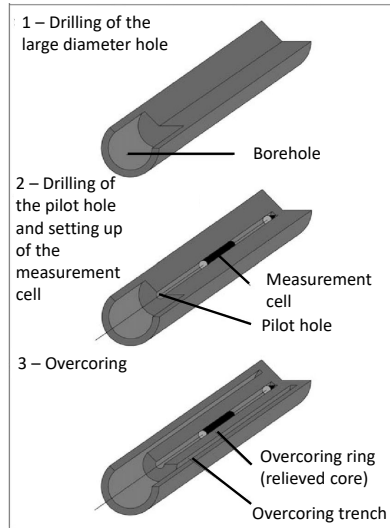


Figure 1. Steps of overcoring [7]

There are two main types of measurement tools that can be installed in the pilot hole. One of these measures the changes in diameter of the pilot hole during Step 3 by pins placed at different depths and orientations. The USBM (US Bureau of Mines) developed a gauge which measures the diameter change in three different orientations [8]. This provides enough data to estimate the in situ stress state in the plane perpendicular to the borehole axis with acceptable accuracy. Naturally, additional measurement data decreases the amount of total measurement error and the probability of instrument failure, therefore there are gauges that measure the pilot hole diameter during overcoring at multiple depths and orientations. For example, the IST gauge developed by SIGRA measures the diameter change in six different orientations [9]. The advantage of these instruments is that they can be used more than once, and there is no need for any cables during the measurements. The disadvantage of these gauges is that the in situ stress components parallel to the borehole axis cannot be estimated if the data is collected from a single hole [10]. Besides, this method is suitable only for relatively shallow depths. [2]

The other main type of overcoring instruments measures the strains of the pilot hole surface in different directions during Step 3. For example, the Hollow Inclusion

(HI) cell developed by CSIRO (Commonwealth Scientific and Industrial Research Organization) contains 9 or 12 strain gauges installed in different positions and orientations [11]. The advantage of these tools is that the full, three-dimensional in situ stress state can be estimated based on the data collected from a single hole. However, the CSIRO HI cell is glued into the pilot hole, so the cell can only be used once. A further disadvantage is that the epoxy-based glues cannot be applied in humid and dusty environments, and the thickness of the glue may influence the accuracy of the measurement [2].

A significant limitation of the overcoring technique is that the material properties of the rock must be known, since the in situ stress state is derived from deformation or strain values. Young's modulus and Poisson's ratio – and other parameters in case of anisotropic or nonlinear material behaviour – are usually determined by biaxial compression tests. These tests are usually carried out on the rock core remaining after Step 3 in the case of the CSIRO HI cell, and on nearby rock cores in the case of the IST method.

In the following section, the equations required to estimate the in situ stress state from the data collected by either an IST gauge or a CSIRO HI cell are presented.

3. THEORETICAL BACKGROUND OF THE EVALUATION OF OVERCORING MEASUREMENTS

3.1. Evaluation of IST measurements. The IST gauge measures the change in diameter of the pilot hole during the relief of the rock core. The collected data can be used to determine the original in situ stress state, which still occurs sufficiently far (1.5–2.5 times the diameter of the borehole [11]) from the borehole.

3.1.1. Assumptions. In order to derive the in situ stress state from the changes in diameter of the pilot hole, the following assumptions are made:

- the stress state is identical in any plane perpendicular to the axis of the borehole,
- the drilling of the borehole and the pilot hole have no influence on the original in situ stress state,
- after overcoring, the rock core and the surface of the pilot hole are completely relieved from any stress,
- the rock is considered to be linearly elastic, homogeneous and isotropic,
- the axial in situ stress component is known. If the axis of the borehole is vertical, this component corresponds with the lithostatic (also called overburden) pressure, which is caused by the weight of the overlying material [4].

These assumptions imply that the deformations measured by the IST gauge are caused by the relief of the in situ stress state. As a consequence, a relationship must exist between the changes in diameter and the in situ stress state.

3.1.2. Description of the stress state. For describing the various stress states considered, the Cauchy stress tensor σ is used, which is assumed to be symmetric. We

define a Cartesian coordinate system in which axis z coincides with the borehole axis. The components of this tensor are

$$\boldsymbol{\sigma} = \begin{bmatrix} \sigma_x & \tau_{xy} & \tau_{xz} \\ \tau_{xy} & \sigma_y & \tau_{yz} \\ \tau_{xz} & \tau_{yz} & \sigma_z \end{bmatrix}. \quad (3.1)$$

Accordingly, the change in the stress state near the pilot hole during Step 3 of overcoring is described by the (symmetric) tensor $\Delta\boldsymbol{\sigma}$ expressed as

$$\Delta\boldsymbol{\sigma} = \begin{bmatrix} \Delta\sigma_x & \Delta\tau_{xy} & \Delta\tau_{xz} \\ \Delta\tau_{xy} & \Delta\sigma_y & \Delta\tau_{yz} \\ \Delta\tau_{xz} & \Delta\tau_{yz} & \Delta\sigma_z \end{bmatrix}. \quad (3.2)$$

According to Section 3.1.1, the rock core is completely relieved after the overcoring, hence its loading changes:

$$\Delta\boldsymbol{\sigma} = \mathbf{0} - \boldsymbol{\sigma}^0, \quad (3.3)$$

where $\boldsymbol{\sigma}^0$ is the in situ stress state to be determined:

$$\boldsymbol{\sigma}^0 = \begin{bmatrix} \sigma_x^0 & \tau_{xy}^0 & \tau_{xz}^0 \\ \tau_{xy}^0 & \sigma_y^0 & \tau_{yz}^0 \\ \tau_{xz}^0 & \tau_{yz}^0 & \sigma_z^0 \end{bmatrix} = -\Delta\boldsymbol{\sigma}. \quad (3.4)$$

It is worth emphasizing here that these stress tensors describe the in situ stress state, which is the original, undisturbed stress state, and is different from the stress field close to the borehole. In most commonly used models, the in situ stress state is considered to be applied sufficiently far away from the borehole as a far-field boundary condition.

3.1.3. Connection between stress state and deformations. The change in diameter of the pilot hole Δd associated with the change in the loading of the core during the relief is given by [10]:

$$\begin{aligned} \Delta d = \frac{d}{E} [& (\Delta\sigma_x + \Delta\sigma_y) + 2(\Delta\sigma_x - \Delta\sigma_y)(1 - \nu^2) \cos(2\theta) + \\ & + 4\Delta\tau_{xy}(1 - \nu^2) \sin(2\theta) - \nu\Delta\sigma_z], \end{aligned} \quad (3.5)$$

where d is the diameter of the pilot hole, E and ν are the Young's modulus and the Poisson's ratio of the rock, θ is the angle formed by the measured diameter and the x axis of the coordinate system. Note that this formula does not contain the τ_{xz} and τ_{yz} shear stress components, as the determination of these components would require measurements from boreholes with different orientations.

The IST gauge measures the changes in diameter in six different orientations (and depths) [9]. Using equations (3.4) and (3.5), the following can be written:

$$\begin{aligned} \Delta d_i = -\frac{d}{E} [& (\sigma_x^0 + \sigma_y^0) + 2(\sigma_x^0 - \sigma_y^0)(1 - \nu^2) \cos(2\theta_i) + \\ & + 4\tau_{xy}^0(1 - \nu^2) \sin(2\theta_i) - \nu\sigma_z^0], \quad i = 1, 2, \dots, 6. \end{aligned} \quad (3.6)$$

This is a system of six linear equations. The variables are σ_x^0 , σ_y^0 , σ_z^0 and τ_{xy}^0 , the components describing the in situ stress state. The system can be written in a matrix equation form as

$$\begin{pmatrix} \Delta d_1 \\ \vdots \\ \Delta d_6 \end{pmatrix} = \hat{\mathbf{A}} \begin{pmatrix} \sigma_x^0 \\ \sigma_y^0 \\ \sigma_z^0 \\ \tau_{xy}^0 \end{pmatrix}, \quad (3.7)$$

where:

$$\hat{\mathbf{A}} = -\frac{d}{E} \begin{pmatrix} 1 + 2(1 - \nu^2) \cos(2\theta_1) & 1 - 2(1 - \nu^2) \cos(2\theta_1) & -\nu & 4(1 - \nu^2) \sin(2\theta_1) \\ \vdots & \vdots & \vdots & \vdots \\ 1 + 2(1 - \nu^2) \cos(2\theta_6) & 1 - 2(1 - \nu^2) \cos(2\theta_6) & -\nu & 4(1 - \nu^2) \sin(2\theta_6) \end{pmatrix}. \quad (3.8)$$

Although the above system seems to be overdetermined at first glance, the equations are actually linearly dependent: it can be shown in a straightforward way that – assuming distinct θ_i – the rank of matrix $\hat{\mathbf{A}}$ is 3, i.e. it does not have full rank.

3.1.4. *Solution of the system.* In order to solve the (3.7) system of equations, σ_z^0 must be known to circumvent the linear dependence of the original equations. According to Subsection 3.1.1, we assume that it is entirely determined by the overburden pressure, which can be expressed as

$$\sigma_z^0 = -\rho gh, \quad (3.9)$$

where ρ is the mean density of the rocks above the location of the measurement, g is the gravitational acceleration, h is the depth measured from the surface.

Consequently, the system of equations (3.7) becomes

$$\underbrace{\begin{pmatrix} \Delta d_1 - \frac{d}{E} \nu \sigma_z^0 \\ \Delta d_2 - \frac{d}{E} \nu \sigma_z^0 \\ \Delta d_3 - \frac{d}{E} \nu \sigma_z^0 \\ \Delta d_4 - \frac{d}{E} \nu \sigma_z^0 \\ \Delta d_5 - \frac{d}{E} \nu \sigma_z^0 \\ \Delta d_6 - \frac{d}{E} \nu \sigma_z^0 \end{pmatrix}}_{\mathbf{b}} = \mathbf{A} \begin{pmatrix} \sigma_x^0 \\ \sigma_y^0 \\ \tau_{xy}^0 \end{pmatrix}, \quad (3.10)$$

where:

$$\mathbf{A} = -\frac{d}{E} \begin{pmatrix} 1 + 2(1 - \nu^2) \cos(2\theta_1) & 1 - 2(1 - \nu^2) \cos(2\theta_1) & 4(1 - \nu^2) \sin(2\theta_1) \\ 1 + 2(1 - \nu^2) \cos(2\theta_2) & 1 - 2(1 - \nu^2) \cos(2\theta_2) & 4(1 - \nu^2) \sin(2\theta_2) \\ 1 + 2(1 - \nu^2) \cos(2\theta_3) & 1 - 2(1 - \nu^2) \cos(2\theta_3) & 4(1 - \nu^2) \sin(2\theta_3) \\ 1 + 2(1 - \nu^2) \cos(2\theta_4) & 1 - 2(1 - \nu^2) \cos(2\theta_4) & 4(1 - \nu^2) \sin(2\theta_4) \\ 1 + 2(1 - \nu^2) \cos(2\theta_5) & 1 - 2(1 - \nu^2) \cos(2\theta_5) & 4(1 - \nu^2) \sin(2\theta_5) \\ 1 + 2(1 - \nu^2) \cos(2\theta_6) & 1 - 2(1 - \nu^2) \cos(2\theta_6) & 4(1 - \nu^2) \sin(2\theta_6) \end{pmatrix}. \quad (3.11)$$

Now the rank of matrix \mathbf{A} is maximal. However, the system is overdetermined since there are six equations and only three variables. Naturally, measuring the change in diameter in three different orientations would be sufficient to determine σ_x^0 , σ_y^0 , and τ_{xy}^0 (see [8]). The reason for measuring more than three Δd values is to minimize the overall error. The optimal least-squares solution can be expressed [12] as

$$\begin{pmatrix} \sigma_x^0 \\ \sigma_y^0 \\ \tau_{xy}^0 \end{pmatrix} = (\mathbf{A}^T \mathbf{A})^{-1} \mathbf{A}^T \mathbf{b}. \quad (3.12)$$

Every element of matrix \mathbf{A} and vector \mathbf{b} is known, therefore the in situ stress components perpendicular to the axis of the borehole – here: the horizontal components – can be determined. It must be emphasized that these results are just estimations of the real in situ stress state, as several assumptions have been made (see Subsection 3.1.1).

Based on the above, the in situ stress components (σ_x^0 , σ_y^0 and τ_{xy}^0) in the plane ($x - y$) perpendicular to the axis of the borehole can be estimated from the data collected from a single measurement. In order to calculate these estimations, besides the assumptions listed in Subsection 3.1.1, the following values have to be known:

- the change in diameter of the pilot hole (Δd) in at least three different orientations θ ,
- the material properties of the rock (ρ , E and ν , as defined previously).

Since the IST gauge measures only radial deformations, the in situ stress state can only be estimated in a plane perpendicular to the axis of the borehole. Furthermore, the axial in situ stress component must be known. In our model, the axis of the borehole is vertical, so it has been assumed that this axial component is the lithostatic pressure (see (3.9)).

It is worth noting that the determination of the axial in situ stress components based purely on measurements is possible using the IST method. However, it requires measurements made in boreholes with different orientations. This method is detailed in [10].

3.2. Evaluation of CSIRO HI cell measurements. Unlike the IST instrument, which measures displacements directly, the CSIRO HI cell contains strain gauges, measuring the strains on the surface of the pilot hole during the relief of the rock core. The collected data can subsequently be used to determine the original in situ stress state.

3.2.1. Assumptions. In order to derive the in situ stress state from the strains measured on the pilot hole surface, the following assumptions have been made according to [11]:

- the stress state is identical in any plane perpendicular to the axis of the borehole,
- the drilling of the borehole and the pilot hole have no influence on the original in situ stress state,
- after overcoring, the rock core and the surface of the pilot hole are completely relieved from any stress,
- the rock and the CSIRO HI cell is considered to be linearly elastic, homogeneous and isotropic,
- the viscoelastic behaviour of the epoxy resin bonding the cell to the rock is negligible,
- the Young's modulus of the rock and the diameter of the overcoring bit are sufficiently large to neglect the resistance of the HI cell to the deformation.

These are similar to the assumptions listed in Subsection 3.1.1. They imply that the strains measured by the gauges are caused by the relief of the in situ stress state, therefore a connection can be found between them. The stress state can be described in the way given in Subsection 3.1.2.

However, whilst an IST gauge does not provide enough data to determine the in situ stress components parallel to the axis of the borehole, a measurement carried out by a CSIRO HI cell can be used to estimate every component of the in situ stress tensor.

The CSIRO HI cells has variants, that contain either 9 or 12 strain gauges installed in different positions and orientations [11]. In the following, we consider a 12-gauge cell.

The angle θ specifies the position of the strain gauge along the perimeter of the pilot hole measured from the x axis. The angle β specifies the orientation of the strain gauge:

- 0° : axial strain (ε_z),
- 90° : tangential strain (ε_θ),
- 45° or 135° : diagonal strain ($\varepsilon_{\pm 45^\circ}$).

Note that whilst the IST gauge measures only radial deformations, the strain gauges in the CSIRO HI cell measure tangential, axial and diagonal strains: this enables each component of the in situ stress tensor to be determined from the measurements performed via the HI cell.

3.2.3. *Connection between stress state and strains.* The in situ stress state associated with the measured strains is given by the following relationships (derived in [11]) as

$$E_r \varepsilon_\theta = -(\sigma_x^0 + \sigma_y^0) K_1 + 2(1 - \nu_r^2) [(\sigma_x^0 - \sigma_y^0) \cos(2\theta) + 2\tau_{xy}^0 \sin(2\theta)] K_2 + \nu_r K_4 \sigma_z^0, \quad (3.13)$$

$$E_r \varepsilon_z = -\sigma_z^0 + \nu_r(\sigma_x^0 + \sigma_y^0), \quad (3.14)$$

$$E_r \gamma_{\theta z} = -4(1 + \nu_r)(\tau_{yz}^0 \cos 2\theta - \tau_{xz}^0 \sin 2\theta) K_3, \quad (3.15)$$

$$\varepsilon_{\pm 45^\circ} = \frac{1}{2}(\varepsilon_z + \varepsilon_\theta \pm \gamma_{\theta z}). \quad (3.16)$$

Variables and parameters contained in these equations:

- E_r and ν_r are the Young's modulus and Poisson's ratio of the rock
- ε_θ , ε_z , and $\varepsilon_{\pm 45^\circ}$ are the tangential, axial and diagonal strains measured by the strain gauges,
- θ is the angle describing the strain gauge position,
- σ_x^0 , σ_y^0 , σ_z^0 , τ_{xy}^0 , τ_{xz}^0 , τ_{yz}^0 are the elements of the in situ stress tensor (see (3.4))
- $\gamma_{\theta z}$ is the engineering shear strain, which can be calculated according to (3.16),
- K_1 , K_2 , K_3 , K_4 are correction factors, detailed below.

The correction factors are necessary as the strain gauges are located in the stress sensor pipe instead of the pilot hole surface, and the material properties of the CSIRO HI cell are not identical to the material properties of the rock [11]. It is worth emphasizing that the behaviour of the HI cell is considered to be linearly elastic. In certain cases (e.g. high temperature), this assumption is not acceptable since the viscoelastic behaviour of the HI cell must be taken into consideration.

In order to calculate the correction factors, the following values must be known:

- E_p , the Young's modulus of the cell,
- ν_p , the Poisson's ratio of the cell,
- R_p , the radius of the pilot hole,
- R_{sg} , the distance between the strain gauges and the borehole axis,
- R_1 , the inner radius of the stress sensor pipe.

For the detailed calculation of the correction factors, see [11].

3.2.4. *Determination of the stress components perpendicular to the borehole axis.* Expressing σ_z from (3.14), then substituting it into (3.13) results in the expression

$$E_r(\varepsilon_\theta + \nu_r \varepsilon_z K_4) = -(\sigma_x^0 + \sigma_y^0)K_1 + 2(1 - \nu_r^2) [(\sigma_x^0 - \sigma_y^0) \cos(2\theta) + 2\tau_{xy}^0 \sin(2\theta)] K_2 + \nu_r^2(\sigma_x^0 + \sigma_y^0)K_4. \quad (3.17)$$

Then, equation (3.17) can be used to derive equations for the measurement results given by the strain gauges as

$$E_r(\varepsilon_{\theta;A_{90}} + \nu_r \varepsilon_{z;A_0} K_4) = -(\sigma_x^0 + \sigma_y^0)K_1 + 2(1 - \nu_r^2) [(\sigma_x^0 - \sigma_y^0) \cos(2\theta_{A_{90}}) + 2\tau_{xy}^0 \sin(2\theta_{A_{90}})] K_2 + \nu_r^2(\sigma_x^0 + \sigma_y^0)K_4, \quad (3.18a)$$

$$E_r(\varepsilon_{\theta;B_{90}} + \nu_r \varepsilon_{z;B} K_4) = -(\sigma_x^0 + \sigma_y^0)K_1 + 2(1 - \nu_r^2) [(\sigma_x^0 - \sigma_y^0) \cos(2\theta_{B_{90}}) + 2\tau_{xy}^0 \sin(2\theta_{B_{90}})] K_2 + \nu_r^2(\sigma_x^0 + \sigma_y^0)K_4, \quad (3.18b)$$

$$E_r(\varepsilon_{\theta;C_{90}} + \nu_r \varepsilon_{z;C_0} K_4) = -(\sigma_x^0 + \sigma_y^0)K_1 + 2(1 - \nu_r^2) [(\sigma_x^0 - \sigma_y^0) \cos(2\theta_{C_{90}}) + 2\tau_{xy}^0 \sin(2\theta_{C_{90}})] K_2 + \nu_r^2(\sigma_x^0 + \sigma_y^0)K_4, \quad (3.18c)$$

$$E_r(\varepsilon_{\theta;E_{90}} + \nu_r \varepsilon_{z;B} K_4) = -(\sigma_x^0 + \sigma_y^0)K_1 + 2(1 - \nu_r^2) [(\sigma_x^0 - \sigma_y^0) \cos(2\theta_{E_{90}}) + 2\tau_{xy}^0 \sin(2\theta_{E_{90}})] K_2 + \nu_r^2(\sigma_x^0 + \sigma_y^0)K_4, \quad (3.18d)$$

$$E_r(\varepsilon_{\theta;F_{90}} + \nu_r \varepsilon_{z;C_0} K_4) = -(\sigma_x^0 + \sigma_y^0)K_1 + 2(1 - \nu_r^2) [(\sigma_x^0 - \sigma_y^0) \cos(2\theta_{F_{90}}) + 2\tau_{xy}^0 \sin(2\theta_{F_{90}})] K_2 + \nu_r^2(\sigma_x^0 + \sigma_y^0)K_4. \quad (3.18e)$$

The above is a system of linear equations, where σ_x^0 , σ_y^0 and τ_{xy}^0 are to be determined. It can be written in a matrix equation form as

$$E_r \underbrace{\begin{pmatrix} \varepsilon_{\theta;A_{90}} + \nu_r \varepsilon_{z;A_0} K_4 \\ \varepsilon_{\theta;B_{90}} + \nu_r \varepsilon_{z;B} K_4 \\ \varepsilon_{\theta;C_{90}} + \nu_r \varepsilon_{z;C_0} K_4 \\ \varepsilon_{\theta;E_{90}} + \nu_r \varepsilon_{z;B} K_4 \\ \varepsilon_{\theta;F_{90}} + \nu_r \varepsilon_{z;C_0} K_4 \end{pmatrix}}_{\mathbf{d}} = \underbrace{\begin{pmatrix} C_{11} & C_{12} & C_{13} \\ C_{21} & C_{22} & C_{23} \\ C_{31} & C_{32} & C_{33} \\ C_{41} & C_{42} & C_{43} \\ C_{51} & C_{52} & C_{53} \end{pmatrix}}_{\mathbf{C}} \begin{pmatrix} \sigma_x^0 \\ \sigma_y^0 \\ \tau_{xy}^0 \end{pmatrix}, \quad (3.19)$$

where $\varepsilon_{z;B}$ can be determined using (3.16):

$$\varepsilon_{z;B} = \frac{\varepsilon_{B_{45}} + \varepsilon_{B_{135}}}{2} - \varepsilon_{B_{90}}. \quad (3.20)$$

The elements of matrix \mathbf{C} are:

$$C_{11} = -K_1 + 2(1 - \nu_r^2) \cos(2\theta_{A_{90}}) K_2 + \nu_r^2 K_4, \quad (3.21a)$$

$$C_{12} = -K_1 - 2(1 - \nu_r^2) \cos(2\theta_{A_{90}}) K_2 + \nu_r^2 K_4, \quad (3.21b)$$

$$C_{13} = 4(1 - \nu_r^2) \sin(2\theta_{A_{90}}), \quad (3.21c)$$

$$C_{21} = -K_1 + 2(1 - \nu_r^2) \cos(2\theta_{B_{90}})K_2 + \nu_r^2 K_4, \quad (3.21d)$$

$$C_{22} = -K_1 - 2(1 - \nu_r^2) \cos(2\theta_{B_{90}})K_2 + \nu_r^2 K_4, \quad (3.21e)$$

$$C_{23} = 4(1 - \nu_r^2) \sin(2\theta_{B_{90}}), \quad (3.21f)$$

$$C_{31} = -K_1 + 2(1 - \nu_r^2) \cos(2\theta_{C_{90}})K_2 + \nu_r^2 K_4, \quad (3.21g)$$

$$C_{32} = -K_1 - 2(1 - \nu_r^2) \cos(2\theta_{C_{90}})K_2 + \nu_r^2 K_4, \quad (3.21h)$$

$$C_{33} = 4(1 - \nu_r^2) \sin(2\theta_{C_{90}}), \quad (3.21i)$$

$$C_{41} = -K_1 + 2(1 - \nu_r^2) \cos(2\theta_{E_{90}})K_2 + \nu_r^2 K_4, \quad (3.21j)$$

$$C_{42} = -K_1 - 2(1 - \nu_r^2) \cos(2\theta_{E_{90}})K_2 + \nu_r^2 K_4, \quad (3.21k)$$

$$C_{43} = 4(1 - \nu_r^2) \sin(2\theta_{E_{90}}), \quad (3.21l)$$

$$C_{51} = -K_1 + 2(1 - \nu_r^2) \cos(2\theta_{F_{90}})K_2 + \nu_r^2 K_4, \quad (3.21m)$$

$$C_{52} = -K_1 - 2(1 - \nu_r^2) \cos(2\theta_{F_{90}})K_2 + \nu_r^2 K_4, \quad (3.21n)$$

$$C_{53} = 4(1 - \nu_r^2) \sin(2\theta_{F_{90}}). \quad (3.21o)$$

The position of the strain gauges imply that the E_{90} and F_{90} tangential strains belong to the $\varepsilon_{z;B}$ and $\varepsilon_{z;C_0}$ axial strains.

The elements of matrix \mathbf{C} and vector \mathbf{d} are known. The system is overdetermined, thus the solution is carried out using the least-squares error method (similarly to the case of the IST method detailed in Subsection 3.1) as

$$\begin{pmatrix} \sigma_x^0 \\ \sigma_y^0 \\ \tau_{xy}^0 \end{pmatrix} = (\mathbf{C}^T \mathbf{C})^{-1} \mathbf{C}^T \mathbf{d}. \quad (3.22)$$

This gives an estimate of the in situ stress state perpendicular to the borehole axis.

3.2.5. Stress components parallel to the borehole axis. The axial normal stress component can be calculated according to (3.14) as

$$\sigma_z^0 = \nu_r(\sigma_x^0 + \sigma_y^0) - E_r \varepsilon_z. \quad (3.23)$$

If σ_x^0 and σ_y^0 are known, the above expression can be evaluated. Since there are several measurement values for ε_z , their arithmetic mean is used for the calculations.

The axial shear stresses can be determined using equations (3.15)–(3.16). A linear system of equations can be written for τ_{xz} and τ_{yz} as

$$E_r \gamma_{\theta z; A_{45}} = -4(1 + \nu_r)(\tau_{yz}^0 \cos 2\theta_{A_{45}} - \tau_{xz}^0 \sin 2\theta_{A_{45}})K_3, \quad (3.24a)$$

$$E_r \gamma_{\theta z; B_{45}} = -4(1 + \nu_r)(\tau_{yz}^0 \cos 2\theta_{B_{45}} - \tau_{xz}^0 \sin 2\theta_{B_{45}})K_3, \quad (3.24b)$$

$$E_r \gamma_{\theta z; B_{135}} = -4(1 + \nu_r)(\tau_{yz}^0 \cos 2\theta_{B_{135}} - \tau_{xz}^0 \sin 2\theta_{B_{135}})K_3, \quad (3.24c)$$

$$E_r \gamma_{\theta z; D_{135}} = -4(1 + \nu_r)(\tau_{yz}^0 \cos 2\theta_{D_{135}} - \tau_{xz}^0 \sin 2\theta_{D_{135}})K_3. \quad (3.24d)$$

Expressed in a matrix form as

$$E_r \underbrace{\begin{pmatrix} \gamma_{\theta z;A_{45}} \\ \gamma_{\theta z;B_{45}} \\ \gamma_{\theta z;B_{135}} \\ \gamma_{\theta z;D_{135}} \end{pmatrix}}_{\mathbf{f}} = -4K_3(1 + \nu_r) \underbrace{\begin{pmatrix} -\sin 2\theta_{A_{45}} & \cos 2\theta_{A_{45}} \\ -\sin 2\theta_{B_{45}} & \cos 2\theta_{B_{45}} \\ -\sin 2\theta_{B_{135}} & \cos 2\theta_{B_{135}} \\ -\sin 2\theta_{D_{135}} & \cos 2\theta_{D_{135}} \end{pmatrix}}_{\mathbf{E}} \begin{pmatrix} \tau_{xz}^0 \\ \tau_{yz}^0 \end{pmatrix}. \quad (3.25)$$

Engineering shear strains are calculated according to (3.16). The elements of matrix \mathbf{E} and vector \mathbf{f} are known. This equation system is also overdetermined, so the solution is carried out using the least-squares error method again as

$$\begin{bmatrix} \tau_{xz}^0 \\ \tau_{yz}^0 \end{bmatrix} = (\mathbf{E}^T \mathbf{E})^{-1} \mathbf{E}^T \mathbf{f}, \quad (3.26)$$

giving the remaining components of the in situ stress tensor.

As shown above, a measurement carried out by a CSIRO HI cell provides enough data from a single borehole to estimate every in situ stress component. To summarize, besides the assumptions mentioned in Subsection 3.2.1, this estimation requires the following data:

- tangential strain (ε_θ) values from at least 3 different θ positions ,
- axial strain (ε_z) value from at least one θ position (measuring at at more than one position provides more reliable results),
- engineering shear strain $\gamma_{\theta z}$ values from at least 2 different θ positions (these can be calculated according to (3.16)),
- material properties of the rock (ρ , E_r and ν_r),
- values required to calculate the correction factors (see Subsection 3.2.3 for details).

4. FINITE ELEMENT MODELS OF OVERCORING MEASUREMENTS

For determining the validity and shortcomings of the assumptions contained in the two measurement methods detailed above, we carry out finite element simulations of two respective models of overcoring measurement. In situ stress components – given as boundary conditions – and material properties are specified according to the results of a measurement carried out at the National Radioactive Waste Repository in Bataapáti, Hungary [14, 15]. Based on the deformation and strain results of the simulation, an estimation of the in situ stress state is calculated according to the formulas given in Sections 3.1–3.2. Then, we compare these estimations to the values specified initially as boundary conditions, in order to examine the accuracy of these techniques, and to determine the optimal location of the measuring instrument.

4.1. Finite element model of the IST measurement. The finite element analysis was carried out using ANSYS Mechanical. In accordance with the linear elastic material model assumed and the evaluation procedure of the IST method, we performed three static analyses, each representing one of the three steps of an overcoring

measurement. We modelled a sufficiently large domain of rock at a depth of 276 m, loaded by the in situ stress state. (The depth and the loads were chosen according to [14].) Due to the symmetry of the geometry and the loads, a quarter model was used. It should be noted that the use of an axisymmetric model is not suitable here, as the in-situ stress state is usually not hydrostatic [1]. This is modelled according to Section 4.1.3.

The evaluation of the results from the finite element model (FEM) was carried out as detailed in Section 3.1. The aim of the investigation was to ascertain whether it is possible to determine the in situ stress state from the data collected during an IST measurement and, if so, how accurately the in situ stress components can be estimated.

4.1.1. *Geometry.* The simulation domain is represented as a cuboid. The longest edges of this cuboid are parallel to z , representing the vertical direction. The height of the cuboid is 2400 mm, and the vertical edges are all 600 mm long. With these dimensions, the disturbance in the stress field caused by the borehole is negligible on the side faces of the cuboid. The boreholes are modelled as cylinders with vertical axes intersecting the horizontal faces at their centers. The hole diameters are the following:

- borehole: 96 mm,
- pilot hole: 25.5 mm,
- overcoring, inner diameter: 63 mm,
- overcoring, outer diameter: 96 mm.

In order to decrease the computational resources required for the computations a quarter model was made. The model was divided into different bodies at the hole bottoms, making structured mesh generation feasible. After slicing, one part was formed from the bodies, merging the nodes on the contacting faces.

IST Step 1

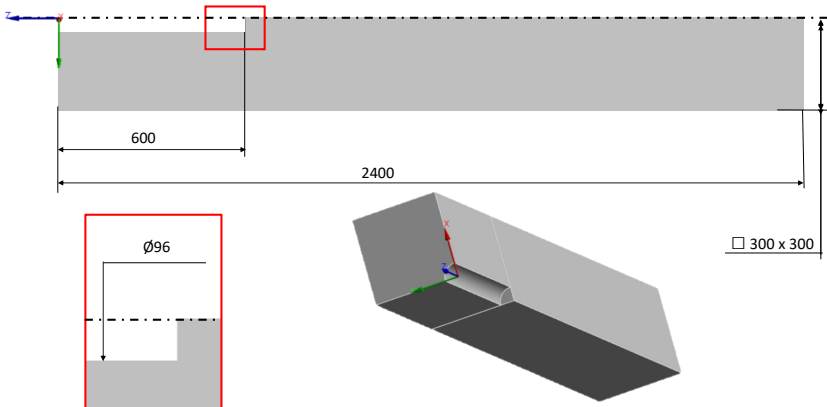


Figure 3. Applied geometry for modelling Step 1 of the IST measurement

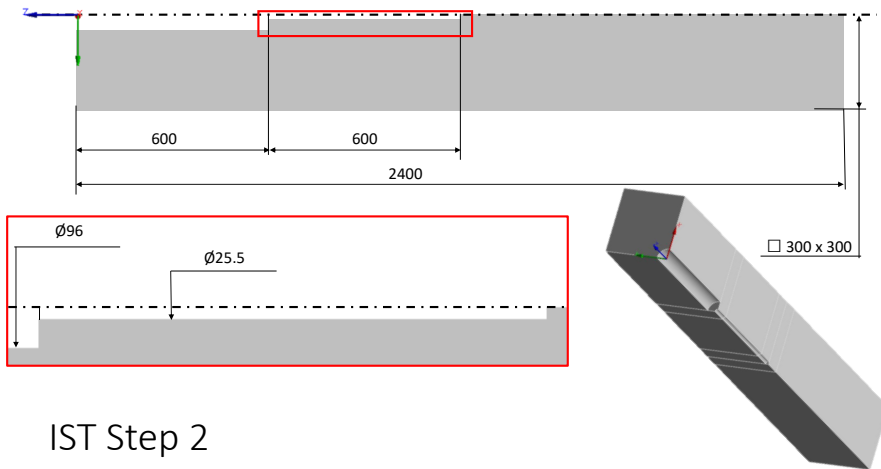


Figure 4. Applied geometry for modelling Step 2 of the IST measurement

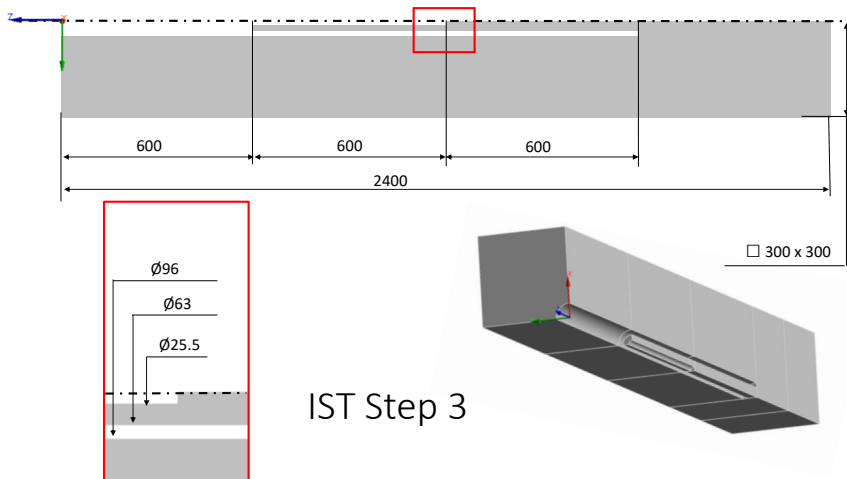


Figure 5. Applied geometry for modelling Step 3 of the IST measurement

The geometry applied for each step is presented in Figures 3–5. The origin of the global coordinate system is at the intersection of the borehole axis and the upper horizontal face.

4.1.2. *Finite element mesh.* The finite element mesh has been generated by ANSYS Mechanical. During the simulation of all three steps, identical principles were followed. Hexagonal elements were used to minimize the number of elements, and smaller elements were generated near the bottoms of the holes, as the deformation and stress

change abruptly at these locations. MultiZone meshing method was applied with element sizes being

- near the holes: 2–3 mm,
- far from the holes: 12–15 mm.

The applied meshes are presented in Figs. 6–8.

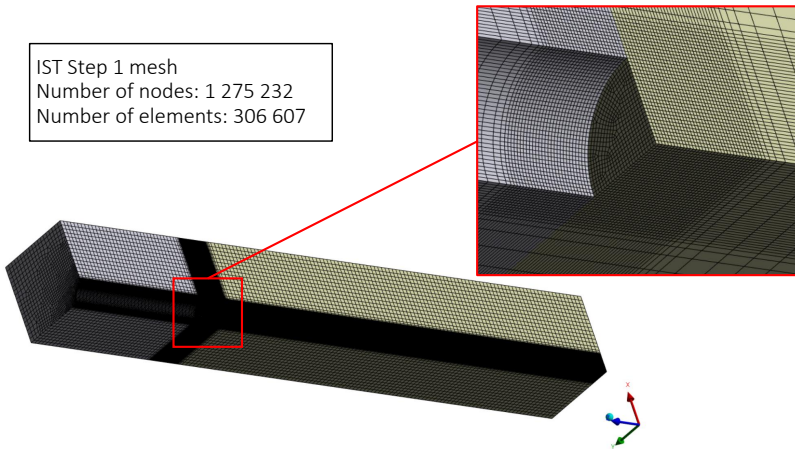


Figure 6. Applied finite element mesh for modelling Step 1 of the IST measurement

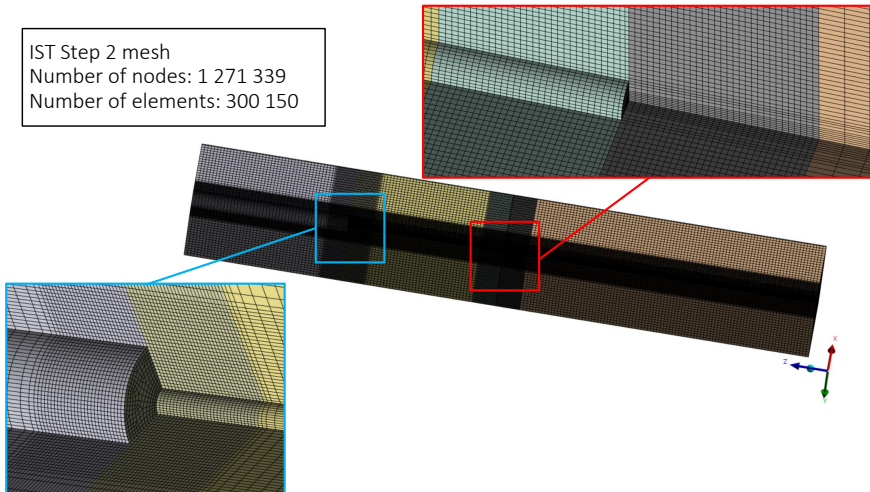


Figure 7. Applied finite element mesh for modelling Step 2 of the IST measurement

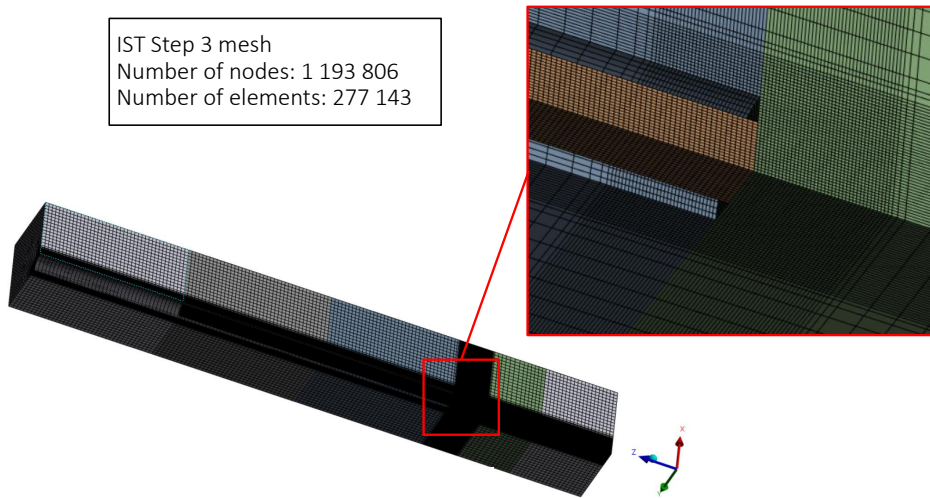


Figure 8. Applied finite element mesh for modelling Step 3 of the IST measurement

4.1.3. *Material properties and boundary conditions.* Material properties and boundary conditions are defined according to the results of the measurements carried out at the National Radioactive Waste Repository in Bataapáti, Hungary [14, 15]. The rock (porphyric monzogranite) is considered to be linearly elastic with the following properties:

- Young's modulus: 73.62 GPa,
- density: 2732 kg/m³,
- Poisson's ratio: 0.253.

The modelled domain is located at a depth of 276 m and loaded by the in situ stress state. At this point, the following assumptions are made:

- the modelled domain is large enough, so that the load of the outer surface of it is considered to be identical in every step,
- the vertical normal in situ stress component is the lithostatic pressure (see (3.9)).

Using the assumptions above, the load of the model can be given as three pressure boundary conditions acting on the outer surface of the modelled domain. The values of these during each step:

$$p_x = 8.21 \text{ MPa}, \quad (4.1)$$

$$p_y = 7 \text{ MPa}, \quad (4.2)$$

$$p_z = 7.5 \text{ MPa}. \quad (4.3)$$

Please note that the p_z value is larger than it should be according to (3.9). The reason behind this is the difference between the areas of the horizontal faces: the upper face

is smaller due to the presence of the borehole. The pressure p_z is applied on the upper face.

The constraints of the modelled domain are the following:

- symmetry is applied on the $x - z$ and $y - z$ planes: no node in these planes can move perpendicular to the plane,
- for every node in the lower horizontal face the displacement in z direction is set to be zero.

The applied boundary conditions are shown in Figure 9. It is worth noting that while formulating the finite element models, several methods of constraining the rigid body motion in z direction were tested. One of these was setting the z displacement of the faces loaded by pressure in the x and y directions to be zero. However, the results (especially for σ_z) implied that the best solution is constraining the lower horizontal face, as shown here.

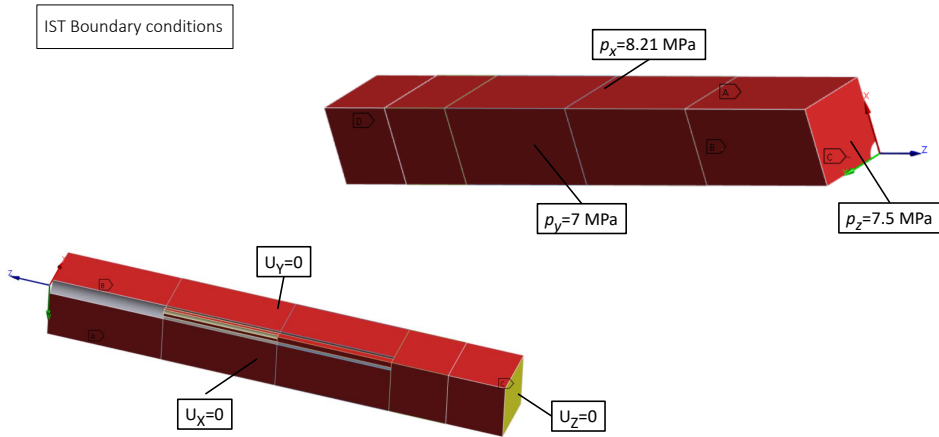


Figure 9. Boundary conditions applied during simulation of the IST measurement

4.1.4. *Evaluation.* As described in Section 3.1, the IST gauge measures the changes in diameter of the pilot hole during overcoring in six different orientations and depths. The aim of the evaluation performed here is to construct the in situ stress tensor from the virtual measurement data provided by the finite element results, as detailed in Section 3.1. Hence, the radial displacement of the points of the pilot hole surface has been queried in Steps 2 and 3. This simulates a measurement with ideal circumstances.

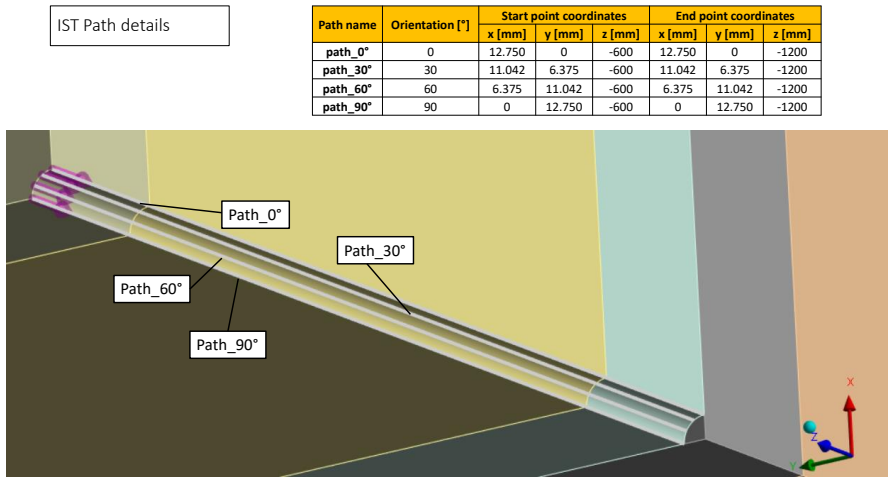


Figure 10. Paths defined to evaluate the simulation of the IST measurement. The paths are given with the global coordinates of the start and end points.

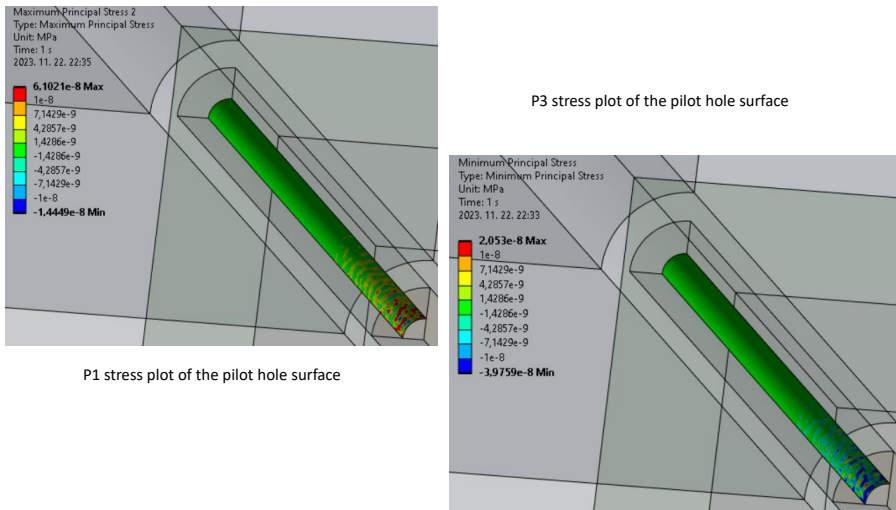


Figure 11. P1 and P3 stress results from Step 3 of the IST simulation. The minimal and maximal values imply that the pilot hole is relieved in this step.

Paths have been defined on the pilot hole surface along the full length of the hole in several orientations θ , as depicted in Figure 10. A real IST gauge measures the change of six diameters, forming a 30-degree angle. Since a quarter model is used,

only four of these are investigated, because the other two do not give any further results. Consequently, the paths are defined at orientations $\theta = 0^\circ$, $\theta = 30^\circ$, $\theta = 60^\circ$ and $\theta = 90^\circ$, where θ is the angle formed by the measured diameter and the x axis of the global coordinate system. The distance of the pins in the IST gauge is 10–15 mm [16], so the distance between the points where the radial displacements are queried is 12.5 mm.

This provides the radial displacement of the points on the pilot hole surface caused by the in situ stress state in each step. In Step 2, this stress state loads the pilot hole surface. However, in Step 3, the remaining rock core, which contains the pilot hole, is relieved from any stress. This is shown in Figure 11.

The diameter change of the pilot hole during the relief in any orientation can be calculated as (taking symmetry into account):

$$\Delta d = 2(U_{rad}^{[3]} - U_{rad}^{[2]}), \quad (4.4)$$

where $U_{rad}^{[2]}$ and $U_{rad}^{[3]}$ are the radial displacements of the pilot hole surface calculated from the FEM in Steps 2 and 3. Since the pilot hole is assumed to be relieved from any stress in Step 3,

$$U_{rad}^{[3]} = 0, \quad (4.5)$$

thus the change in diameter becomes

$$\Delta d = -2U_{rad}^{[2]}. \quad (4.6)$$

Based on (4.6), the changes in diameter along the paths presented in Figure 10 can be evaluated. These changes in diameter are shown in Figure 12.

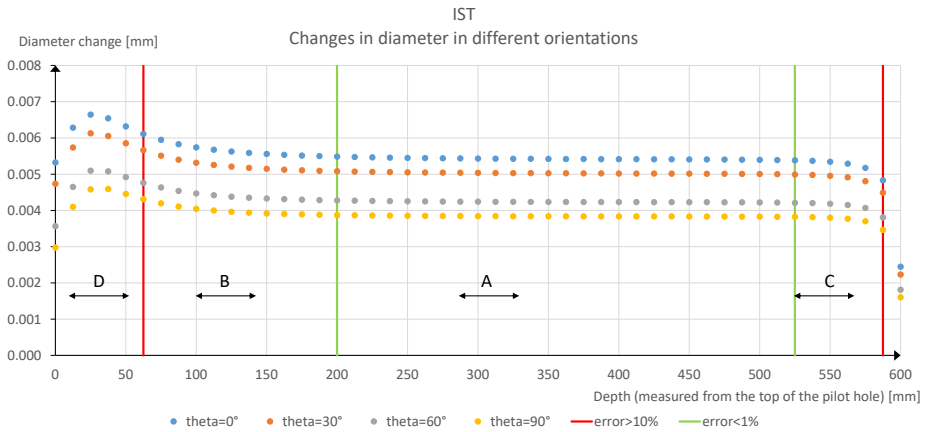


Figure 12. Diameter change Δd results of the IST simulation in each orientation. Red and green lines represent the error correlating to the Δd result from the middle of the pilot hole. The intervals labelled with letters are the locations of the simulated measurements.

The in situ stress state can be derived from the diameter changes according to equations (3.10)–(3.12). Due to the symmetry, the last two rows of matrix **A** and vector **b** are not considered. To solve these equations, the following values are needed:

- E and ν material properties (see Subsection 4.1.3),
- pilot hole diameter: $d = 25.5$ mm,
- vertical normal in situ stress component according to equation (3.9):
 $\sigma_z^0 = -7.5$ MPa,
- angles describing the different orientations: $\theta_1 = 0^\circ$, $\theta_2 = 30^\circ$, $\theta_3 = 60^\circ$,
 $\theta_4 = 90^\circ$,
- Δd diameter changes in each orientation.

The diameter changes depend on the depth measured from the top of the pilot hole, as presented in Figure 12. Firstly, let us substitute Δd values from location A (287–325 mm) into the equations. Doing so, a measurement carried out at such depth is simulated. This location is between the two green lines representing optimal instrument placement in Figure 12. The substituted values are presented in Table 2.

Table 2. Δd values substituted into equation (3.10), from location A (cf. Figure 12).

θ [°]	Depth [mm]	Δd [mm]
0	287.5	$5.437 \cdot 10^{-3}$
30	300	$5.037 \cdot 10^{-3}$
60	312.5	$4.240 \cdot 10^{-3}$
90	325	$3.842 \cdot 10^{-3}$

In situ stress components derived from the Δd values above, and their comparison against the loads set in the model are shown in Table 3. It can be seen that the error of the in situ stress components given by the solution of (3.10) is less than 1%. As a consequence, the estimation error is minimal if the data is collected from location A.

Table 3. Comparison of the in situ stress components derived from the data presented in Table 2., and the loads applied to the model detailed in Subsection 4.1.3.

Stress component	Estimation [MPa]	Load [MPa]	Error
σ_x^0	−8.261	−8.21	0.62%
σ_y^0	−7.031	−7.00	0.45%
τ_{xy}^0	0.001	0	–

Secondly, let us substitute Δd values from location B (100–137.5 mm) into the equations. This location is between the red and green lines shown in Figure 12, i.e., in the 10 % and 1% error range. The substituted values are presented in Table 4.

Table 4. Δd values substituted into equation (3.10), from location B (c.f. Figure 12)

θ [°]	Depth [mm]	Δd [mm]
0	100	$5.742 \cdot 10^{-3}$
30	112.5	$5.258 \cdot 10^{-3}$
60	125	$4.381 \cdot 10^{-3}$
90	137.5	$3.940 \cdot 10^{-3}$

In situ stress components derived from the Δd values above, and their comparison against the loads set in the model are shown in Table 5. It can be seen that the error of the in situ stress components given by the solution of (3.10) is around 5%.

Table 5. Comparison of the in situ stress components derived from the data presented in Table 4 and the loads applied to the model detailed in Subsection 4.1.3

Stress component	Estimation [MPa]	Load [MPa]	Error
σ_x^0	-8.628	-8.21	5.09%
σ_y^0	-7.246	-7.00	3.51%
τ_{xy}^0	0.019	0	-

Now, we substitute Δd values from location C (537.5–575 mm) into the equations. This location is between the green and red lines to the right in Figure 12. The substituted values are presented in Table 6.

Table 6. Δd values substituted into equation (3.10), from location C (c.f. Figure 12)

θ [°]	Depth [mm]	Δd [mm]
0	537.5	$5.369 \cdot 10^{-3}$
30	550	$4.958 \cdot 10^{-3}$
60	562.5	$4.153 \cdot 10^{-3}$
90	575	$3.701 \cdot 10^{-3}$

In situ stress components derived from the Δd values above, and their comparison against the loads set in the model are shown in Table 7. It can be seen that the error of the in situ stress components given by the solution of (3.10) is less than 5%.

The three cases illustrate that a good estimation can be given for the in situ stress components, if the Δd values are from a location between the two red lines shown in Figure 12.

Table 7. Comparison of the in situ stress components derived from the data presented in Table 6 and the loads applied to the model detailed in Subsection 4.1.3.

Stress component	Estimation [MPa]	Load [MPa]	Error
σ_x^0	-8.133	-8.21	0.94%
σ_y^0	-6.857	-7.00	2.04%
τ_{xy}^0	-0.018	0.00	-

However, if the estimation is based on Δd values collected outside this interval, the error is significant. The increased error is caused by the disturbed stress and displacement field near the bottom of the boreholes. As an example, we substitute Δd values from location D (12.5–50 mm) into the equations. This location is outside the interval marked by the two red lines according to Figure 12. The substituted values are presented in Table 8.

Table 8. Δd values substituted into equation (3.10), from location D (c.f. Figure 12).

θ [°]	Depth [mm]	Δd [mm]
0	12.5	$6.284 \cdot 10^{-3}$
30	25	$6.123 \cdot 10^{-3}$
60	37.5	$5.082 \cdot 10^{-3}$
90	50	$4.457 \cdot 10^{-3}$

In situ stress components derived from the Δd values above and their comparison against the loads set in the model are shown in Table 9. It can be seen that the error of the in situ stress components given by the solution of (3.10) exceeds 10%.

Table 9. Comparison of the in situ stress components derived from the data presented in Table 8 and the loads applied to the model written in Subsection 4.1.3

Stress component	Estimation [MPa]	Load [MPa]	Error
σ_x^0	-9.427	-8.21	14.82%
σ_y^0	-7.976	-7.00	13.94%
τ_{xy}^0	-0.209	0.00	-

4.1.5. *Summary of IST simulation results.* Based on the results of the finite element analysis, the in situ stress components can be estimated from the changes in diameter of the pilot hole as written in Section 3.1. Another conclusion is that the location of the IST gauge in the pilot hole has a significant influence on the results. The simulation shows that the ideal position of the IST gauge is between the two green lines in

Figure 12, which means a depth between 200–525 mm, measured from the top of the pilot hole. Nondimensionalizing the depths by the borehole diameter ($D = 96$ mm) produces the following results: in order to make the best approximation, the IST gauge should be located at least $2.1D$ beneath the bottom of the borehole, and at least $0.8D$ above the bottom of the pilot hole.

Locating a gauge outside the interval marked by the two red lines in Figure 12 increases the error. In terms of dimensionless values, this means the IST gauge must be located at least $0.7D$ beneath the bottom of the borehole, and $0.1D$ above the bottom of the pilot hole in order to get an acceptable estimation. This agrees with [8, p. 5], which suggests the following: “the plane of the deformation measurement should be located $1D$ ahead of the larger hole”. If this $1D$ distance is provided between the gauge and the top of the pilot hole, the error of the estimation is less than 10%. This location is marked with B in Figure 12. The in situ stress components in the horizontal $x - y$ plane can be estimated with an error less than 10% from the data collected at this location (see Table 5).

The same standard [8] suggests that when a distance of $1D$ cannot be left between the IST gauge and the top of the pilot hole, the gauge should be located as far ahead of the larger hole as possible. This also agrees with the simulation results: the distance to be left between the gauge and the bottom of the pilot hole ($0.1D$) is far less than the distance which has to be left between the top of the pilot hole and the gauge ($0.7D$).

Furthermore, the assumption made in Subsection 3.1.1 regarding the stress state of the pilot hole at the end of the overcoring is correct based on the results of the simulation (see Figure 11).

4.1.6. *Plausibility check.* In order to prove the results of the FE model plausible, the force equilibrium has been checked. The vector of the loading forces:

$$\mathbf{F}_t = \begin{bmatrix} p_x A_x \\ p_y A_y \\ p_z A_z \end{bmatrix} = \begin{bmatrix} -5 & 911 & 200 \\ -5 & 040 & 000 \\ -661 & 500 \end{bmatrix} \text{ N.} \quad (4.7)$$

In these equations, A_x , A_y and A_z are the surfaces on which the pressure boundary conditions were defined. The vector of the reaction forces computed from the FEM:

$$\mathbf{F}_r = \begin{bmatrix} 5 & 911 & 200 \\ 5 & 040 & 000 \\ 661 & 430 \end{bmatrix} \text{ N.} \quad (4.8)$$

The sum of the loading and the reaction forces:

$$\mathbf{F}_t + \mathbf{F}_r = \begin{bmatrix} 0 \\ 0 \\ -70 \end{bmatrix} \text{ N.} \quad (4.9)$$

This sum has to be zero. Since -70 N is negligible, it can be stated that the reaction forces and the defined loads are in equilibrium.

Besides the reaction forces, the stress field on the borehole surface has been checked. At points which can move along the x direction, σ_x has to be zero. Also at points

which can move along the y direction, σ_y has to be zero. As shown in Figure 13 the results of the FE model meet these two criteria.

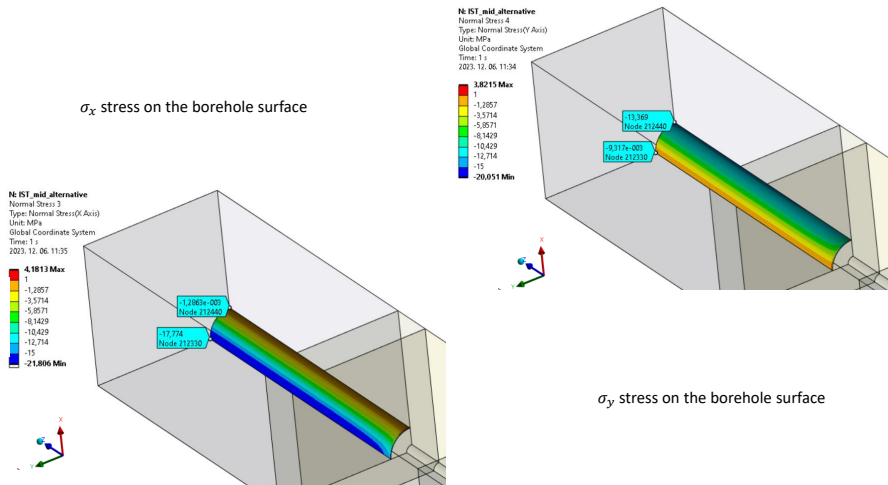


Figure 13. σ_x and σ_y stresses on the borehole surface in Step 2 of the IST simulation

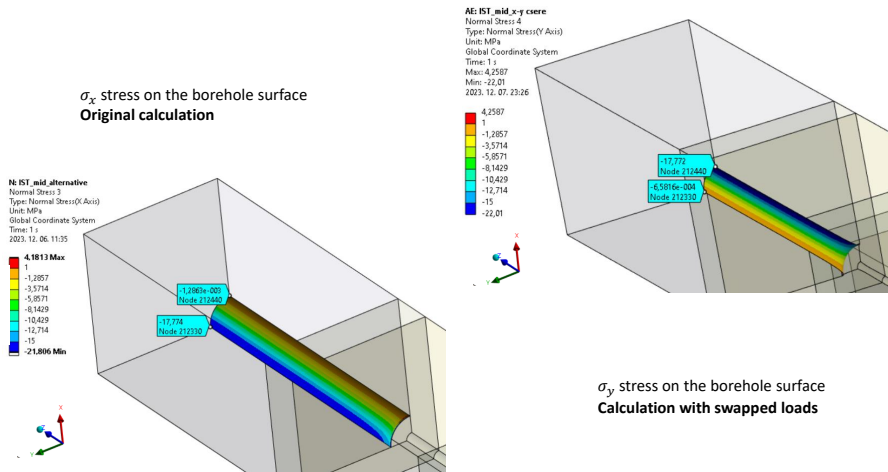


Figure 14. σ_x (left) results of the original simulation and σ_y (right) results of the simulation carried out with the commuted loads

Furthermore, an analysis with p_x and p_y values commuted was carried out and the stress state of the borehole surface was investigated. The commutation of the loads also commutes the x and y axes. This means the σ_x results of the original

computation must be the same as the σ_y results of this new simulation. Based on Figure 14, the results of the FE model meet this criterion. Naturally, the results must be mirrored to the plane defined by the z axis and the $x = y$ line.

The plausibility checks were carried out on the results of Step 2 of the IST simulation, since these results are used to derive the in situ stress state. Based on the performed plausibility checks, the results of the FE model are shown to be plausible.

4.2. Finite element model of the CSIRO HI measurement. For the CSIRO HI measurement method, the finite element analysis was carried out similarly to the previously described analysis. Three static analyses was performed using ANSYS Mechanical on a large domain of rock at a depth of 276 m and loaded by the in situ stress state, as detailed in Section 4.1. Due to the symmetry of the geometry and the loads, a quarter model can be used here as well. The evaluation of the simulation results was carried out as in Section 3.2. Similarly to the previous analysis, the goal was to determine whether it is possible to determine the in situ stress state from the data collected during a measurement carried out using a CSIRO HI cell, and if so, to determine how accurately the in situ stress components can be estimated.

4.2.1. Geometry. The geometric model is similar to that used for simulating the IST measurement. The differences from the model described in Subsection 4.1.1 are the diameters of the holes, which were specified according to [14] as

- borehole : 146 mm,
- pilot hole : 37.7 mm,
- overcoring, inner diameter: 131.4 mm,
- overcoring, outer diameter: 146 mm.

The applied geometry for each step is presented in Figs. 15–17.

4.2.2. Finite element mesh. The finite element mesh was generated similarly to the previous analysis, with a slightly different range of element sizes in the MultiZone meshing to accommodate for the different geometry. These element sizes were

- near the holes: 2.5–5 mm,
- far from the holes: 15–17 mm.

The applied meshes are presented in Figures 18–20.

4.2.3. Material properties and boundary conditions. The material properties and boundary conditions are the same as those given in Subsection 4.1.3. The applied boundary conditions are shown in Figure 21.

4.2.4. Evaluation. As described in Section 3.2, the strain gauges in the CSIRO HI cell measure the strains on the surface of the pilot hole during overcoring in 12 different orientations and positions. The aim is to construct the in situ stress tensor from the virtual measurement data provided by the finite element results as written in Section 3.2. Hence, the strains of the points of the pilot hole surface were queried in Steps 2 and 3. This simulates a measurement in ideal circumstances.

CSIRO Step 1

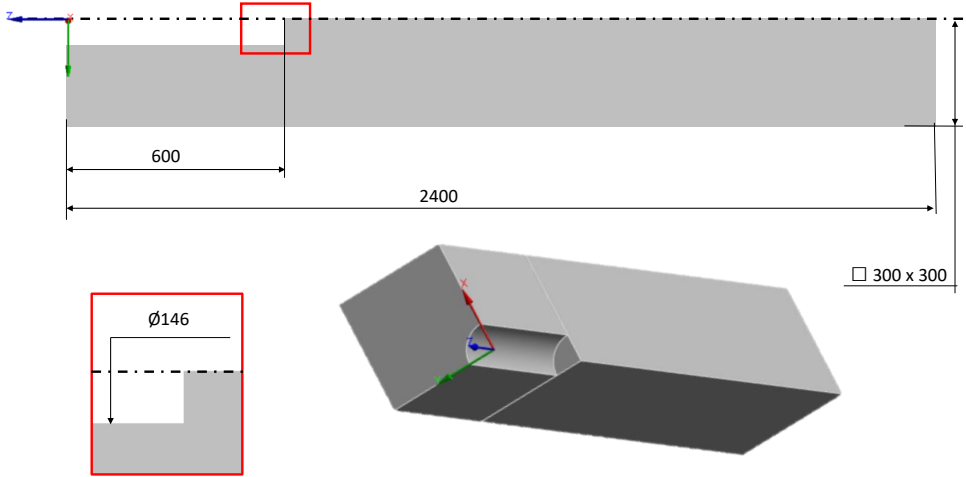


Figure 15. Applied geometry for modelling Step 1 of the CSIRO measurement

CSIRO Step 2

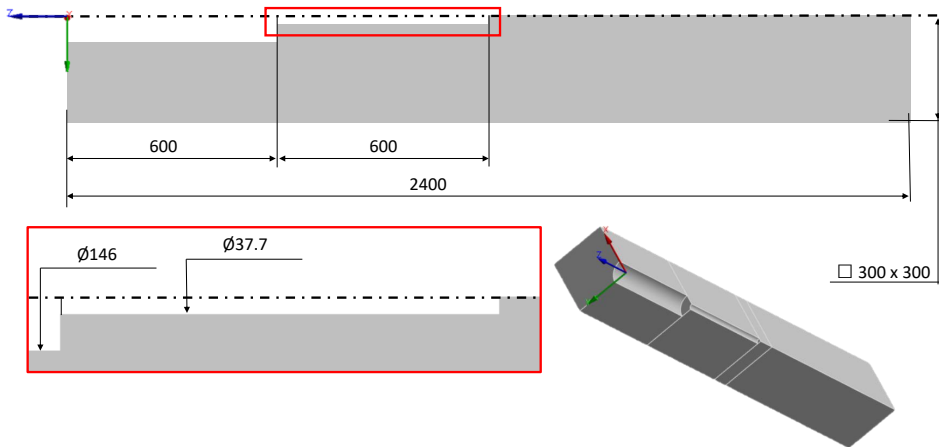


Figure 16. Applied geometry for modelling Step 2 of the CSIRO measurement

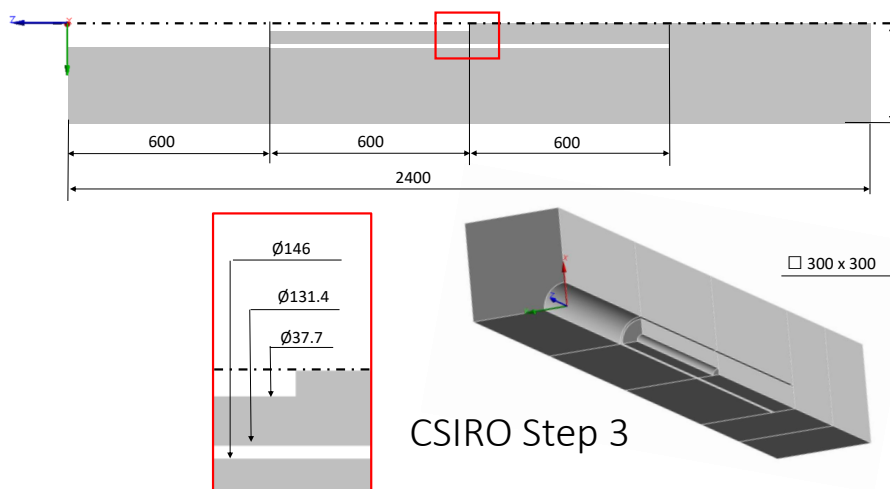


Figure 17. Applied geometry for modelling Step 3 the of CSIRO measurement

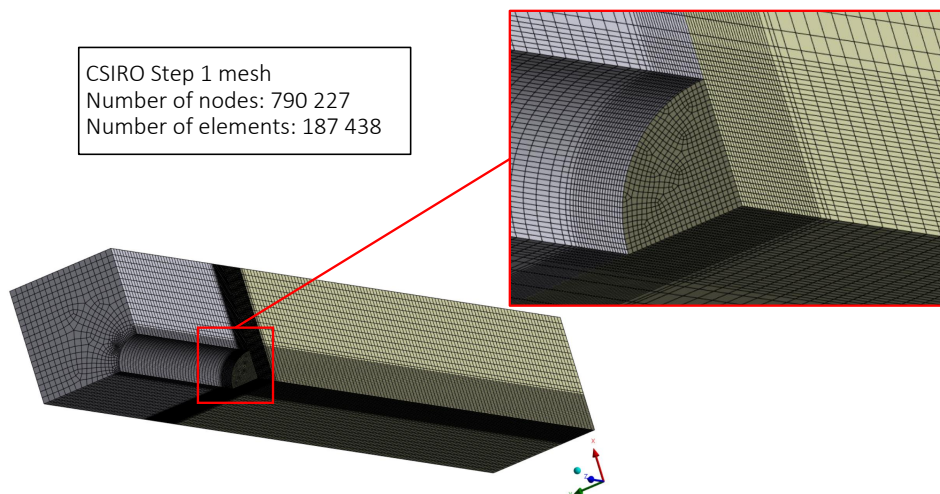


Figure 18. Applied finite element mesh for modelling Step 1 of the CSIRO measurement

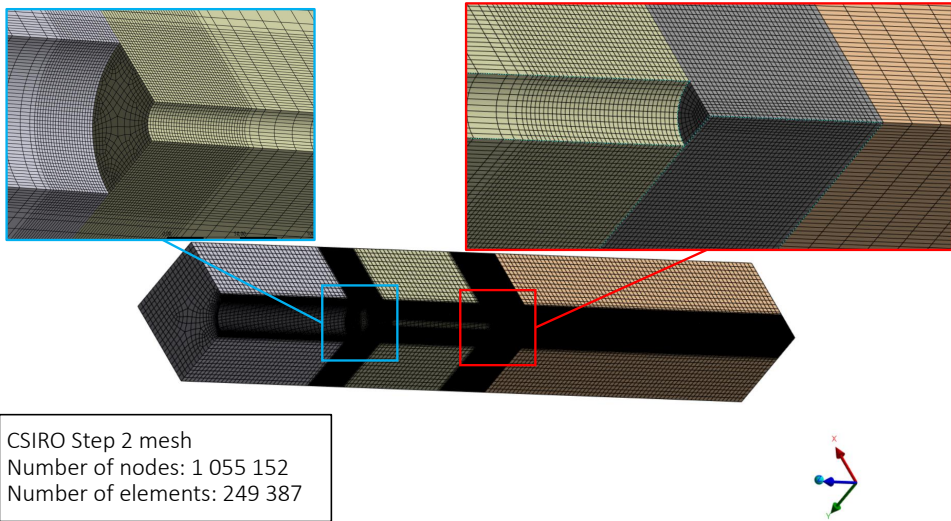


Figure 19. Applied finite element mesh for modelling Step 2 of the CSIRO measurement

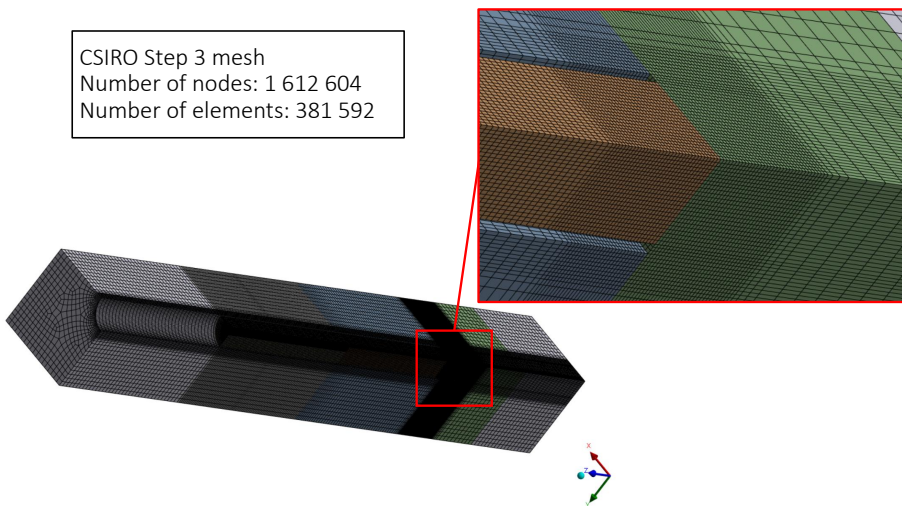


Figure 20. Applied finite element mesh for modelling Step 3 of the CSIRO measurement

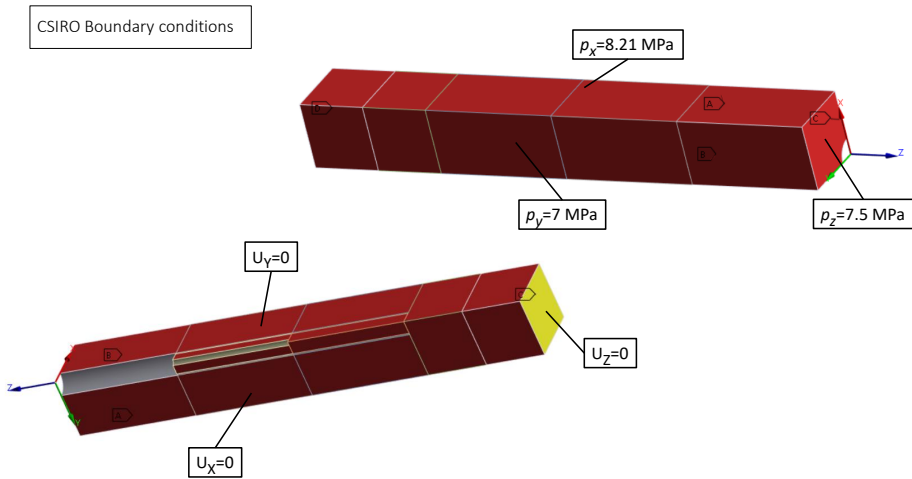


Figure 21. Boundary conditions applied for the simulation of the CSIRO measurement

The positions and orientations of the strain gauges are detailed in Table 1. Since a quarter model was used, the positions change to the values shown in Table 10. The orientation (β) of the strain gauges are not affected by the mirrorings. The following gauges measure the same strain in the quarter model:

- A₉₀ and C₉₀,
- A₄₅ and C₄₅.

The strains measured by these gauges are only considered once during the evaluation.

Table 10. Strain gauge positions in the quarter model [13]

ID	Original θ [°]	Modified θ [°]
A ₀	323	37
A ₉₀	300	60
A ₄₅	300	60
B ₄₅	163.5	16.5
B ₁₃₅	163.5	16.5
B ₉₀	180	0
C ₀	83	83
C ₉₀	60	60
C ₄₅	60	60
D ₁₃₅	300	60
E ₉₀	210	30
F ₉₀	90	90

Paths have been defined on the pilot hole surface along the full length of the hole in the modified positions θ as depicted in Figure 22. Along these paths, ε_θ , ε_z and $\gamma_{\theta z}$ are queried in Steps 2 and 3. The difference in these is the strain measured by the gauges during overcoring:

$$\Delta\varepsilon = \varepsilon^{[3]} - \varepsilon^{[2]}, \tag{4.10}$$

where ε tensor describes the strain state of a point of the pilot hole surface.

As mentioned earlier, by the end of the measurement (Step 3), the pilot hole surface is relieved from any stress, which means:

$$\varepsilon^{[3]} = \mathbf{0}, \tag{4.11}$$

hence strain caused by the relief from the in situ stress state:

$$\Delta\varepsilon = -\varepsilon^{[2]}. \tag{4.12}$$

The evaluation detailed in Section 3.2 was carried out with these results.

CSIRO Path details

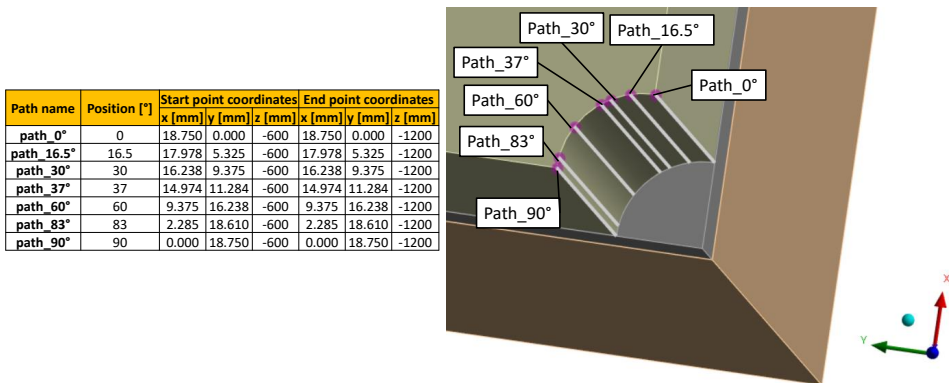


Figure 22. Paths defined to evaluate the simulation of the CSIRO measurement. The paths are given with the global coordinates of the start and end points.

As detailed in Section 4.1., the in situ stress components determined by an IST measurement depend on the location of the gauge in the pilot hole. The same dependence exists in case of the CSIRO HI cell. Tangential strain results are presented in Figure 23.

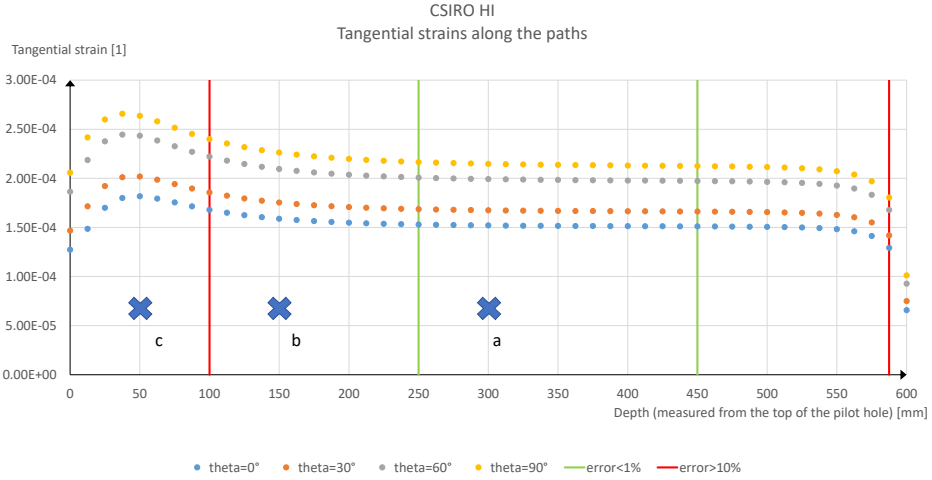


Figure 23. Tangential strain ε_θ results of the CSIRO simulation in each position. Red and green lines represent the error correlating to the ε_θ result from the middle of the pilot hole. The points marked with a cross are the locations of the simulated measurements.

Axial strain results are presented in Figure 24. In the modelled case, the ε_z axial strains are independent from the gauge position θ .

The in situ stress components in the horizontal ($x - y$) plane can be derived from the strains according to equations (3.19)–(3.22). Due to the symmetry, the 3rd row of matrix \mathbf{C} and vector \mathbf{d} are not considered. To solve these equations, the following values are needed:

- E_r and ν_r material properties (Subsection 4.2.3),
- positions and orientations of the strain gauges (Table 10),
- strain results of the simulation, queried at the locations of the strain gauges,
- K_1, K_2, K_4 correction factors. K_3 is only needed to calculate the shear stresses.

In Subsection 3.2.3 the role and calculation of the correction factors are detailed. Since the CSIRO HI cell itself is not modelled, its material properties are considered to be

- $E_p = 0$,
- $\nu_p = 0$.

In the finite element model, the measured strains are queried from the pilot hole surface, hence:

$$R_p = R_{sg} = R_1 = 18.85 \text{ mm} \quad (4.13)$$

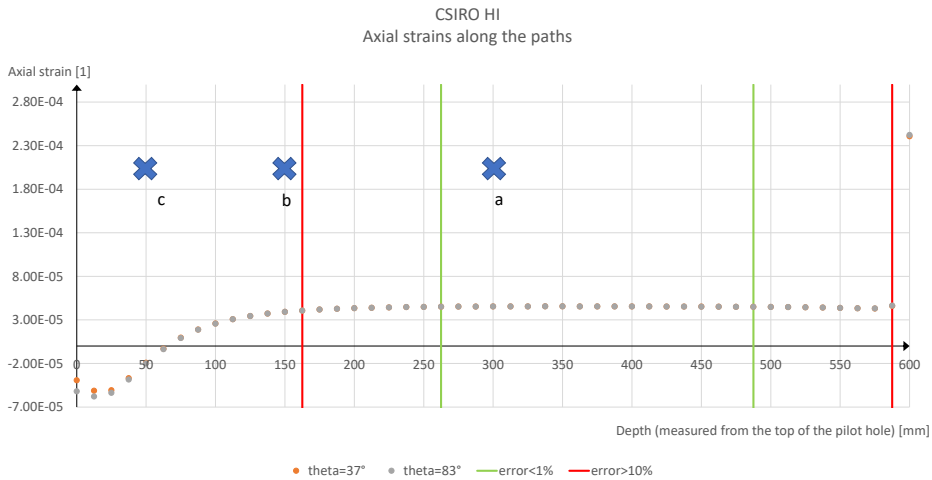


Figure 24. Axial strain ε_z results of the CSIRO simulation in each position. Red and green lines are representing the error correlating to the ε_z result from the middle of the pilot hole. The points marked with a cross are the locations of the simulated measurements.

are used for further calculations. With these input parameters, correction factors can be calculated according to [11]:

$$K_1 = K_2 = K_3 = K_4 = 1. \quad (4.14)$$

This means that the stiffness of the CSIRO HI cell has not been taken into consideration in the model. The fact that the strains are not measured on the pilot hole surface is also neglected.

Firstly, let us substitute strain values shown in Table 11 into equation (3.19), and solve it using (3.22).

Table 11. Tangential strain values from location ‘a’ (300 mm depth) to be substituted into (3.19). The axial strain at this depth is $\varepsilon_z = 4.54 \cdot 10^{-5}$.

θ [°]	Strain gauge	ε_θ [1]
0	B ₉₀	$1.521 \cdot 10^{-4}$
30	E ₉₀	$1.675 \cdot 10^{-4}$
60	A ₉₀	$1.993 \cdot 10^{-4}$
90	F ₉₀	$2.148 \cdot 10^{-4}$

With this evaluation the horizontal components of the in situ stress state can be estimated. These values are presented in Table 12.

Table 12. Comparison of the horizontal in situ stress components calculated from the values in Table 11 and the loads of the model detailed in Subsection 4.2.3

Stress component	Estimation [MPa]	Load [MPa]	Error
σ_x^0	-8.284	-8.21	0.90%
σ_y^0	-7.047	-7.00	0.68%
τ_{xy}^0	-0.001	0	-

The axial normal in situ stress component can be calculated according to (3.23):

$$\sigma_z^0 = \nu_r(\sigma_x^0 + \sigma_y^0) - E_r \varepsilon_z = -7.221 \text{ MPa.} \quad (4.15)$$

It can be seen that the error of the horizontal in situ stress components is less than 1%. As a consequence, the estimation error is minimal if the data is collected from location ‘a’. This location is in the interval bounded by the two green lines in Figures 23–24. In terms of σ_z^0 , the error value is higher: 3.72%.

The axial (vertical) shear stresses can be calculated according to equations (3.25)–(3.26). Engineering shear strain results can be queried directly from the FE model, therefore the modelling of the diagonal strain gauges is not required. Since the x , y , and z axes of the model coincide with the principal stress directions of the in situ stress state, only normal stress components have been given as boundary conditions. As a consequence, the *in situ* shear stress components derived from the measured strains on the pilot hole surface have to be zero. The queried $\gamma_{\theta z}$ values are negligible compared to the strain results, so the derived τ_{xz}^0 and τ_{yz}^0 are very close to zero.

Let us substitute strain values shown in Table 13 into equation (3.19), and solve it using (3.22). With this evaluation the horizontal components of the in situ stress

Table 13. Tangential strain values from location ‘b’ (150 mm depth) to be substituted into (3.19). The axial strain at this depth is $\varepsilon_z = 3.917 \cdot 10^{-5}$

θ [°]	Strain gauge	ε_θ [1]
0	B ₉₀	$1.589 \cdot 10^{-4}$
30	E ₉₀	$1.754 \cdot 10^{-4}$
60	A ₉₀	$2.263 \cdot 10^{-4}$
90	F ₉₀	$2.225 \cdot 10^{-4}$

state can be estimated. These values are presented in Table 14.

The axial normal in situ stress component can be calculated according to (3.23):

$$\sigma_z^0 = \nu_r(\sigma_x^0 + \sigma_y^0) - E_r \varepsilon_z = -6.913 \text{ MPa.} \quad (4.16)$$

Table 14. Comparison of the horizontal in situ stress components calculated from the values in Table 13 and the loads of the model detailed in Subsection 4.2.3

Stress component	Estimation [MPa]	Load [MPa]	Error
σ_x^0	-8.628	-8.21	5.09%
σ_y^0	-7.299	-7.00	4.29%
τ_{xy}^0	-0.002	0.00	-

It can be seen that the error of the horizontal in situ stress components is around 5%. As a consequence, the error of the estimation increases if the data is collected from location ‘b’. This location is in the interval bounded by a green and a red line in Figure 23. In terms of σ_z^0 , the error value is higher: 7.83%. Although location ‘b’ is outside the interval bounded by the two red lines in Figure 24 – so this is not an ideal location to measure axial strains – the estimation of the axial normal stress component is acceptable.

We substitute strain values shown in Table 15 into equation (3.19) and solve it using (3.22).

Table 15. Tangential strain values from location ‘c’ (50 mm depth) to be substituted into (3.19). The axial strain at this depth is $\varepsilon_z = -1.962 \cdot 10^{-5}$.

θ [°]	Strain gauge	ε_θ [1]
0	B ₉₀	$1.817 \cdot 10^{-4}$
30	E ₉₀	$2.019 \cdot 10^{-4}$
60	A ₉₀	$2.434 \cdot 10^{-4}$
90	F ₉₀	$2.638 \cdot 10^{-4}$

The horizontal components of the in situ stress state can be estimated. These values are presented in Table 16.

Table 16. Comparison of the horizontal in situ stress components calculated from the values in Table 15 and the loads of the model detailed in Subsection 4.2.3

Stress component	Estimation [MPa]	Load [MPa]	Error
σ_x^0	-9.374	-8.21	14.18%
σ_y^0	-7.756	-7.00	10.80%
τ_{xy}^0	-0.002	0	-

The axial normal in situ stress component can be calculated according to (3.23):

$$\sigma_z^0 = \nu_r(\sigma_x^0 + \sigma_y^0) - E_r\varepsilon_z = -2.889 \text{ MPa}. \tag{4.17}$$

It can be seen that the error of the horizontal in situ stress components is around 15%. In terms of σ_z^0 , the error value is even higher: 61.48%. As a consequence, the estimation is not acceptable if the data is collected from location ‘c’. This location is outside the interval bounded by the two red lines in Figure 23. Based on the results of the simulation, the in situ stress components should not be derived from the data collected by a measurement outside the interval marked with the red lines in Figure 23.

4.2.5. Summary of CSIRO HI simulation results. Based on the results of the finite element analysis, the in situ stress components can be estimated from the strains of the pilot hole surface during overcoring as given in Section 3.2. Another conclusion is that the location of the CSIRO HI cell in the pilot hole has a significant effect on the results. The simulation shows that the ideal position of the CSIRO HI cell is between the two green lines in Figure 23, which means a depth between 250–450 mm measured from the top of the pilot hole. Nondimensionalizing the depths by the borehole diameter ($D = 146$ mm) produces the following results: in order to make the best approximation, the CSIRO HI cell should be located $1.7D$ beneath the bottom of the borehole, and $1D$ above the bottom of the pilot hole. This agrees with [11], which suggests that the CSIRO HI cell should be located $1.5D - 2.5D$ beneath the bottom of the borehole.

Locating a gauge outside the interval marked by the two red lines in Figure 23 increases the error. In terms of dimensionless values, this means that the HI cell must be located at least $0.7D$ beneath the bottom of the borehole, and at least $0.1D$ above the bottom of the pilot hole in order to obtain an acceptable estimation.

In order to give an accurate estimation for the axial normal in situ stress component σ_z^0 , the CSIRO HI cell is recommended to be located in the interval bounded by the two green lines in Figure 24. In terms of depths, this means 262.5–487.5 mm. Nondimensionalizing the depths by the borehole diameter ($D = 146$ mm) produces the following results: in order to make the best approximation, the CSIRO HI cell should be located $1.8D$ beneath the bottom of the borehole, and $0.8D$ above the bottom of the pilot hole. If the axial strain values are measured outside the interval bounded by the two red lines in Figure 24, the estimation for σ_z^0 is less reliable. However, as has been demonstrated by the results of location ‘b’, the accuracy of the estimated in situ stress components depends on the tangential strains rather than on the axial strains.

Note that at every location of evaluation, the error of the estimated value of σ_z^0 is greater than the error of the horizontal in situ stress components. The reason for this is that the pressure boundary condition in z direction is applied on the upper horizontal face of the rock mass. This upper face is smaller than the lower face due to the presence of the borehole. The σ_z stress value caused by the reaction force on this lower face – which cannot move in direction z – is -7.153 MPa.

Furthermore, we can conclude that the assumption made in Subsection 3.2.1 regarding the stress state of the pilot hole at the end of the overcoring is correct based on the results of the simulation (see Figure 25).

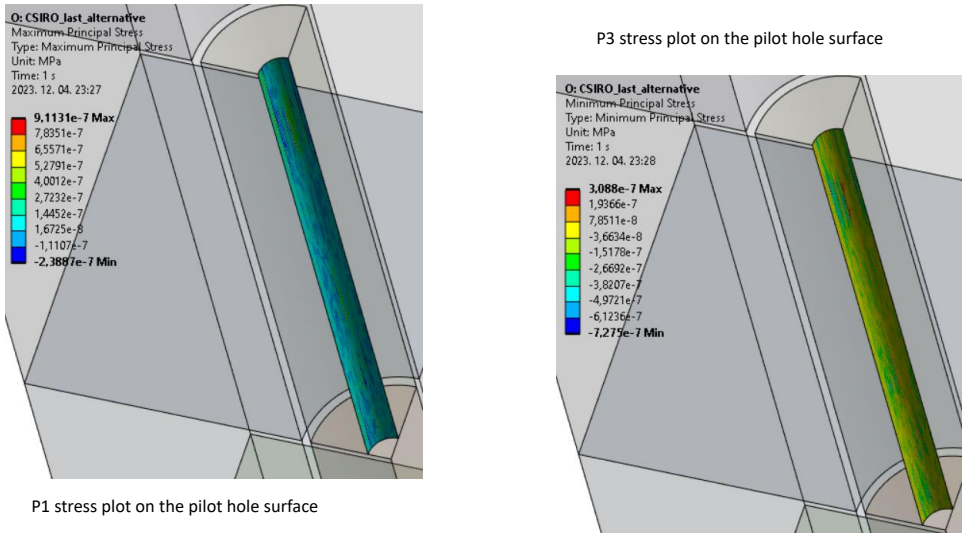


Figure 25. P1 and P3 stress results from Step 3 of the CSIRO simulation. The minimal and maximal values imply that the pilot hole is relieved in this step.

4.2.6. *Plausibility check.* In order to prove the results of the FE model plausible, the force equilibrium has been checked. The vector of the loading forces:

$$\mathbf{F}_t = \begin{bmatrix} p_x A_x \\ p_y A_y \\ p_z A_z \end{bmatrix} = \begin{bmatrix} -5 & 911 & 200 \\ -5 & 040 & 000 \\ -643 & 770 \end{bmatrix} \text{ N.} \quad (4.18)$$

In these equations, A_x , A_y and A_z are the surfaces on which the pressure boundary conditions were defined. The vector of the reaction forces computed from the FEM:

$$\mathbf{F}_r = \begin{bmatrix} 5 & 911 & 200 \\ 5 & 040 & 000 \\ 643 & 610 \end{bmatrix} \text{ N.} \quad (4.19)$$

The sum of the loading and the reaction forces:

$$\mathbf{F}_t + \mathbf{F}_r = \begin{bmatrix} 0 \\ 0 \\ -160 \end{bmatrix} \text{ N.} \quad (4.20)$$

This sum has to be zero. Since -160 N is negligible compared to the applied boundary conditions, it can be stated that the reaction forces and the defined loads are in equilibrium.

Besides the reaction forces, the stress field on the borehole surface was also checked. At points which can move along the x direction, σ_x has to be zero. Also at points

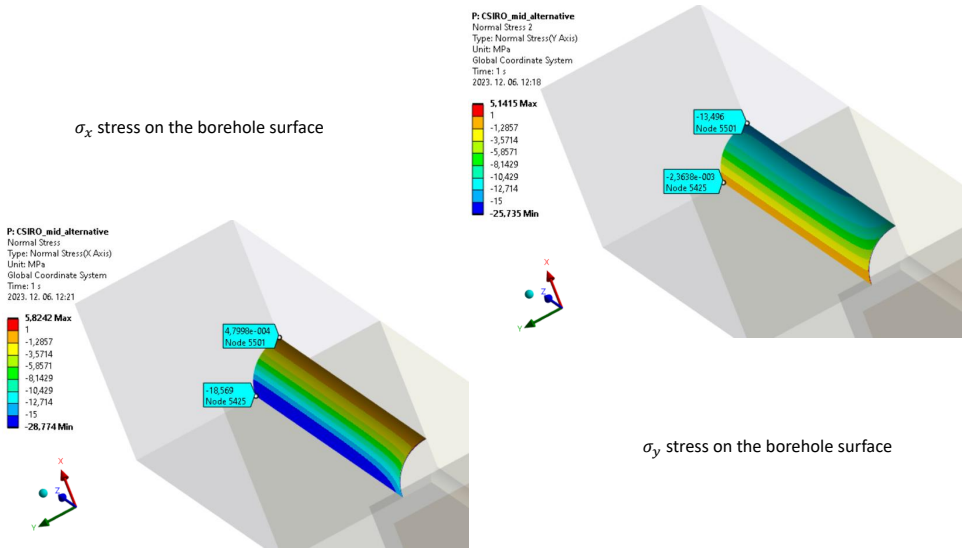


Figure 26. σ_x and σ_y stresses on the borehole surface in Step 2 of the CSIRO HI simulation.

which can move along the y direction, σ_y has to be zero. As shown in Figure 26, the results of the FE model meet these two criteria.

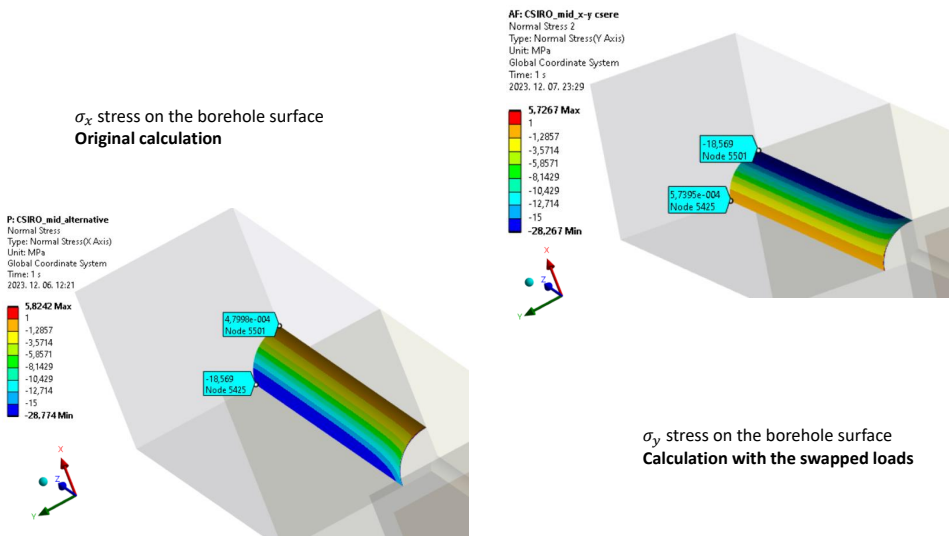


Figure 27. σ_x (left) results of the original simulation, and σ_y (right) results of the simulation carried out with the commuted loads

Furthermore, an analysis with p_x and p_y values commuted was carried out and the stress state of the borehole surface was investigated. The commutation of the loads also commutes the x and y axes. This means the σ_x results of the original computation must be the same as the σ_y results of this new simulation. Based on Figure 27, the results of the FE model meet this criterion. Naturally, the results must be mirrored to the plane defined by the z axis and the $x = y$ line.

The plausibility checks were performed based on the results of Step 2 of the CSIRO HI simulation, since these results are used to derive the in situ stress state. Based on the performed plausibility checks, the results of the FE model are deemed to be plausible.

5. COMPARISON OF THE IST AND CSIRO HI TECHNIQUES

In this section, the main conclusions of Section 4 have been collected.

Firstly, based on the results of the finite element analysis, both the IST gauge and CSIRO HI cell can provide enough data to give a correct estimation for the in situ stress state. The detailed evaluation process has been presented in Section 3. According to Table 3, the horizontal in situ stress components can be derived from the deformations measured by the IST gauge with an error less than 1%. According to Table 12, the horizontal in situ stress components can be derived from the strains measured by the CSIRO HI cell with an error of less than 1%. Compared to the IST gauge, the error of the estimation based on the data provided by the CSIRO HI cell is higher. However, the CSIRO HI cell provides enough data to estimate the axial in situ stress components as well. The error of this estimation is less than 5%. Meanwhile, the axial in situ stress components cannot be derived from the data collected by the IST gauge in a single borehole.

It must be emphasized that during the calculations, several assumptions have been made, for example:

- the the rock was considered to be linearly elastic, homogeneous and isotropic,
- the stress state was considered to be identical in any plane perpendicular to the axis of the borehole.

Besides the items mentioned above further assumptions have been made. These are detailed in Subsections 3.1.1 and 3.2.1. We must emphasize that the results of a real measurement can only be less accurate than when calculated by an idealized model, and the robustness of the presently investigated methods in the case of non-ideal circumstances should be assessed to supplement the analysis presented here.

Secondly, based on the results of the finite element analysis, the ideal position of the IST gauge and the CSIRO HI cell has been determined. In order to make the results comparable, the distances have been nondimensionalized by the borehole diameters. This value is $D = 96$ mm in terms of the IST gauge, and $D = 146$ mm in terms of the CSIRO HI cell. The ideal position of the tools is the following:

- the minimal distance between the top of the pilot hole and the IST gauge is $2.1D$,

- the minimal distance between the top of the pilot hole and the CSIRO HI cell is $1.7D$,
- the minimal distance between the bottom of the pilot hole and the IST gauge is $0.8D$,
- the minimal distance between the bottom of the pilot hole and the CSIRO HI cell is $1D$.

Comparing the dimensionless values, it can be stated that the CSIRO HI cell can be located closer to the top of the pilot hole than the IST gauge. However, the IST gauge can be located closer to the pilot hole bottom than the CSIRO HI cell. These optimal intervals are marked by green lines in Figures 28– 29.

To obtain acceptable estimations for the in situ stress components, both the IST gauge and the CSIRO HI cell should be set at least $0.7D$ beneath the top of the pilot hole, and $0.1D$ above the bottom of the pilot hole. This interval is marked by red lines in Figures 28– 29. Note that the optimal location of the CSIRO HI cell has been determined based on the tangential strain results, since the accuracy of the estimations depends more on the tangential strains than the axial strains.

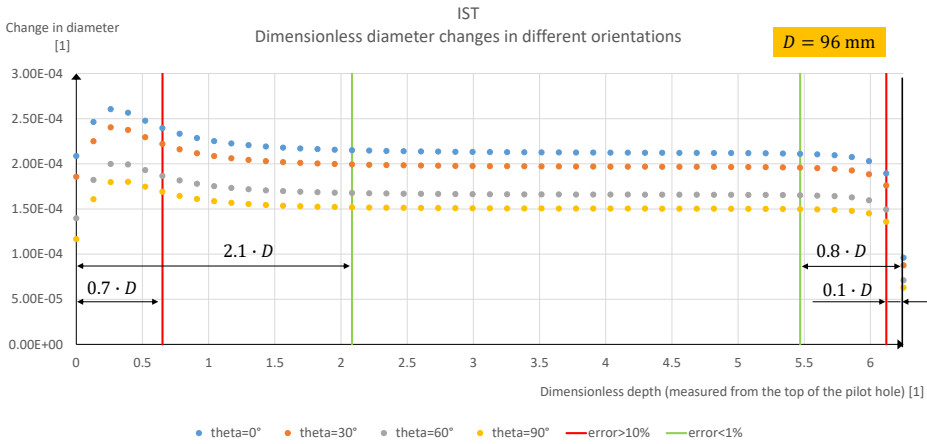


Figure 28. Dimensionless diameter change results of the IST simulation as a function of dimensionless depth in each orientation. The change in diameter values is nondimensionalized by the pilot hole diameter ($d = 25.5$ mm), the depth values by the borehole diameter ($D = 96$ mm).

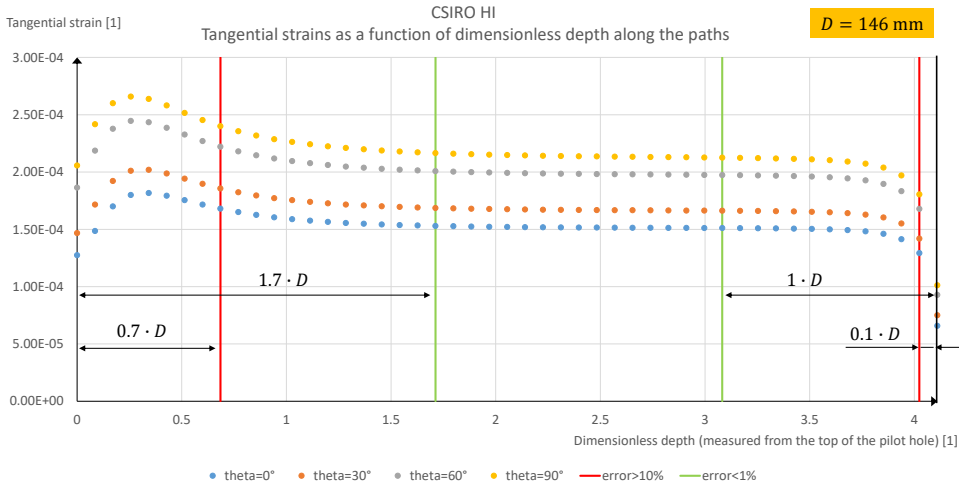


Figure 29. Tangential strain results of the CSIRO HI simulation as a function of dimensionless depth in each position. The depth values are nondimensionalized by the borehole diameter ($D = 146$ mm).

6. DISCUSSION

The present work has been carried out with the explicit assumption of homogeneous, isotropic and linearly elastic materials, in accordance with the assumptions made during the derivation of the measurement evaluation methods. However, these assumptions are all based on the necessity of making calculations feasible, while rocks are often non-homogeneous and frequently behave in an anisotropic, viscoelastic way. Thus, relaxing any of these three assumptions during the simulations would yield further valuable insight into the accuracy of the measurement techniques and evaluation methods.

A first step in this direction would be the investigation of the effects of anisotropy on the optimal placement of the instruments used. The size of the optimal and acceptable ranges of placement would, presumably, change significantly even if the condition of isotropy is relaxed to transverse isotropy. Experience of such effects is often considered when overcoring measurements are performed by experts.

Additionally, the effects of the measurement time compared to the relaxation time of a viscoelastically behaving rock type could also influence the accuracy of the estimated in situ stress state. Practical experience as well as analytical calculations [17] suggest that the measurement time indeed influences the displacements and strains observed in a borehole surrounded by a rock mass exhibiting viscoelasticity.

AUTHOR CONTRIBUTIONS

D. Borza: Methodology, Formal analysis, Investigation, Validation, Visualization, Writing – Original Draft. **D.M. Takács:** Conceptualization, Methodology, Supervision, Writing – Review & Editing.

Acknowledgement. We are grateful to László Kovács for his insightful comments regarding the simulations, as well as his kind help in providing some of the technical parameters of the measurement methods. We also thank Tamás Fülöp for drawing our attention to some possible theoretical limitations of the investigated methods.

REFERENCES

1. STEPHANSSON, O., and ZANG, A. “ISRM suggested methods for rock stress estimation – Part 5: establishing a model for the in situ stress at a given site.” *The ISRM Suggested Methods for Rock Characterization, Testing and Monitoring: 2007-2014*. Springer, 2014, pp. 187–201.
2. HUASHENG, L., OH, J., MASOUMI, H., CANBULAT, I., ZHANG, C., and DOU, L. “A review of in situ stress measurement techniques.” *Proceedings of the 2018 Coal Operators’ Conference, Mining Engineering, University of Wollongong, 18-20 February*. 2019.
3. LJUNGGREN, C., YANTING, C., JANSON, T., and CHRISTIANSSON, R. “An overview of rock stress measurement methods.” *International Journal of Rock Mechanics and Mining Sciences*, **40**(7), (2003). Special Issue of the IJRMMS: Rock Stress Estimation ISRM Suggested Methods and Associated Supporting Papers, pp. 975–989. DOI: <https://doi.org/10.1016/j.ijrmms.2003.07.003>.
4. JAEGER, J. C., COOK, N. G. W., and ZIMMERMAN, R. *Fundamentals of Rock Mechanics*. Wiley, 2007.
5. MATSUKI, K. “An elastic strain recovery compliance of rocks and its application to in situ stress measurement.” *International Journal of Rock Mechanics and Mining Sciences*, **45**(6), (2008), pp. 952–956. DOI: [10.1016/j.ijrmms.2007.10.005](https://doi.org/10.1016/j.ijrmms.2007.10.005).
6. LIN, W., YAMAMOTO, Y., and HIROSE, T. “Three-dimensional stress state above and below the plate boundary fault after the 2011 Mw 9.0 Tohoku earthquake.” *Earth and Planetary Science Letters*, **601**, (2023), p. 117888.
7. GIOT, R., GIRAUD, A., and HOMAND, F. “Three-dimensional finite element modelling of stress relaxation tests in anisotropic clayey medium: Direct problem and back analysis.” *Geotechnical and Geological Engineering*, 24 (Aug. 2006), pp. 919–947. DOI: [10.1007/s10706-005-7723-x](https://doi.org/10.1007/s10706-005-7723-x).
8. ASTM. *Standard Test Method for Determination of In Situ Stress in Rock Mass by Overcoring Method – USBM Borehole Deformation Gauge, D4623-08*. Tech. rep. 2008.
9. GRAY, I. “The measurement and interpretation of in-situ stress using an overcoring technique from surface.” *Proceedings of the 1st Canada-US Rock Mechanics Symposium - Rock Mechanics Meeting Society’s Challenges and Demands* **1**, (May 2007), pp. 721–727. DOI: [10.1201/NOE0415444019-c89](https://doi.org/10.1201/NOE0415444019-c89).

10. LEEMAN, E. R. "The borehole deformation type of rock stress measuring instrument." *International Journal of Rock Mechanics and Mining Sciences & Geomechanics Abstracts*, **4**(1), (1967), pp. 23–44. DOI: [https://doi.org/10.1016/0148-9062\(67\)90003-4](https://doi.org/10.1016/0148-9062(67)90003-4).
11. WOROTNICKI, G. "13 - CSIRO Triaxial Stress Measurement Cell." *Rock Testing and Site Characterization*. Ed. by HUDSON, J. A. Oxford: Pergamon, 1993, pp. 329–394. DOI: <https://doi.org/10.1016/B978-0-08-042066-0.50020-3>.
12. WESTWICK, D. T. and KEARNEY, R. E. *Identification of Nonlinear Physiological Systems*. IEEE Press Series on Biomedical Engineering. Wiley, 2003. DOI: 10.1002/0471722960.
13. BAHRANI, N. and VALLEY, B. "Stress Measurement: The GRC Perspective." World Mining Congress, Montreal, Jan. 2013.
14. KOVÁCS, L. *Jelentés a Bkf-(6-11) jelű fúrásokban elvégzett CSIRO HI-cellás 3D-s és Doorstopper-cellás 2D-s szekunder kőzetfeszültség-meghatározásokról*. Tech. rep. RHK Kft. Adattár: RHK-K-036/16. Pécs: Kőmérő Kft., RHK Kft., June 2016.
15. KOVÁCS, L. and VÁSÁRHELYI, B. "Special requirements for geotechnical characterization of host rocks and designing of a radioactive waste repository." *Engineering Geology for Society and Territory-Volume 6: Applied Geology for Major Engineering Projects*. Springer. 2015, pp. 909–913.
16. PHAM, J., SMITH, D., and GRAY, I. *In situ stress testing on borehole Baf-3 (318 to 835 m depth)*. Tech. rep. Sibra Job Reference Number: 511. SIGRA PTY Ltd., Mar. 2021.
17. FÜLÖP, T. and SZÜCS, M. "Analytical solutions for rheological processes around bores and tunnels." *Journal of Engineering Mathematics*, **136**(1) (2022), pp. 1–28. DOI: 10.1007/s10665-022-10235-6.

Notes for Contributors to the Journal of Computational and Applied Mechanics

Aims and scope. The aim of the journal is to publish research papers on theoretical and applied mechanics. Special emphasis is given to articles on computational mechanics, continuum mechanics (mechanics of solid bodies, fluid mechanics, heat and mass transfer) and dynamics. Review papers on a research field and materials effective for teaching can also be accepted and are published as review papers or classroom notes. Papers devoted to mathematical problems relevant to mechanics will also be considered.

Frequency of the journal. Two issues a year (approximately 80 pages per issue).

Submission of Manuscripts. Submission of a manuscript implies that the paper has not been published, nor is being considered for publication elsewhere. Papers should be written in standard grammatical English. The manuscript is to be submitted in electronic, preferably in pdf, format. The text is to be 130 mm wide and 190 mm long and the main text should be typeset in 10pt CMR fonts. Though the length of a paper is not prescribed, authors are encouraged to write concisely. However, short communications or discussions on papers published in the journal must not be longer than 2 pages. Each manuscript should be provided with an English Abstract of about 50–70 words, reporting concisely on the objective and results of the paper. The Abstract is followed by the Mathematical Subject Classification – in case the author (or authors) give the classification codes – then the keywords (no more than five). References should be grouped at the end of the paper in numerical order of appearance. Author’s name(s) and initials, paper titles, journal name, volume, issue, year and page numbers should be given for all journals referenced.

The journal prefers the submission of manuscripts in L^AT_EX. Authors should select the $\mathcal{A}\mathcal{M}\mathcal{S}$ -L^AT_EX article class and are not recommended to define their own L^AT_EX commands. Visit our home page for further details concerning how to edit your paper.

Manuscripts should be sent to either to the Editorial Office of JCAM:

jcam@uni-miskolc.hu

or directly to the editor-in-chief: Balázs Tóth

balazs.toth@uni-miskolc.hu

The eventual supply of an accepted for publication paper in its final camera-ready form will ensure more rapid publication. Format requirements are provided by the home page of the journal from which sample L^AT_EX files can be downloaded:

<http://www.mech.uni-miskolc.hu/jcam/>

These sample files can also be obtained directly (via e-mail) from Balázs Tóth.

One issue of the journal will be provided free of charge and mailed to the correspondent author. Since JCAM is an open access journal each paper can be downloaded freely from the homepage of the journal.

The Journal of Computational and Applied Mechanics is abstracted in Zentralblatt für Mathematik and in the Russian Referativnij Zhurnal.

Secretariat of the Vice-Rector for Research and International Relations, University of Miskolc

Responsible for publication: Prof. dr. Zita Horváth, rector

Published by the Miskolc University Press under the leadership of Attila Szendi

Responsible for duplication: Works manager Erzsébet Pásztor

Number of copies printed: 75

Put to the Press on January 14, 2025

Number of permission: TNI.2025-20.ME.

ISSN 2732-0189 (Online)

ISSN 1586-2070 (Print)

A Short History of the Publications of the University of Miskolc

The University of Miskolc (Hungary) is an important center of research in Central Europe. Its parent university was founded by the Empress Maria Teresia in Selmecbánya (today Banská Štiavnica, Slovakia) in 1735. After the first World War the legal predecessor of the University of Miskolc moved to Sopron (Hungary) where, in 1929, it started the series of university publications with the title *Publications of the Mining and Metallurgical Division of the Hungarian Academy of Mining and Forestry Engineering* (Volumes I.–VI.). From 1934 to 1947 the Institution had the name Faculty of Mining, Metallurgical and Forestry Engineering of the József Nádor University of Technology and Economic Sciences at Sopron. Accordingly, the publications were given the title *Publications of the Mining and Metallurgical Engineering Division* (Volumes VII.–XVI.). For the last volume before 1950 – due to a further change in the name of the Institution – *Technical University, Faculties of Mining, Metallurgical and Forestry Engineering, Publications of the Mining and Metallurgical Divisions* was the title.

For some years after 1950 the Publications were temporarily suspended.

After the foundation of the Mechanical Engineering Faculty in Miskolc in 1949 and the movement of the Sopron Mining and Metallurgical Faculties to Miskolc, the Publications restarted with the general title *Publications of the Technical University of Heavy Industry* in 1955. Four new series – Series A (Mining), Series B (Metallurgy), Series C (Machinery) and Series D (Natural Sciences) – were founded in 1976. These came out both in foreign languages (English, German and Russian) and in Hungarian. In 1990, right after the foundation of some new faculties, the university was renamed to University of Miskolc. At the same time the structure of the Publications was reorganized so that it could follow the faculty structure. Accordingly three new series were established: Series E (Legal Sciences), Series F (Economic Sciences) and Series G (Humanities and Social Sciences). The latest series, i.e., the series H (European Integration Studies) was founded in 2001. The eight series are formed by some periodicals and such publications which come out with various frequencies.

Papers on computational and applied mechanics were published in the

Publications of the University of Miskolc, Series D, Natural Sciences.

This series was given the name Natural Sciences, Mathematics in 1995. The name change reflects the fact that most of the papers published in the journal are of mathematical nature though papers on mechanics also come out.

The series

Publications of the University of Miskolc, Series C, Fundamental Engineering Sciences

founded in 1995 also published papers on mechanical issues. The present journal, which is published with the support of the Faculty of Mechanical Engineering and Informatics as a member of the Series C (Machinery), is the legal successor of the above journal.



Journal of Computational and Applied Mechanics

Volume 19, Number 1 (2024)

Contents Contributed Papers

- István ECSEDI and Ákos József LENGYEL: Investigation of the stress state in a thin elastic disc 3–15
- Ibrahim Kipngeno ROTICH and László E. KOLLÁR: Numerical study of ice accretion on blade surface with varying cloud characteristics 17–35
- Dávid BORZA and Donát M. TAKÁCS: Analysis of overcoring in situ stress measurement methods using finite element simulations 37–79